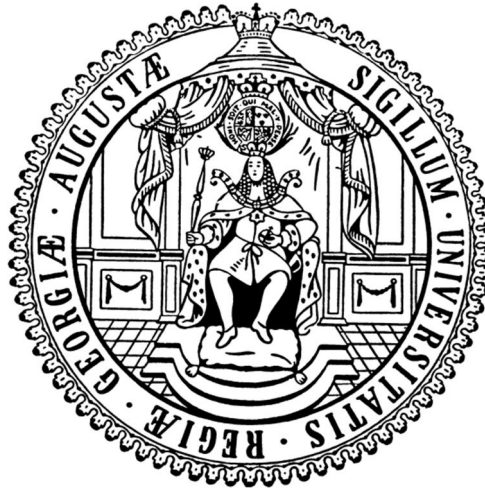


Evaluation of Detector and Intensity Reliability in Charge Density Studies



Dissertation

zur Erlangung des mathematisch-naturwissenschaftlichen Doktorgrades

„Doctor rerum naturalium“

der Georg-August-Universität Göttingen

im strukturierten Promotionsprogramm

der Georg August University School of Science (GAUSS)

vorgelegt von Felix Engelhardt

aus Northeim

Göttingen, 2017

Betreuungsausschuss

Prof. Dr. D. Stalke, Institut für Anorganische Chemie, Georg-August-Universität

Dr. F. Fabbiani, GZG, Georg-August-Universität

Mitglieder der Prüfungskommission

Referent:

Prof. Dr. D. Stalke, Institut für Anorganische Chemie, Georg-August-Universität

Korreferentin:

Dr. F. Fabbiani, GZG, Georg-August-Universität

weitere Mitglieder der Prüfungskommission

Dr. H. Sowa, GZG, Georg-August-Universität

Prof. Dr. F. Meyer, Institut für Anorganische Chemie, Georg-August-Universität

Prof. Dr. Ricardo Mata, Institut für Physikalische Chemie, Georg-August-Universität

Jun.-Prof. Dr. Selvan Demir, Institut für Anorganische Chemie, Georg-August-Universität

Tag der mündlichen Prüfung: 09.05.2017

Table of Contents

1	Single Crystal X-ray Diffraction.....	1
1.1	The independent atom model.....	1
1.2	Multipole Model	2
1.3	Data Quality	3
1.3.1	Experimental Setup.....	3
1.3.2	Intensity Statistics and Diederichs Plots.....	4
1.4	Model Quality Indicators.....	6
1.5	Validation of Refined Models via R_{free}	7
1.6	Residual Density Analysis.....	9
1.7	Observed and Calculated Structure Factors.....	10
2	Quantum Theory of Atoms in Molecules (QTAIM)	13
2.1	Atomic Basins.....	13
2.2	Critical Points	14
2.3	The Laplacian	15
2.4	Non-covalent Interaction (NCI).....	16
3	Charge Density Analysis of Lithium[2,5-bis((dimethylamino)methyl)pyrrolide].....	21
3.1	Data collection and data processing	23
3.2	Structure solution and refinement (IAM)	24
3.3	General discussion of the IAM of 1	24
3.4	Multipole model refinement	27
3.5	Validity of the model	32
3.6	Topological analysis of Lithium[2,5-bis((dimethylamino)methyl)pyrrolide].....	36
3.7	Conclusion.....	43
4	Charge Density Analysis of dipotassium phenylene-1,4-bis(trifluoroborate).....	45
4.1	Data collection and data processing	47
4.2	Structure solution and refinement	48
4.3	General Discussion of the IAM	49
4.4	Multipole model refinement	50
4.5	Validity of the model	53
4.6	Topological Analysis of dipotassium phenylene-1,4-bis(trifluoroborate)	55
4.7	Conclusion.....	61
5	Influence of the Estimated Standard Deviation on Charge Density Refinements	63
5.1	Descripton	65

5.2	Examination of the raw and processed data	66
5.3	Differences in the model for compound 1	68
5.4	Differences in the derived properties for compound 1	74
5.5	Differences in the model for compound 2	79
5.6	Differences in the derived properties for compound 2	84
5.7	Conclusion	86
6	Short Term Stability of X-ray detectors	89
6.1	Working principle of the used X-ray detectors	90
6.1.1	CCD sensors vs CMOS sensors.....	91
6.1.2	Hybrid Pixel Counting sensors	93
6.2	Temporary adaption of a PILATUS3 R CdTe to a BRUKER D8 Diffractometer	95
6.3	Short-term stability tests	96
6.4	Results	98
6.5	Summary	103
7	Evaluation of errors introduced to X-ray Data by the timing shutter	105
7.1	Results	106
7.2	Conclusion	107
8	Data collection at SPring-8 BL02B1	109
8.1	Experimental measurements.....	110
8.2	Conclusion	111
9	Single Crystal Structures Determination	113
9.1	Collaboration with Dr. Rajendra Ghadwal	114
9.1.1	Unpublished Structures	114
	References.....	120
	Danksagung.....	129
	Curriculum Vitae	131

1 Single Crystal X-ray Diffraction

Since the discoveries of *Friedrich, Knipping* and *von Laue* about the interference of X-rays with crystalline matter little over a hundred years ago X-ray diffraction has developed into one of the most powerful analytic methods.^[1] This is also due to the contributions to of *Debye* and *Scherrer* as well as *Hull* who independently developed X-ray Powder diffraction.^[2,3] The underlying principles however have remained the same since *W. H. Bragg* and *W. L. Bragg* derived the fundamental laws of X-Ray diffraction.^[4-6]

1.1 The independent atom model

The independent atom model (IAM) which is used widely for routine structure determination is one possibility to describe the atomic contributions to the electron density within the unit cell. It assumes that the electrons density is mostly located around the core and follows a spherical distribution. Furthermore, it does not take interactions between atoms into account. The spherical atom form factors are defined as

$$f_j(\mathbf{H}) = \int \rho_j(\mathbf{s}) e_j^{2\pi\mathbf{H}\mathbf{s}dV} \quad (1)$$

with an integration over the volume of the respective atom. This atom form factor is the used to get the calculated structure factor F_{calc} . An initial model is usually supplied by the structure solution program. This model is then refined in a least squares procedure. Within this procedure the equation

$$\sum_{hkl} w\Delta^2 = \sum_{hkl} w_{hkl} (sF_{obs}^2 - F_{calc}^2)^2 \quad (2)$$

is minimized. Therein w_{hkl} represents a weighting factor which takes the standard uncertainties $\sigma(F_{hkl})$ of the individual reflections into account. The calculated and observed structure factors are not necessarily on the same scale therefore the scale factor s is introduced. Usually the scale factor is determined from the ratio between the sum of the observed squared structure factors and the calculated squared structure factors.

1.2 Multipole Model

The assumption made by the IAM that the atoms do not interact with each other is certainly valid and useful for routine structure determination. However, the deficiencies of the IAM become visible if high resolution data are taken into account. Throughout this and the next chapter a high resolution data set ($\frac{\sin \theta}{\lambda} = 1.16 \text{ \AA}^{-1}$) of oxalic acid recorded in our workgroup is used as an example. Figure 1 shows the

difference
density map
of oxalic
acid after
the IAM
refinement
(left) and
after

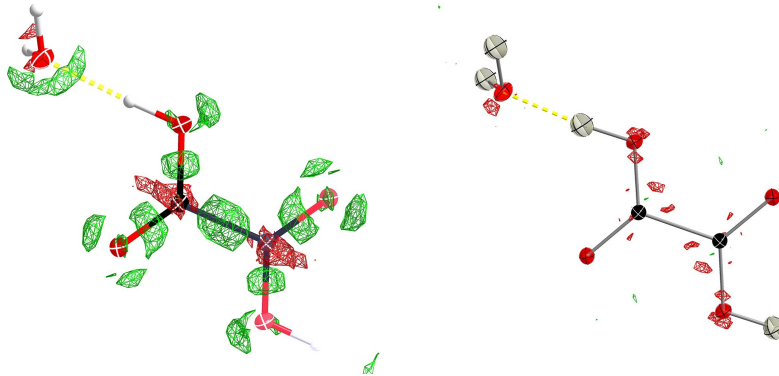


Figure 1: Difference density before (left) and after (right) refinement of oxalic acid with the multipole model. The difference density map is depicted at a level of 0.1 e\AA^{-3} .

refinement with the multipole model (MM). It can be clearly seen that electron density which is not described by the IAM is still visible in the bonding regions and for the oxygen atoms in regions where lone pairs would be expected. To also take this into account the assumption of the spherical distribution of the electron density needs to be replaced. A number of different approaches were made to describe aspherical bonding electron density.^[7,8] Amongst these is the multipole model developed by *Hansen* and *Coppens* which is based on works of *Stewart*.^[7,9-13] Within the multipole model the electron density around the atoms is no longer considered to be spherical but rather divided into three parts:

$$\begin{aligned} \rho(\mathbf{r}) = & P_c \rho_c(\mathbf{r}) + P_v \kappa^3 \rho_{sph}(\kappa, \mathbf{r}) \\ & + \sum_{l=0}^{l_{max}} \kappa'^3 R_l(\kappa', \mathbf{r}) \sum_{m=-l}^l P_{lm} Y_{lm}(\vartheta, \varphi) \end{aligned} \quad (3)$$

The first part does represent the spherical core electron density, the second a spherical contribution to the valence density and the last part does account for deformations within the valence density. The factors P_c , P_v and P_{lm} are the

population factors. For the radial distribution function $R_l(\kappa')$, typically *Slater* functions are used. The deviation from sphericity is modelled by the spherical harmonics Y_{lm} . The parameter l does control to which order spherical harmonics are used. In the XD2006 program, l_{max} is arbitrarily limited to four. The refinement is then carried out by stepwise increasing the complexity of the model.

1.3 Data Quality

As stated in the previous chapter for an accurate description of the valence electron density high quality and high resolution data sets are needed. Therefore, it is crucial to judge on the quality of the measured data. Within this chapter selected premises and indicators of data quality in charge density investigations are discussed.

1.3.1 Experimental Setup

Undoubtedly, the experimental setup does influence the quality of the measured data. This includes all the components used in the diffractometer from the X-ray source over the monochromator, goniometer and crystal-cooling device to the detector.

First of all, to achieve high resolution data sets of course the best crystal has to be selected. However, the best crystal is of no use if the intensity of the X-ray source is not sufficient.

Traditionally, rotating anodes have been used for charge density measurements. With the introduction of the so-called micro-sources another alternative entered the field.^[14-16] Through the constant development since the introduction of the first INCOATEC micro-focused sealed tube in 2006, a dramatic increase in X-ray intensity could be achieved for the latest generation.^[17] In contrast to the maintenance intensive rotating anodes these sources offer longer maintenance intervals, are air-cooled and consume a considerably lesser amount of energy. On the downside, these X-ray sources are less intense and as a consequence of the mirror optics used to monochromatise and focus the X-ray beam a low-energy contamination thereof is inevitable. The setup of the X-ray mirrors does also allow certain integer

multiples of the desired wavelength to pass through.^[15] As *Macchi et al* suggest this contamination can be minimized by using aluminium foil as a filter. This method however does further reduce the intensity of the beam. Fortunately, *Krause et al* recently developed a protocol to correct for this kind of low energy contamination.^[18] The so-called 3λ contamination does mainly affect the reflections with indices $3h, 3k, 3l$ and is treated in analogy to the $\lambda/2$ correction for charge coupled device (CCD) detectors introduced by *Pinkerton et al.*^[19] Therefore, it is now possible to use the full intensity of the micro focus-sealed tubes.

Another factor which is directly influencing the data quality is the detector. As well as X-ray sources, X-ray detectors have been constantly updated since early days of crystallography. An in depth discussion of their influence on the data quality is given in Chapter 6.

It is also desirable to carry out X-ray diffraction experiments at the lowest possible temperature do reduce the atomic thermal vibrations.^[20] This facilitates the deconvolution of the electron density and the thermal motion.

1.3.2 Intensity Statistics and Diederichs Plots

After having successfully recorded, reduced and scaled a data set its quality needs to be judged. One of the first quality indicators addressed is the intensity statistic computed by the scaling and absorption correction program (within this thesis the program SADABS^[16] is used, exclusively). The intensity statistic is given in the form of a plot of the R_{int} and the R_{sigma} versus the resolution. The R_{int} and the R_{sigma} are defined as

$$R_{int} = \frac{\sum |F_o^2 - \langle F_o^2 \rangle|}{\sum [F_o^2]} \quad (4)$$

and

$$R_{sigma} = \frac{\sum [\sigma(F_o^2)]}{\sum [F_o^2]} \quad (5)$$

with the observed structure factor F_o^2 and its standard uncertainty $\sigma(F_o^2)$. Figure

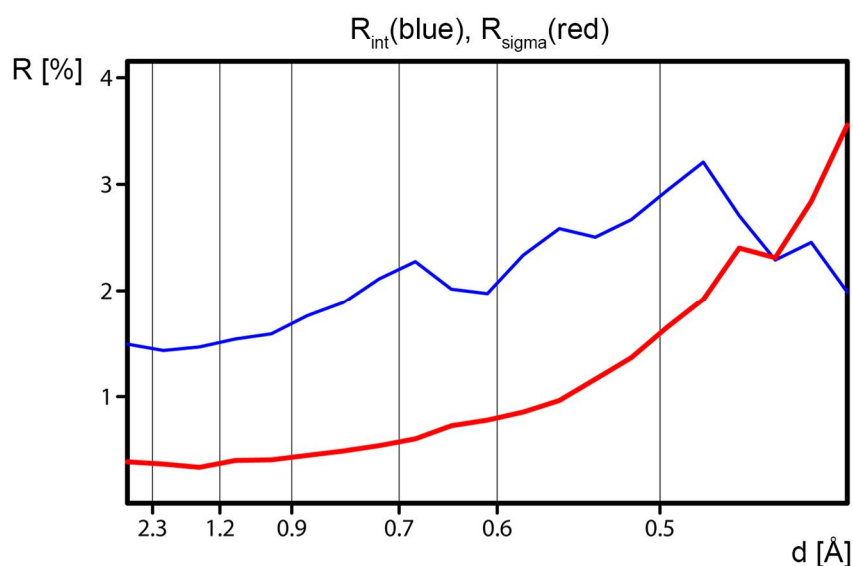


Figure 2: Intensities statistics for oxalic acid as plotted by SADABS.

2 shows the plot of the R_{int} and the R_{sigma} vs the resolution for oxalic acid. As defined the R_{int} is the sum of the deviation from the mean observed structure factor divided by the observed structure factor. In principle it is a measure of internal agreement of independent measurements of symmetry related structure factors. The R_{sigma} is a similar quantity using the sum of the standard uncertainties and the sum of the observed structure factor. For a charge density measurement it is desirable that these values do not exceed a value of 10 % throughout the whole resolution range. Furthermore, for the innermost resolution shells the R -values should not exhibit values larger than 5 %. Additionally, features within this plot can also be an indicator for uneven data collection over the resolution shells. However, the R_{int} is dependent on the multiplicity of the measured data. In general, the multiplicity should be as high as possible in both routine and charge density measurements. As a rule of thumb the overall multiplicity should be larger than 4 and additionally for the inner data larger than 10. Due to this dependency it is advisable to also consider the $R_{r.i.m.}$ and the $R_{p.i.m.}$ introduced by Weiss et al.^[21] While the $R_{r.i.m.}$ gives a measure for the precision of the individual reflection without being dependant on the multiplicity the $R_{p.i.m.}$ describes the precision of the averaged measurement.

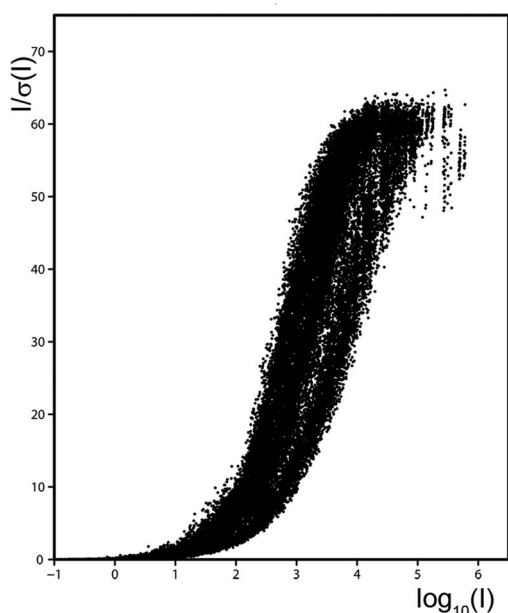


Figure 3: Diedrichs plot for oxalic acid.

Another diagnostic tool which is provided by SADABS is the *Diedrichs* plot.^[22,23] *Diedrichs* proposed to plot the significance $I/\sigma(I)$ versus the decadic logarithm of the intensity ($\log_{10} I$). These plots have been initially designed for macromolecular crystallography but can also be applied to small molecules. Figure 3 shows an exemplary plot for oxalic acid. Typically, these plots show a sigmoidal shape. A large maximum value indicates string reflections with low sigma values. This gives rise to the conclusion that experimental and systematic errors are minimal for the collected data.

1.4 Model Quality Indicators

The commonly used quality indicator in both the IAM and the MM are the R_I and the wR_2 . The former is calculated on the structure factor F while the latter is calculated on F^2 . The quantities are defined as follows:

$$R_1 = \frac{\sum ||F_{obs}| - |F_{calc}||}{\sum |F_{obs}|} \quad (6)$$

$$wR_2 = \sqrt{\frac{\sum w(F_{obs}^2 - F_{calc}^2)^2}{\sum F_{obs}^4}} \quad (7)$$

Commonly in routine structure determination the wR_2 is considered to judge on the model quality however the R_I is also calculated. Within the charge density community there is no convention whether to use the R_I or the wR_2 . The influence of weak reflections on the R_I is slightly higher which suggests the use of the wR_2 . Within this thesis consequently the wR_2 is used.

For data of average quality, the R_I should be lower than 5 % and the wR_2 should be smaller than 10 % if the structure does not show signs of disorder. However, for charge density refinements both quantities should be well below 10 %. In this

context it needs to be stated that the R factors solely state that the refined model does fit the measured data mathematically correct. This does however not take into account if the refined model is of chemical validity or if artefacts are modelled. Therefore, in addition to these R factors other figures of merit which will be discussed below need to be considered too.

1.5 Validation of Refined Models via R_{free}

The use of the multipole model does introduce up to 50 parameters per atom on top of the 9 parameters used by the IAM. This does show one of the perils of charge density refinements. By introducing a large number of parameters to a model the agreement with the data increases. This phenomenon is called overfitting. This may be visualized by a simple example shown in Figure 5 and Figure 4. It can be seen that the linear fit with a minimum of parameters describes the data quite well while the 6th polynomial fit does match the data points perfectly. Even though the polynomial fit does describe the data better the linear fit is correct. The question that needs to be asked is, how many parameters may be refined with the current data set. A general rule of thumb has been established in crystallography to prevent overfitting, that the data to parameter ratio should not fall below ten. However, it is not necessarily true for every data set that this rather arbitrary value does prevent overfitting. To overcome this problem macromolecular crystallographers have used the method of cross validation.^[23–26] Cross validation is a statistical technique for which the data is divided into two sets, the larger training or working set and the smaller test set. The model building process is then performed on the working set while the test set is left untouched. Subsequent to the model building process the derived model is taken and applied to the test set. If the model derived from the

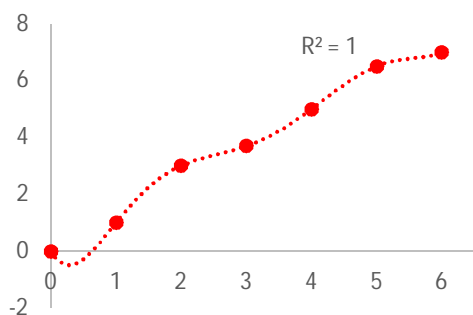


Figure 5: Plot of data with 6th order polynomial fit.

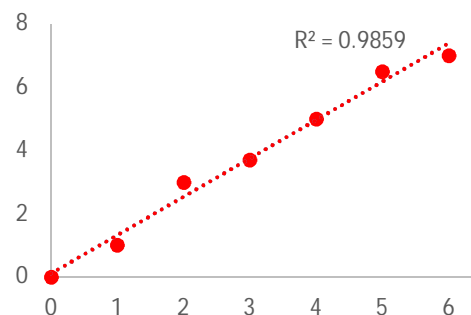


Figure 4: Plot of data with linear regression.

working set is correct it should also fit the test set. Due to the fact that in charge density refinements single reflections can have huge influence on the model the k-fold cross validation is used. In k-fold cross validation the full data set is subdivided into k sets of equal size. The model building process is then performed k times on k-1 parts of the data. In each of the k model building processes another fraction of the data is left untouched as training set. The final model quality indicators are then calculated from the mean of the k individual quality indicators (see Figure 6). This procedure has already been applied for a charge density refinement by *Paul et al* using the MOPRO program suite.^[27,28] A protocol to use this procedure with the XD2006 program suite^[29] has been developed within our workgroup.^[30] The data set is divided in k sets with some considerations concerning the subdivision into account. For example, it is necessary that *Friedel* pairs end up together either in the test or working set. For each step of the refinement the model quality indicators are calculated for the test and working set. A decrease in R -value of the working set (R_{work}) when adding more parameter to the refinement should also result in a decrease in R -value of the test set (R_{free}) if this is not overfitting. In consequence, a decrease of R_{work} associated with an increase in R_{free} is considered to be overfitting. Additionally, another indicator is calculated the so called R_{cross} . The R_{cross} is

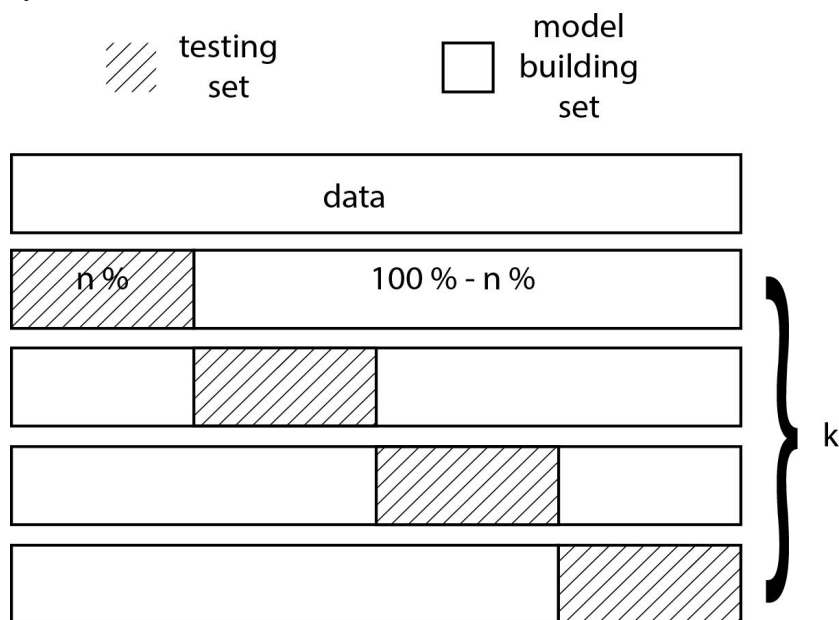


Figure 6: Schematic representation of the k-fold cross validation technique.

calculated from the combined calculated intensities as outputted by the refinement program.

1.6 Residual Density Analysis

One important quality indicator is the difference or residual density. The difference density is obtained by Fourier transformation of the difference $|F_{obs}^2| - |F_{calc}^2|$. In an ideal measurement with no systematic or random errors the calculated structure factors should directly match the observed structure factors and thus the

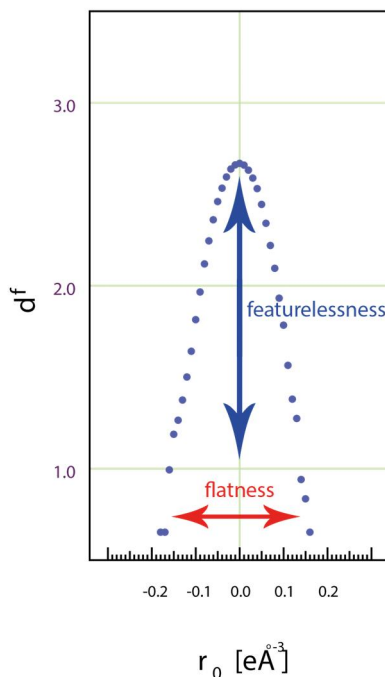


Figure 7: Plot of the fractal dimension of the residual density versus the residual density. The distribution is calculated on the same model as shown in Figure 1.

residual density after refinement should vanish. However, due to errors within the experimental setup and errors in the method of how the structure factors are reconstructed from the measured intensities, this may not be achieved. The consequence is that even after refinement with the flexible multipole model residual density still is present (cf. Figure 1). A first estimator to judge on the quality of the model are the values of the highest peak and the deepest hole within the residual density. The values thereof should be reasonably small. However, judgement by two singular values is not advisable. Instead the overall distribution of the residual density should be “flat and featureless”. In 2008 *Meindl et al* reported on

the possibility to judge on the flatness and the featurelessness of the residual density by calculating the fractal dimension of the residual density within the unit cell.^[31] The fractal dimension is then plotted versus the residual electron density. The outcome resembles an inverted parabola. The height of the parabola indicates the featurelessness. For a grid with no residual density the fractal dimension equals to three. By inclusion of residual density into this grid the value is lowered. Thus the maximum value of the parabola should be as close as possible to three. The flatness

of the residual density can be judged by the width of the parabola. The smaller the width of the parabola, the flatter the distribution of the residual density.

1.7 Observed and Calculated Structure Factors

One important quality indicator is the ratio of the observed and calculated structure factors in dependence of the resolution. The ratio does deliver a measure for the suitability of the model with respect to the data. In the case of an ideal agreement between

model and measurement this ratio should equal to unity. An example of such a plot is shown

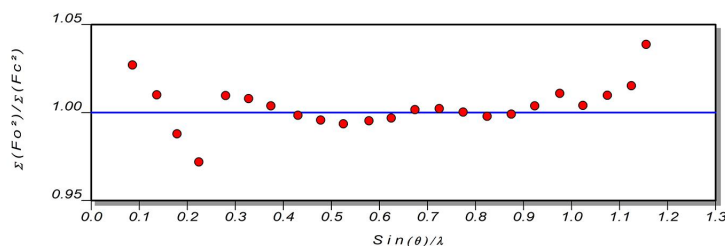


Figure 8: Plot of the ratio between observed and calculated structure factors in dependence of the resolution for oxalic acid after MM refinement.

in Figure 8. Each point in the plot is calculated for a distinct resolution batch. The deviations from unity may be due to a variety of causes. Amongst these is the experimental setup and data reduction which do influence the observed structure factors and may thus influence the course of the plot. Furthermore, this plot may indicate resolution dependent errors such as thermal diffuse scattering.^[32] A detailed investigation of the behaviour of these plots for modern area detectors was published by *Zhurova et al.*^[33]

Previous studies showed that the investigation of these plots can indicate deficiencies in the data.^[32,34,35] As *Wolf et al* showed problems such as overexposures can be revealed for the innermost reflections.^[34] However the DRKPLOT^[36] program commonly used to generate the plots lacks some features to facilitate their identification. One of these not delivered informations is the exact binning, which was

applied. By careful investigation of Figure 8 it can be noticed that the data points are not equidistant. Table 1 summarizes the first four data points shown in Figure 8. While the first and the second data point show a distance of 0.0508 \AA^{-1} the second and third are only 0.0419 \AA^{-1} apart. Furthermore, the program does not report the

Table 1: Resolution and ratio of the observed and calculated structure factor for selected data points in Figure 8.

#	$\frac{\sin \theta}{\lambda} / \text{\AA}^{-1}$	$\frac{\sum F_o^2}{\sum F_c^2}$
1	0.0856	1.0271
2	0.1364	1.0102
3	0.1783	0.9880
4	0.2238	0.9720

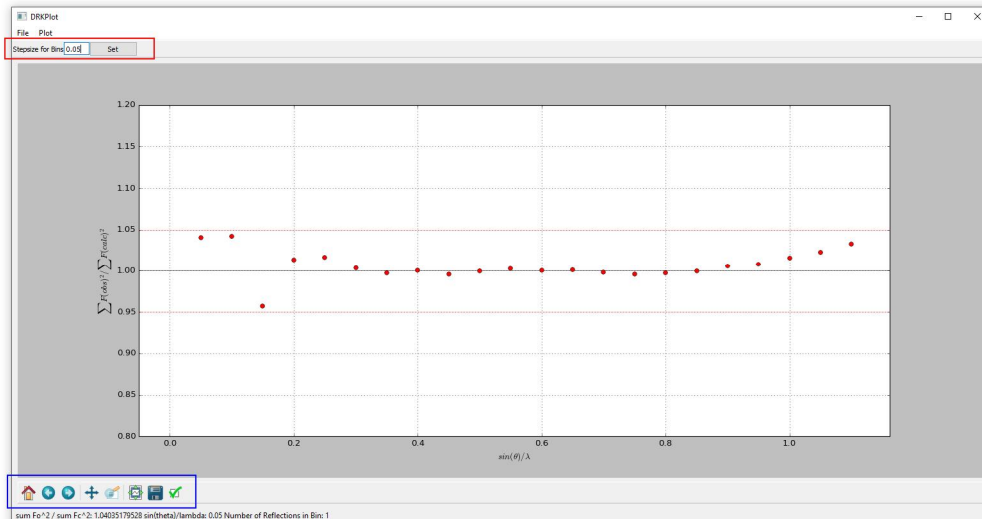


Figure 9: Graphical interface after loading of an Xd2006 structure factor file. Red square indicates step size control. Blue square indicates graph manipulation toolbox.

number of reflections in the individual bins. The number of reflections and the exact binning boundaries however bear crucial information. Especially for the in the low resolution range the number of reflections in the bins is typically small. This however, means that the influence of individual reflections on the ratio of the sum of the observed and calculated structure factors is increased.^[34] To overcome these limitations within this thesis the functionality of the DRKPLOT program was reimplemented and complemented with the desired features. The program was written in PYTHON using the PYQT graphical framework to enable interactive manipulation of the plots. Figure 9 shows the graphical interface after the loading of an Xd2006 structure factor file. By default, the ratio of the observed and calculated structure factors is displayed. The stepsize of the binning

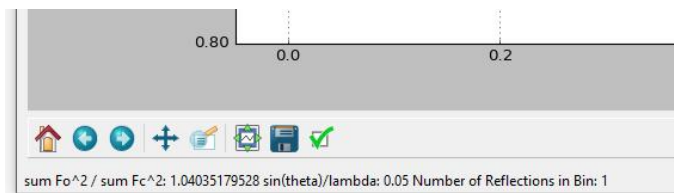


Figure 10: Information displayed in the status bar of the program.

can be easily chosen (red square). The blue square in Figure 9 indicates the control buttons for zooming and other manipulations of the plot. By clicking one of the data points, a summary of important parameters is displayed in the status bar of the window (Figure 10). These include the value of $\frac{\sum F_o^2}{\sum F_c^2}$, the resolution and the number of reflections in this particular bin. As in the original DRKPLOT program, several other diagnostic plots were implemented. In contrast to the previously discussed

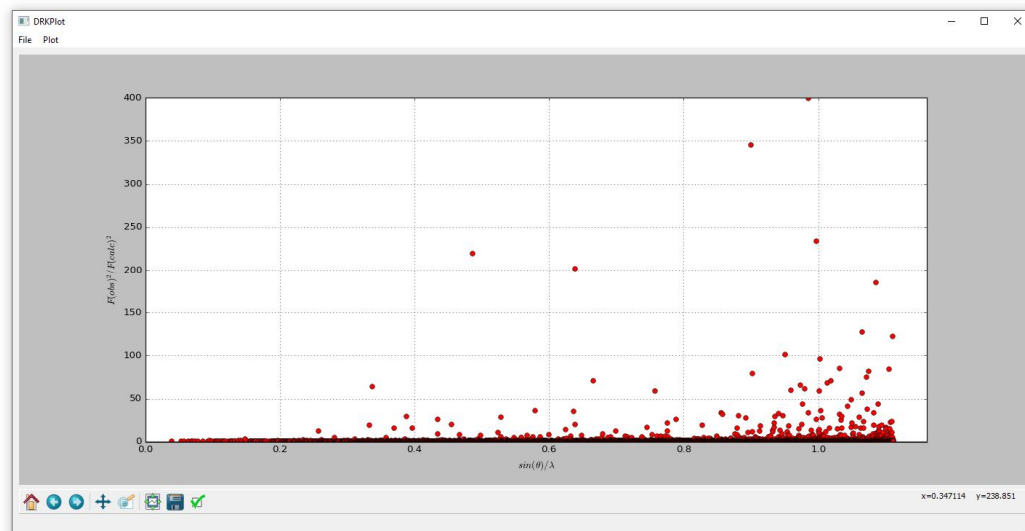


Figure 11: Program displaying the plot of $\frac{F_o^2}{F_c^2}$ versus the resolution.

plot of $\ln\left(\frac{F_o^2}{F_c^2}\right) + 1$ or $\frac{F_o^2}{F_c^2}$ versus the resolution can be used to identify individual reflections. As an example the plot of $\frac{F_o^2}{F_c^2}$ versus the resolution was chosen (Figure 11). In Figure 11 it can be seen that the ratio of the observed and calculated structure factors spans a wide range of values (maximum value 399.0). Within the DRK PLOT program by *Stash* the cannot be interactively manipulated which complicates the search for individual reflections especially in the low resolution range. Within the newly developed program the plot can be interactively zoomed to facilitate the identification of reflections.

In addition to the ratio of the observed and calculated structure factors the values of the squared difference of the observed and calculated structure factors should follow a normal distribution.^[33,37] To test this the weighted differences are plotted against the expected differences. For an ideal match this would result in a line of slope one through the origin (Figure 12).

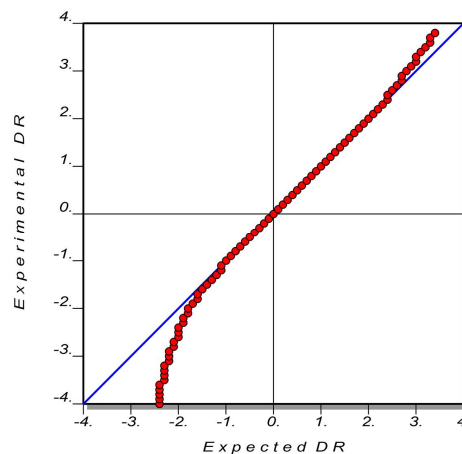


Figure 12: Normal probability plot of oxalic acid after MM refinement.

2 Quantum Theory of Atoms in Molecules (QTAIM)

The result of the multipole model refinement is an electron density distribution including the valence density. However, it is not the electron density distribution as such which is interesting to the chemist but the properties derived from it. The theoretical framework to interpret the received electron density distribution has been developed by *Bader*.^[38–41] The theory implies that the electron density can be described as a scalar vector field which may be analysed by its gradient vector field. Furthermore, the QTAIM does assume that the properties of a molecule can be understood as the sum of the atomic contributions. Therefore, the definition of the boundaries of an atom is crucial.

2.1 Atomic Basins

One of the major advantages of the QTAIM is the straightforward way to partition the electron density in atomic basins. To achieve this the gradient of the electron density

$$\nabla\rho = \mathbf{i}\frac{\partial\rho}{\partial x} + \mathbf{j}\frac{\partial\rho}{\partial y} + \mathbf{k}\frac{\partial\rho}{\partial z} \quad (8)$$

with the Cartesian basis vectors \mathbf{i} , \mathbf{j} and \mathbf{k} is analysed. Within the gradient vector field each point equals to a vector which is directed towards the steepest increase in electron density. This means that every trajectory within this vector field terminates in a point of maximum electron density. These points are called attractors and are usually located at the atomic positions. The atomic basin is defined by all trajectories terminating in the respective attractor and do not cross the boundary surface of the atom. The boundary surface is called *zero flux surface* and does fulfil the condition:

$$\nabla\rho \cdot \mathbf{n}(\mathbf{r}) = 0 \quad (9)$$

Because of the vanishing scalar product of $\nabla\rho$ and the surface normal $\mathbf{n}(\mathbf{r})$ this zero flux surface cannot be crossed by trajectory paths. Thus an atom basin can be elegantly identified by trajectories within the gradient vector field.

By this unambiguous partitioning of the molecule into atoms it is also possible to calculate atomic charges. This is achieved by integrating the electron density within the atomic basins as defined by the zero flux surfaces.

2.2 Critical Points

Special positions within the electron density ρ are called *critical points* (CP). These points are located at minima, maxima and saddle points within the electron density. Thus the corresponding gradient must vanish:

$$\nabla\rho = \begin{pmatrix} \frac{\partial\rho}{\partial x} \\ \frac{\partial\rho}{\partial y} \\ \frac{\partial\rho}{\partial z} \end{pmatrix} = 0 \quad (10)$$

To distinguish between maxima, minima and saddle points the sign of the second derivative of the electron density is used. Therefore, the eigenvalues of the Hessian matrix

$$H = \begin{pmatrix} \frac{\partial^2\rho}{\partial x^2} & \frac{\partial^2\rho}{\partial x\partial y} & \frac{\partial^2\rho}{\partial x\partial z} \\ \frac{\partial^2\rho}{\partial y\partial x} & \frac{\partial^2\rho}{\partial y^2} & \frac{\partial^2\rho}{\partial y\partial z} \\ \frac{\partial^2\rho}{\partial z\partial x} & \frac{\partial^2\rho}{\partial z\partial y} & \frac{\partial^2\rho}{\partial z^2} \end{pmatrix} \quad (11)$$

which consists of the second derivatives of the electron density with respect to all possible combinations of coordinates are calculated. The critical points are characterised using two criteria. First the rank of the critical point. The rank of the critical points is defined by the number of non-zero eigenvalues λ_1 , λ_2 and λ_3 . The rank of critical points will in almost all cases be three as the crystal structure

Table 2: Summary of the classification of the critical points in ρ

(m,n)	Name	Chemical interpretation
3,-3	atomic position	atomic position
3,-1	bond critical point	chemical bond
3,+1	ring critical point	closed ring of chemical bonds (at least 3 bonds involved)
3,+3	cage critical point	Closed cage of chemical bonds (at least 4 bonds involved)

represents in almost all cases a state of minimum energy and

thus all curvatures will be different from zero. The second criterion is the signature. The signature is the sum of the signs of the eigenvalues of the Hessian matrix. This gives rise to four possible critical points within ρ . Atomic positions (AP) are found if all eigenvalues of the Hessian matrix show a negative sign, bond critical points (BCP) if the sum of signs equals -1, ring critical points (RCP) if the sum equals 1 and cage critical point (CCP) if all eigenvalues exhibit a positive sign (Table 2). In association with the critical points one important relationship between the number of non-degenerate critical points in a non-periodic system, the *Poincaré-Hopf* relationship, needs to be mentioned. The *Poincaré-Hopf* rule links the number of critical points as follows:

$$n - b + r - c = 1 \quad (12)$$

with n being the number of atomic positions, b the number of BCPs, r of RCPs and c the number of CCPs. The set of numbers n , b , r and c is called characteristic set. For a single molecular structure this relation must be satisfied.

2.3 The Laplacian

The electron density is mostly dominated by the core electrons. This however is unfortunate because the interesting features for the chemist are the subtle changes due to the valence electrons. To overcome this difficulty, the second derivative with respect to the Cartesian coordinates, also called the *Laplacian* ($L(\mathbf{r}) = \nabla^2 \rho(\mathbf{r})$) is used to visualize the effects of the valence density. Within the Laplacian negative values ($L(\mathbf{r}) < 0$) might be interpreted as accumulations of electron density while

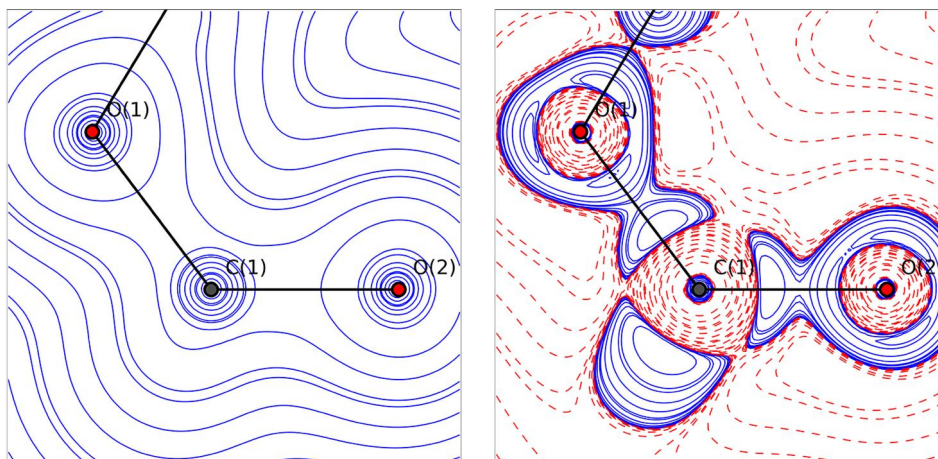


Figure 13: Isocontour drawing of the electron density ρ (left) and the Laplacian (right) for oxalic acid. For the Laplacian blue lines denote negative values and red lines positive values.

positive values ($L(\mathbf{r}) > 0$) indicate electron density depletions. Figure 13 shows an example of isocontour map of the Laplacian and the electron density of oxalic acid. In contrast to the electron density in the Laplacian features like bond and non-bond directed density concentrations can be identified. The Laplacian, as the electron density, can be searched for critical points. These critical points typically occur in either bonding or non-bonding regions. These critical points are termed *valence shell charge concentrations* (VSCC). Typically, these critical points form a geometry in agreement with the geometry as predicted for the *Lewis* concept of bonding and non-bonding electron pairs.^[38,42]

The Laplacian is furthermore used to characterise different types of bonding. A covalent bond is characterised by a negative value of the Laplacian at the bond critical point. It can be best visualised by two VSCCs merging during the process of bond forming. This type is also called *shared interaction* within the QTAIM framework. In contrast to that an ionic or *closed shell interaction* is associated with a positive value of the Laplacian at the BCP.

2.4 Non-covalent Interaction (NCI)

The QTAIM itself as developed by *Bader* is not particularly good in the description of interactions as for example multi centre bonds, C-H \cdots π interactions, dipole – dipole interactions, steric repulsion or London dispersion. Typically, these interactions are summarised as so-called packing effects. In routine structure determination, these packing effects have mostly been called on to explain unusual molecular geometries.^[43] To overcome these shortcomings other descriptors than the ones defined by *Bader* need to be considered. *Johnson et al* and *Contreras-Garcia et al* evaluated the possibility to adapt the reduced density gradient (RDG) $s(\mathbf{r})$ which is a common descriptor in density functional theory (DFT) to the QTAIM.^[44,45] In their publications the reduced density gradient is defined as follows:

$$s(\mathbf{r}) = \frac{|\nabla\rho(\mathbf{r})|}{2\sqrt[3]{3\pi^2}\sqrt[3]{\rho(\mathbf{r})^4}} \quad (13)$$

The reduced density gradient is a dimensionless quantity which is by definition zero for all points within a homogeneous electron gas. This means deviations of the RDG from zero indicate deviations from homogeneity of the charge density. The RDG assumes high values at points in space with low electron density due to the deviation from homogeneity. This is the case for regions far from the molecule where the electron density decaying to zero. In contrast to that the RDG will

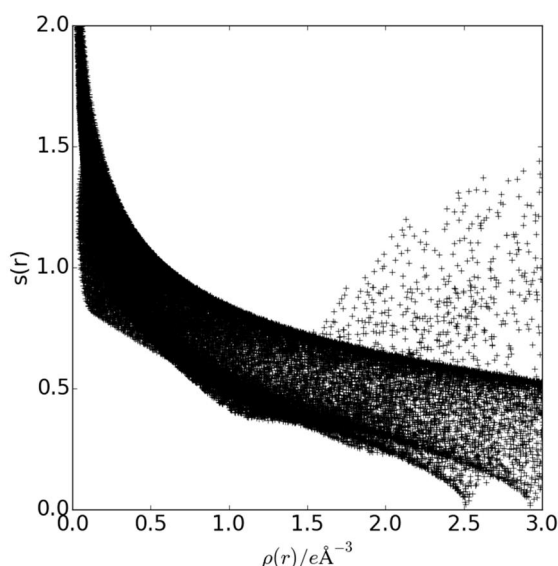


Figure 14: Plot of the RDG versus the electron density in the region of the covalent bond O1 - C1.

approach zero in regions of covalent bonding or non-covalent interactions. Therefore it has been proven worthwhile to investigate plots of the RDG $s(r)$ versus the electron density $\rho(r)$. Figure 14 shows one of these plots in the region of the O1 - C1 bond. A typical course for a covalent bonding can be observed. In the low electron density region relatively far

away from the molecule the reduced density gradient adopts high values. When moving towards the covalent bond (regions of higher electron density) the reduced density exponentially decays. Because bond critical points represent saddle points in the electron density ($\nabla\rho = 0$) the RDG vanishes at these points ($s(r) = 0$). This means that in Figure 14 the spikes in the lower right part of the plot correspond to bond critical points. The fact that two bond critical points appear within in the plot is a consequence of the size of the grid from which the plot is calculated. In fact in the plot two covalent bonds are displayed, first the O1 - C1 bond ($\rho(BCP) = 2.517(6)e\text{\AA}^{-3}$) and second the O2 - C1 bond ($\rho(BCP) = 2.927(7)e\text{\AA}^{-3}$).

The plot in Figure 15 shows a new feature in contrast to the former one. A spike in the region around $0.5 e\text{\AA}^{-3}$. The cuboid grid from which this plot is calculated is centred in the region of the hydrogen bond of the oxalic acid water dimer. The spike

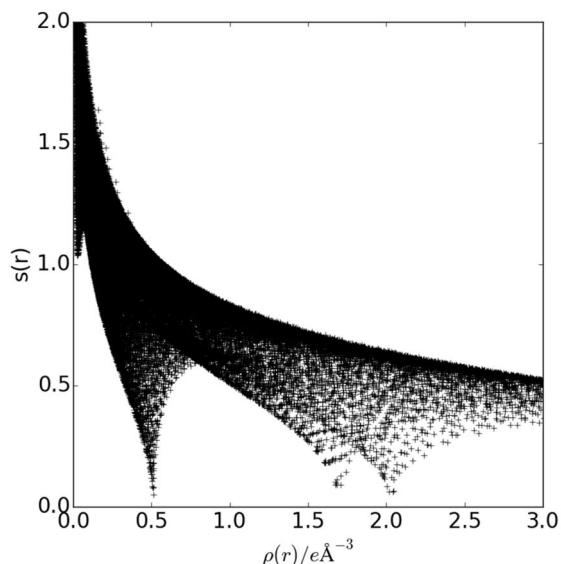


Figure 15: Plot of the RDG versus the electron density in the region of the O3 - H1 hydrogen bond.

stems from the hydrogen bond. These non-covalent interactions are thus characterised by a steep decay of the RDG in a region of low electron density. The spikes at around $1.7 \text{ e}\text{\AA}^{-3}$ and $2.0 \text{ e}\text{\AA}^{-3}$ correspond to the oxygen hydrogen bond in the oxalic acid and the water molecule.

In the QTAIM framework, the Laplacian of the electron density is used to distinguish different interaction types.^[42] This lead to the distinction between covalent and electrostatic interactions (cf. Chapter 2.3). The Laplacian can be decomposed into the contributions along the three principal axis. These contributions correspond to the eigenvalues ($\lambda_1 \leq \lambda_2 \leq \lambda_3$) of the diagonal matrix of the second derivatives of the electron density (Hessian matrix).

$$H(\mathbf{r}) = \begin{pmatrix} \frac{\partial^2 \rho}{\partial x^2} & \frac{\partial^2 \rho}{\partial x \partial y} & \frac{\partial^2 \rho}{\partial x \partial z} \\ \frac{\partial^2 \rho}{\partial y \partial x} & \frac{\partial^2 \rho}{\partial y^2} & \frac{\partial^2 \rho}{\partial y \partial z} \\ \frac{\partial^2 \rho}{\partial z \partial x} & \frac{\partial^2 \rho}{\partial x \partial y} & \frac{\partial^2 \rho}{\partial z^2} \end{pmatrix} \quad (14)$$

The eigenvalues are used to gain further insight into the bonding situation. For noncovalent interactions, both bonding and nonbonding, The Laplacian is dominated by the positive contribution of λ_3 . Van der Waals interactions and hydrogen bonds for example exhibit a negative value ($\lambda_2 \leq 0$) while steric crowding or other repulsive interactions lead to charge depletion and the sign of λ_2 is positive ($\lambda_2 > 0$). Thus, when the RDG is plotted against the quantity $\text{sign}(\lambda_2) \cdot \rho(\mathbf{r})$ repulsive and attractive interactions can be distinguished. An example is shown in Figure 16. It can be seen that for oxalic acid repulsive as well as attractive non covalent interactions are present. Unfortunately, the 2-dimensional plots do not

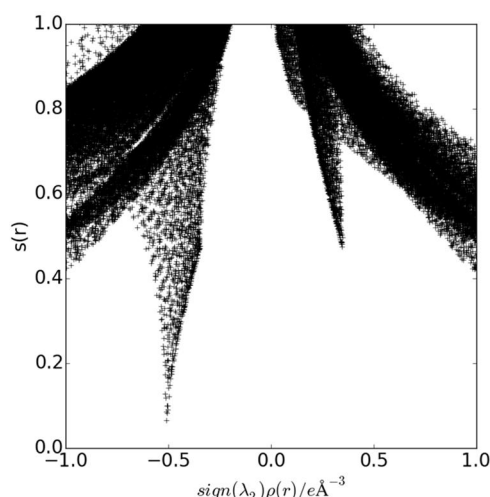


Figure 16: Plot of the $\text{sign}(\lambda_2) \cdot \rho(\mathbf{r})$ vs the reduced density gradient for oxalic acid.

carry any information of the region in which the non-covalent interactions occur. An elegant way to visualise noncovalent interactions is to calculate three-dimensional grids and then map $\text{sign}(\lambda_2) \cdot \rho(\mathbf{r})$ onto the RDG (cf. Figure 17). It is important not to confuse these isosurfaces with the widely used isosurface representations of the Laplacian. It seems that a level of 0.5 is a frequently used value for these isosurfaces, but

other values may also be used. In Figure 17 it can be seen that at a reduced density gradient of value 0.5 an isosurface in between the hydrogen and the oxygen atom is located. From the sign of the mapped quantity the decision if the interaction is attractive (negative sign, marked in red in Figure 17) or repulsive (positive sign, marked in green). The absolute value of $\text{sign}(\lambda_2) \cdot \rho(\mathbf{r})$ can be used to estimate the strength of the interactions. Higher absolute values indicate stronger interactions.

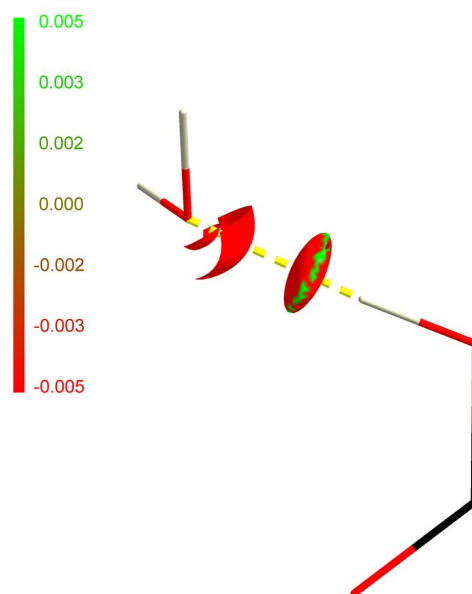
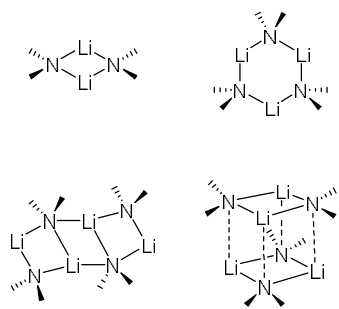


Figure 17: $\rho \cdot \text{sign}(r)$ mapped onto the reduced density gradient $s(r)$ in the region of the hydrogen bonding in the oxalic acid water co crystal at a level of 0.5. Red indicates attractive interaction, green repulsive interaction.

3 Charge Density Analysis of Lithium[2,5-bis((dimethylamino)methyl)pyrrolide]

Lithium amides are among the most widely used organometallic reagents in organic synthesis.^[46,47] They are easily prepared by reacting n-Butyl lithium with



Scheme 1: Examples of lithium amide solid state structures.

the amine. Starting from the monomeric to the di- and trimeric up to polymeric species lithium amides can adopt a wide range of geometries of these

oligomeric species have been the subject of many sophisticated crystallographic studies in the 1990s^[48–52]. A repeating pattern in the solid-state structures of lithium amides is the laddering or stacking of (LiN)_x-membered rings (see Scheme 1). The smallest repeating unit in this laddering and stacking patterns is the lithium amide dimer. In most cases, another feature of these dimeric lithium amides is the asymmetric bonding situation within the Li₂N₂ ring. From a total of 498 structures reported to the Cambridge Structural Database (CSD) containing the central Li₂N₂ ring only 24 show a symmetric bond length distribution.^[53] For the others the bond lengths from one nitrogen to the lithium atoms differ by up to 0.761 Å. An example of this asymmetry is given in [C₆H₅N(H)Li · 2 thf]₂ and [C₆F₅N(H)Li · 2 thf]₂ (Figure 18).^[51] Von Bülow *et al* explained the differences in bond length with a rehybridisation of the deprotonated anilides from sp³ to sp².^[51] This does not only explain the differences in the lithium nitrogen bonds (Li1-N1 1.989 Å, Li1A-N1 2.087 Å) but also the shortening of the N1-C1 bond (1.365 Å) in comparison to aniline (1.39 Å)^[54].

Despite the structural aspects of these amides, the nature of the lithium – nitrogen bond has as well been in the focus of research. Several theoretical studies with differing approaches, methods and basis sets yielded in different

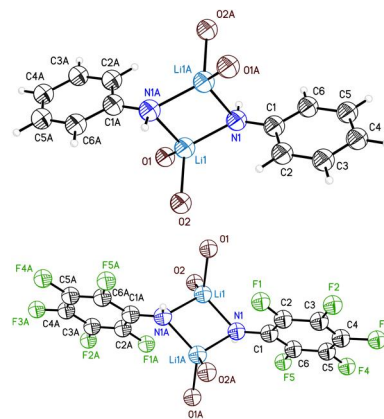
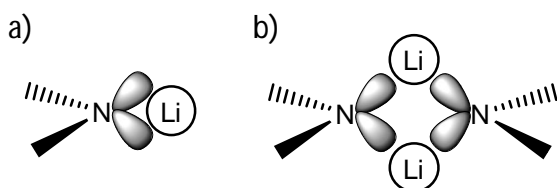


Figure 18: Lithium anilid structures investigated by Bülow *et al*.

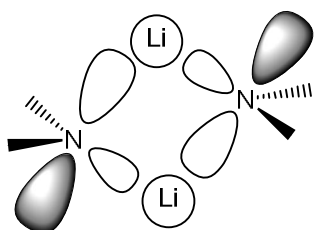
interpretations. Some attribute a significant covalent character^[48,55–61] to lithium amides while others state that the interactions are purely ionic^[62].



Scheme 2: Orbital interactions according to *Fressigné et al.*

Accordingly, the dimer is built up from two pyramidal sp^3 hybridised amide residues interacting with two lithium atoms (Scheme 2b). This would most likely result in equal bond lengths for the lithium – nitrogen bonds.

Having seen that most of the dimeric lithium amides are asymmetric this approach seems contradictory. While *Fressigné et al* chose the Electron



Scheme 3: Orbital interactions as proposed by *Pople et al* and *Weinhold et al.*

Localisation Function (ELF)^[63] framework as their tool *Pople et al*^[57] and *Weinhold et al*^[61] used Population Analysis to analyse monomeric lithium amides. They stated that the lithium atom may benefit from a π conjugation of one of its vacant p orbitals with the p_z orbital of a sp^2 nitrogen atom (Scheme 3). A dimerization of this type of monomer would result in an asymmetric bonding situation with alternating bond length and one lithium closer to the amide plane. This does resemble the observed structures.

To contribute to the discussion from an experimental point of view a high resolution, low temperature dataset of lithium[2,5-bis((dimethylamino)-methyl)pyrrolide] (**1**) was collected. **1** was first synthesised by *Kuo et al*^[64], however only a room temperature dataset has been recorded at that time. With the ability to record a data set at low temperature first, the bond length can be

determined more precisely and through the high resolution, a multipole model refinement and subsequent analysis within the QTAIM framework are possible.

3.1 Data collection and data processing

The synthesis of **1** was carried out by *C. Maaß*. Colorless crystals have been obtained by recrystallization from diethyl ether at -28°C . A suitable crystal for single crystal X-ray diffraction was isolated with the use of the X-Temp2 device^[65,66]. The crystal was mounted on top of a *MiTeGen micromount*TM with a minimum of inert oil. The mounted crystal was transferred to the goniometer and placed in a nitrogen cold stream (100 K) of a Bruker Kryoflex2. The dataset used was collected by *C. Maaß* on a *Bruker D8 Ultra* diffractometer equipped with a *Turbo X-ray Source* (TXS) molybdenum rotating anode. The data collection strategy was calculated with the COSMO^[67] plugin within the APEX2^[68] suite. The raw data were reduced with SAINT v8.30C^[69] and subsequently scaled and corrected for absorption with SADABS 2014/5^[16]. The data statistics have been determined with XPREP 2015/1^[70] (see Table 3). Due to the R_{int} which was above 20% the resolution was cut at 0.45 Å. The high quality of this data set (redundancy of up to 6 and completeness of ~99 %) made a multipole refinement and the subsequent analysis within the QTAIM framework feasible.

Table 3: Statistics from XPREP 2014/5 after scaling and absorption correction with SADABS 2014/5

d [Å]	#Data	#Theory	Compl.	Red.	$\langle I \rangle$	$\langle I/\sigma \rangle$	R_{int}	R_{sigma}
Inf-1.84	445	445	100	30.62	41.6	71.04	0.0419	0.0102
1.84-1.21	1053	1053	100	36.25	10.6	66.16	0.051	0.0106
1.21-0.95	1540	1540	100	25.84	5.4	54.38	0.0593	0.0124
0.95-0.83	1477	1477	100	15.35	2.3	45.05	0.0513	0.0152
0.83-0.75	1553	1553	100	17.67	1.5	46.95	0.0527	0.0146
0.75-0.7	1380	1381	99.9	18.55	1.6	49.88	0.0452	0.0136
0.7-0.66	1425	1425	100	18.02	1.2	46.19	0.0541	0.015
0.66-0.62	1785	1785	100	16.86	0.9	39.61	0.0644	0.0174
0.62-0.59	1700	1700	100	15.53	0.6	32.19	0.0742	0.0217
0.59-0.57	1298	1298	100	14.77	0.6	29.57	0.0829	0.0239
0.57-0.55	1530	1530	100	14.38	0.4	24.04	0.1079	0.0312
0.55-0.53	1764	1765	99.9	13.76	0.3	19.51	0.1373	0.0399
0.53-0.52	970	970	100	13.22	0.2	16.53	0.1576	0.0472
0.52-0.5	2216	2217	100	11.07	0.2	15.02	0.1517	0.0544
0.5-0.49	1231	1231	100	10.14	0.2	12.42	0.1709	0.067
0.49-0.48	1367	1367	100	9.65	0.2	11.4	0.1866	0.0756
0.48-0.47	1458	1458	100	8.27	0.1	10.49	0.1759	0.0836
0.47-0.46	1567	1567	100	7.11	0.1	9.02	0.18	0.0991
0.46-0.45	1770	1770	100	6.77	0.1	8.48	0.1886	0.1098
0.45-0.44	2023	2080	97.3	6.15	0.1	7.04	0.2202	0.1372
0.54-0.44	13531	13590	99.6	9.1	0.2	11.57	0.1649	0.0739
Inf-0.44	29552	29612	99.8	14.39	1.8	28.19	0.0523	0.0151

3.2 Structure solution and refinement (IAM)

The reflection statistics given by XPREP 2015/1 gave rise to the space group $P2_1/c$. The structure was solved with SHELXT^[71], which confirmed the space group. The IAM refinement was carried out with SHELXL^[72] in a straightforward

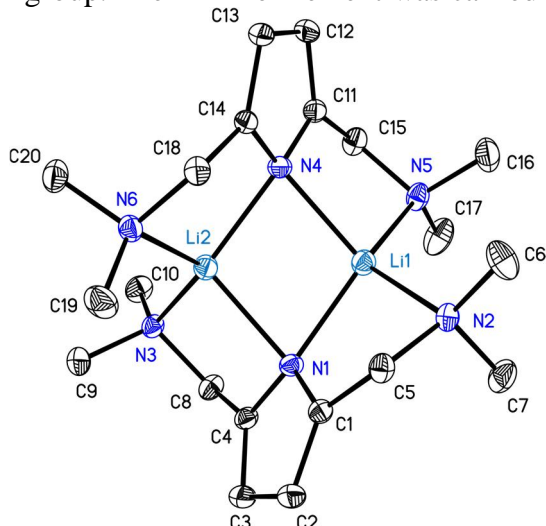


Figure 20: Graphical representation of the content of the asymmetric unit of **1**. Thermal displacement parameters are depicted at a level of 50%. Hydrogen atoms have been omitted for clarity.

manner. All atom positions could be assigned from the Fourier density difference map and all non-hydrogen atoms were refined with anisotropic displacement parameters. The full molecule is contained within the asymmetric unit (see Figure 20). The hydrogen atoms were placed with the appropriate HFIX command implemented in SHELXL. A riding hydrogen model was applied. The hydrogen atoms were refined isotropic.

Their isotropic displacement parameter has been fixed to 1.5 times the U_{eq} of the pivot atom for the four methyl group hydrogen atoms and 1.2 times for all other hydrogen atoms.

3.3 General discussion of the IAM of **1**

The striking feature of this structure is the asymmetry of the central $(LiN)_2$ -ring. It can be seen that the bond lengths within this motif differ in an alternating

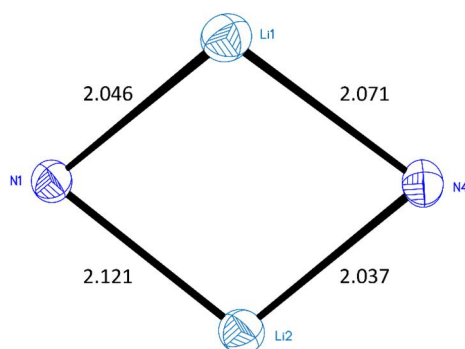


Figure 19: Detail of the crystal structure of **1**. Bond length in units of Å.

way. Each nitrogen has a longer and a shorter distance to Lithium (see Figure 19). Additionally, the bonds do not obey any inversion symmetry which means nitrogen N4 shows significantly different bond distances than N1. The bond distances range from 2.071 Å to 2.121 Å. It is also interesting, that the difference in bond length

is bigger at N1 ($\Delta d = 0.0751 \text{ \AA}$) than at N4 ($\Delta d = 0.0343 \text{ \AA}$). From the crystallographic point of view bond lengths are often correlated to bond strengths. This refers back to *Badger* who correlated bond force constants to internuclear distances in di- and polyatomic molecules.^[73,74] Yet, recent publications seemingly falsified this relationship.^[75,76] For some compounds even an inverse bond length – bond strength relationship has been proposed.^[77] It has, however, to be noted that *Kraka et al*^[77] as well as *Kaupp et al*^[75,76] concluded that these are rare and almost exclusively seen for highly electronegative elements carrying lone pair electrons, such as fluorine. A possible explanation may be the lone pair – lone pair repulsion.^[78,78] Since these conditions are not fulfilled here the first simple presumption is made that the lithium bonds decrease in strength with their length.

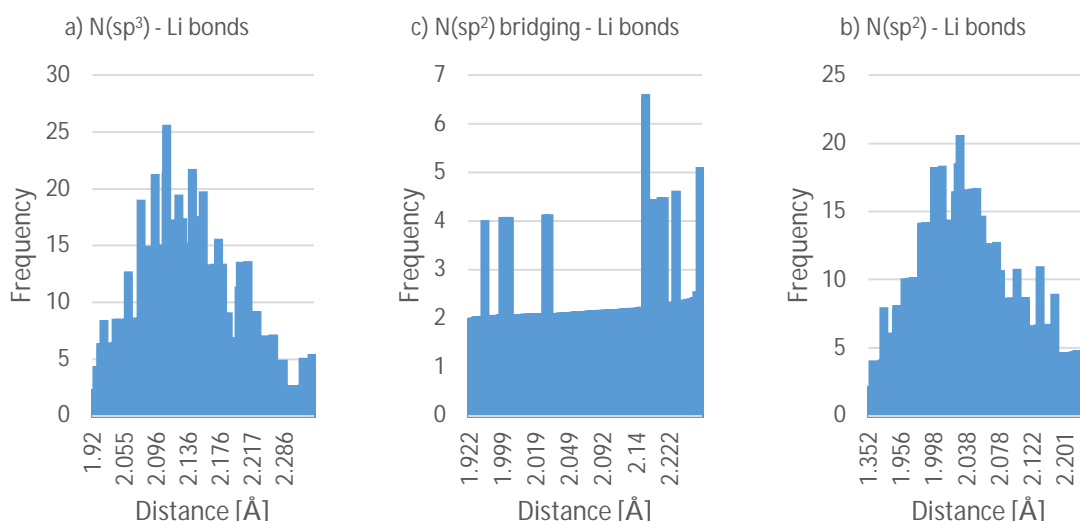


Figure 21: Histograms of the frequency of bond distances for N(sp³), N(sp²) and bridging N(sp²) - Li bonds

Of course, this has to be confirmed by the subsequent analysis within the QTAIM framework.

Additional to the four N(sp²) – Li bonds there are four N(sp³) – Li bonds. These stem from the side arms of the pincer-type ligand. The bond lengths thereof range from 2.1039(4) Å to 2.1322(4) Å (cf. Table 4). A search in the Cambridge Structural Database (CSD) for N(sp²) atoms coordinating one or two lithium atoms and N(sp³) – lithium bonds was carried out to see if the bond lengths found in this work are within or out of the normal range.^[53] For the amine nitrogen atoms (Figure

21a) the most frequent bond length is 2.108 Å while for the N(sp²) atoms bridging two lithium atoms no clear tendency is observable (Figure 21b). In contrast to the other histograms there is no continuous distribution but small peaks emerge. One

Table 4: Bond length for N(sp³) - Li bonds from the side arms

Bond	d / Å
Li1 - N2	2.1165(4)
Li2 - N3	2.1163(4)
Li1 - N5	2.1322(4)
Li2 - N6	2.1039(4)

of these peaks is around 2.030 Å. For comparison N(sp²) atoms coordinating only one lithium atom have been searched. There the most frequent bond lengths also show around 2.030 Å with the most frequent at 2.029 Å (Figure 21c). This means that the lengths of the amine nitrogen - lithium bonds in molecule **1** are within the expected range. Two of the N(sp²) - Li bonds (N1 - Li1 and N4 - Li2) show bond lengths in a range with slightly higher frequency for non-bridging nitrogen. The other two bonds (N1 - Li2 and N4 - Li1) are neither for bridging nor for non-bridging N(sp²) atoms in a range with increased frequency.

Besides the bond lengths, the distances of the lithium atoms to the pyrrole mean planes also show a high degree of asymmetry. For the plane containing N1, C1, C2, C3 and C4 the distances are 0.544 Å to Li1 and 1.528 Å to Li2. So Li1 is clearly much closer to the pyrrole plane than Li2. Looking at the situation at the other plane (containing N4, C11, C12, C13 and C14) one lithium atom (Li2) is still closer (0.921 Å) to the plane but not that much (distance Li1 - plane(N4,C11,C12,C13,C14) = 1.298 Å). As it happens this is also the ligand molecule, which as discussed earlier, shows the smaller difference in N - Li bond length.

To check whether or not this asymmetry is a common motif in dimeric lithium amide structures an extensive search in the Cambridge Structural Database (CSD) for all structures with a Li₂N₂ unit, not containing more than two lithium atoms was carried out. Distances and planes were defined according to Figure 22. 155 structures were found in version 5.37 of the CSD. For each nitrogen atom d₁ and d₂ represent the two bond distances to lithium atoms 1 and 2, while d₃ and d₄ are

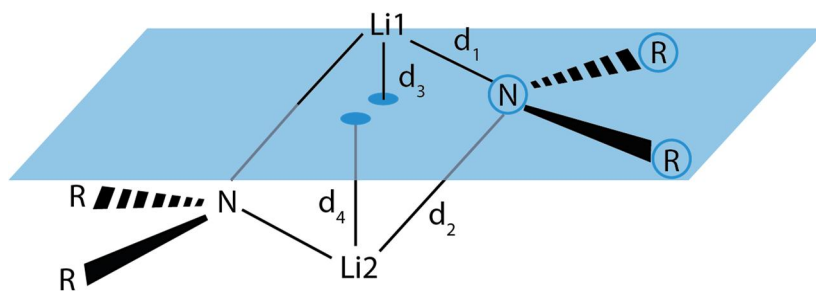


Figure 22: Definition of the Li-N bond distances d_1 and d_2 , and the distances d_3 and d_4 from the lithium atoms to the RNR plane.

calculated as the distances of lithium atom 1 and 2 to the plane containing the nitrogen atom

and its two next non-metallic bonding partners. For a bonding situation outlined in Scheme 3 we expect d_1 and d_2 to differ and the lithium atom with the shorter N-Li distance to be closer to the nitrogen plane. The latter would lead to the fact that the differences $d_1 - d_2$ and $d_3 - d_4$ have the same sign. Therefore, we plotted $d_1 - d_2$ against $d_3 - d_4$ (cf. Figure 23). The correlation between these two values is calculated to 49.1%. 118 data points (blue) fulfil our expectations while the red ones (37) disagree.

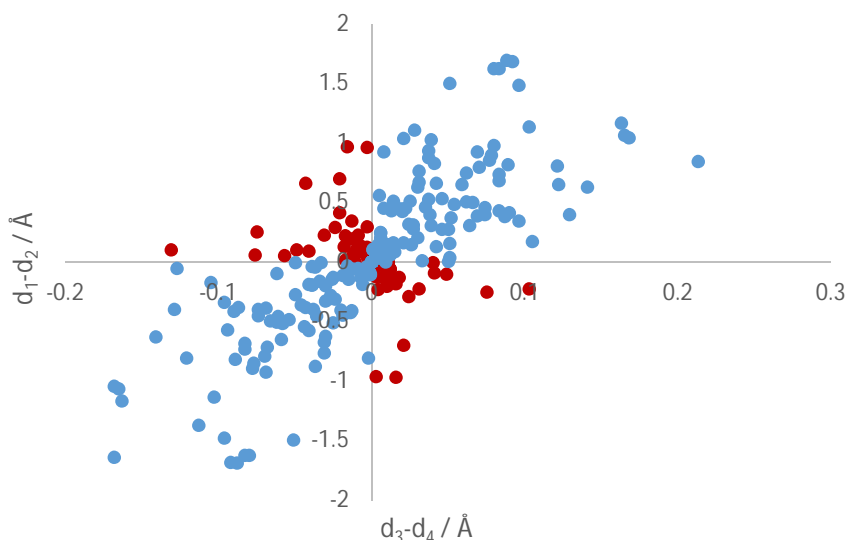


Figure 23: Plot of d_1-d_2 vs d_3-d_4 .

3.4 Multipole model refinement

For the multipole model refinement, the existing IAM refinement was used as a starting point. The model was modified so that the hydrogen atoms were no longer set with an HFIX command on idealised positions but the positions thereof were

identified by difference Fourier analysis. The resulting IAM was taken and the hydrogen atoms were moved to neutron distances along their bond vectors.^[79]

On the basis of this modified routine structure the starting model for the multipole refinement with the XD2006 program suite^[29] has been created with the XDINI program.

The resulting *.mas files need to be modified so that local coordinate system, highest order of multipoles and order of thermal parameters fit to the necessities of the current compound. For the carbon and nitrogen atoms the highest order of multipoles was set to hexadecapoles. Different expansion-contractions parameters κ and κ' were used for the individual atom types and atoms of the same type in different chemical environments. The local coordinate systems were set up so that the highest reasonable symmetry could be used (see Table 5). The hydrogen atoms were refined with monopole and bond directed dipole and quadrupole. The expansion-contraction parameters κ and κ' were fixed to the values proposed by Volkov et al ($\kappa = 1.1$; $\kappa' = 1.18$).^[80] As previous studies showed, refining valence

Table 5: Definition of the local coordinate systems (columns one to five) for the non-hydrogen atoms of compound 1. Maximum level of thermal parameters (TP), maximum level of multipoles (LMX), local symmetry (Site Symm) and chemical constraints (Chem Con)

Atom	Atom 1	Ax1	Atom 2	Ax2	R/L	TP	LMX	Site Symm	Chem Con
N(1)	C(1)	X	C(4)	Y	R	2	4	m	
N(2)	Li(1)	X	C(5)	Y	R	2	4	m	
N(3)	Li(2)	X	C(8)	Y	R	2	4	m	N(2)
N(4)	C(11)	X	C(14)	Y	R	2	4	m	N(1)
N(5)	Li(1)	X	C(15)	Y	R	2	4	m	N(2)
N(6)	Li(2)	X	C(18)	Y	R	2	4	m	N(2)
C(1)	N(1)	X	C(2)	Y	R	2	4	m	
C(2)	C(1)	X	C(4)	Y	R	2	4	m	
C(3)	C(4)	X	C(1)	Y	R	2	4	m	C(2)
C(4)	N(1)	X	C(3)	Y	R	2	4	m	C(1)
C(5)	C(1)	X	N(2)	Y	R	2	4	m	
C(6)	N(2)	Z	H(6C)	X	R	3	4	3m	
C(7)	N(2)	Z	H(7B)	X	L	3	4	3m	C(6)
C(8)	C(4)	X	N(3)	Y	R	2	4	m	C(5)
C(9)	N(3)	Z	H(9B)	X	R	3	4	3m	C(6)
C(10)	N(3)	Z	H(10C)	X	L	3	4	3m	C(6)
C(11)	N(4)	X	C(12)	Y	R	2	4	m	C(1)
C(12)	C(11)	X	C(14)	Y	R	2	4	m	C(2)
C(13)	C(14)	X	C(11)	Y	R	2	4	m	C(2)
C(14)	N(4)	X	C(13)	Y	R	2	4	m	C(1)
C(15)	C(11)	X	N(5)	Y	R	2	4	m	C(5)
C(16)	N(5)	Z	H(16B)	X	R	3	4	3m	C(6)
C(17)	N(5)	Z	H(17C)	X	L	3	4	3m	C(6)
C(18)	C(14)	X	N(6)	Y	R	2	4	m	C(5)
C(19)	N(6)	Z	H(19C)	X	R	3	4	3m	C(6)
C(20)	N(6)	Z	H(20B)	X	L	3	4	3m	C(6)
Li(1)	N(6)	Z	N(4)	X	R	2	0		
Li(2)	N(2)	Z	N(1)	X	R	2	0		

Table 6: Detailed description of the refinement strategy (Abbreviations: Sca: scale factor (refined in every step, only mentioned in the first one); CC: chemical constraints; LS: local symmetry; SIGOBS: data with I/σ smaller than the number is excluded from the refinement; M: monopoles; D: dipoles; Q: quadrupoles; O: octapoles; H: hexadecapoles; κ , κ' : expansion-contractions parameters; (H)XYZ: positional parameters; U2: displacement parameters; U3: third order Gram-Charlier coefficients).

#	Parameter Groups	SIGOBS	CC	LS
1	Sca	3	1	1
2	M	3	1	1
3	D Q O H	3	1	1
4	M D Q O H	3	1	1
5	U2	3	1	1
6	M D Q O H	3	1	1
7	U2 M D Q O H	3	1	1
8	XYZ	3	1	1
9	XYZ M D Q O H	3	1	1
10	XYZ U2 M D Q O H	3	1	1
11	κ	3	1	1
12	M	3	1	1
13	M κ	3	1	1
14	XYZ U2 M D Q O H	3	1	1
15	κ	3	1	1
16	XYZ U2 M D Q O H κ	3	1	1
17	XYZ U2 M D Q O H	3	1	1
18	HXYZ	3	1	1
19	XYZ U2 M D Q O H	3	1	1
20	XYZ U2 M D Q O H κ	3	1	1
21	κ'	3	1	1
22	XYZ U2 M D Q O H κ	3	1	1
23	XYZ U2 M D Q O H κ	2	1	1
24	XYZ U2 M D Q O H κ	1	1	1
25	XYZ U2 M D Q O H κ	0	1	1
26	DQOH	0	1	0
27	XYZ U2 M D Q O H	0	1	0
28	XYZ U2 M D Q O H κ	0	1	0
29	XYZ U2 M D Q O H κ	0	1	0
30	U3	0	1	0
31	XYZ	0	1	0
32	XYZ U3 U2 M D Q O H	0	1	0
33	XYZ U3 U2 D Q O H κ	0	1	0
34	XYZ U3 U2 M D Q O H κ	0	1	0
35	XYZ U3 U2 M D Q O H κ	0	1	0
36	XYZ U3 U2 M D Q O H	0	0	0
37	XYZ U3 U2 M D Q O H κ	0	0	0

density at alkaline metals proves to be challenging^[81–86]. Refinement of a monopole for the lithium atom has been tried but initial steps suggested a lack of refinable valence electrons. Hence, lithium was refined as Li^+ using the entry for the cation in the database assembled by *Su, Coppens* and *Macchi*^[87] implemented in XD2006. The monopole population has been evenly distributed over the donor nitrogen atoms.

For the multipole model refinement, the block refinement approach was used. In this approach the complexity of the model is increased in a stepwise manner. One group of parameters, for example the monopole, is refined solely, afterwards all previously

included parameters are refined. At the end of the block all current parameters are refined together and the next block starts.

As discussed in Chapter 1.5 the choice of refinement strategy and the set of refined parameters is crucial to get the best results. Therefore, k-fold cross validation^[24,26,88] was used to judge on the refinement strategy. Specifically, it was used to test whether refining Gram-Charlier coefficients up to third order, loosening chemical constraints and loosening the local symmetry of the atoms would overfit

the data. A strategy was set up that includes all the above mentioned groups of parameters using the block refinement approach (cf. Table 6).

First all monopoles and multipoles are introduced on top of the IAM geometry (steps 1 to 4). Afterwards the thermal parameters and coordinates of the non-hydrogen atoms were added in steps 5 to 10. After every refinement of the coordinates of the heavy atoms the hydrogen atoms were reset to neutron distance along their bond vectors.^[79] Then the expansion-contraction parameter κ , coordinates of the hydrogen atoms and κ' were gradually introduced (steps 11 to 21) and refined. In the next four refinement steps the σ cut-off was lowered to zero so no data was excluded from the refinement. After this the local symmetry of the atoms was disregarded (steps 26 to 29) and third order Gram-Charlier coefficients were introduced (steps 30 to 35). At last the chemical constraints have been taken out of the refinement. Subsequent to the refinement the increase or decrease in R_{work} and R_{free} is calculated for every refinement step (Figure 24).^[24,26]

As already discussed (cf. Chapter 1.5) a decrease in R_{work} in combination with an increase in R_{free} is used as a sign for overfitting. It can be seen that for all steps prior to the loosening of the chemical constraints R_{free} and R_{work} both either increase or decrease. The slight increase in R-value in the steps 23, 24 and 25 is a consequence of the inclusion of (weak) data. This indicates that neither loosening the local symmetry of the atoms nor introducing ten third order Gram-Charlier parameters to the methyl carbon atoms has to be seen as overfitting the data. However, the steps 36 and 37 show a different picture. The disregarding of the chemical constraints shows an increase in R_{free} while the R_{work} decreases. As can be seen from Table 5 only six heavy atoms were refined when chemical constraints were enabled. This means that the number of multipole parameters increases by a factor of more than four (from 150 to 650). To avoid this overfitting, the loosening of the chemical constraints was removed from the strategy.

In addition to the strategy explained above another strategy was tested where the local symmetry was loosened after the introduction of the third order Gram-Charlier coefficients. This was done to test if the change in order results in the conclusion that loosening the local symmetry already overfits the data. This was not the case so the final strategy consists of the steps one to 35 in Table 6.

3.5 Validity of the model

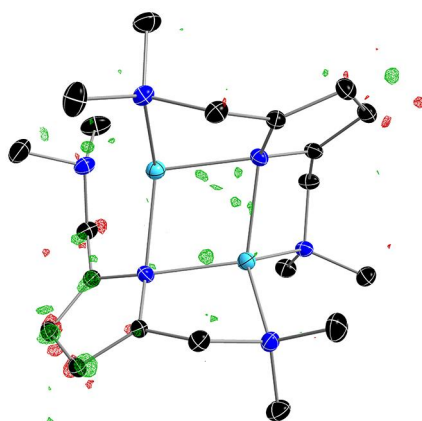


Figure 25: Residual density depicted at a level of 0.1 eA^{-3} . Graphics rendered with MoleCoolQt. The Map generated without any resolution cut offs.

To judge on the validity and quality of the model several diagnostic tools need to be used. First of all, the R -value calculated for the square of the structure factor F is considered. For the present refinement the final $R(F^2)$ equals to 2.60 %. A visual inspection of the residual difference density map shows no significant features (Figure 25). However, slightly higher residual density is visible at the carbon atoms (C11, C12, C13, C14, C15). The

highest peak ($0.159 \text{ e}\text{\AA}^{-3}$) and deepest hole ($-0.178 \text{ e}\text{\AA}^{-3}$) are also located at the carbon atoms C12 and C13. This is probably due to the chemical constraints applied. Despite these deficiencies in modelling the density, inspection of the fractal dimension of the residual density shows a sufficiently flat and featureless distribution (Figure 27). The maximum of the almost paraboloid distribution peaks at $D^f(\text{max}) = 2.759$. The curve exhibits small shoulders in the negative region of the residual density. However the overall course of the curve suggests a flat- and featureless distribution of the residual electron density.^[31]

The plot of the resolution dependence of the ratio between the observed and calculated structure factors reveals some bigger deviations from unity in the low angle as well as in the high angle regions. The comparison of the plots generated with the self-developed program (see Chapter 1.7) and the DRKplot program (cf. Figure 26) shows that these are in close agreement. For the first data points the number of reflections in these bins is significantly smaller than for the others. The first data point for example consists of only two reflections. It is obvious that the individual reflections have a huge influence on the value. The fact that the bins contain an unequal amount of reflections is on the one hand good because the low

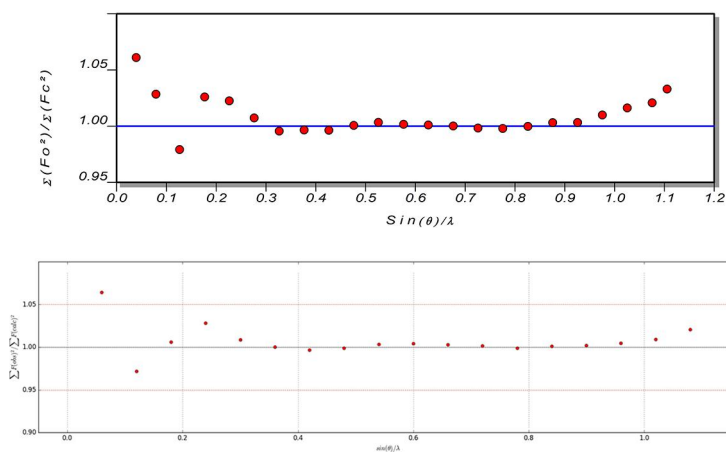


Figure 26: Resolution dependence of the ratio between mean observed and calculated structure factors. The upper one was generated with DRKplot the one below with the self written program (width of bins 0.055 \AA^{-1}).

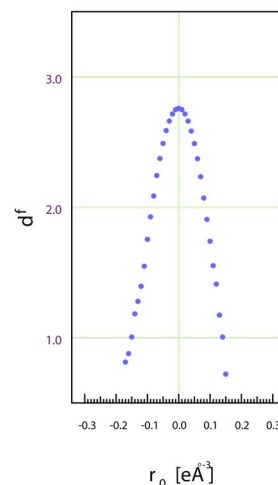


Figure 27: Plot of the fractal dimension of the residual density. $D^f(\text{max}) = 2.759$.

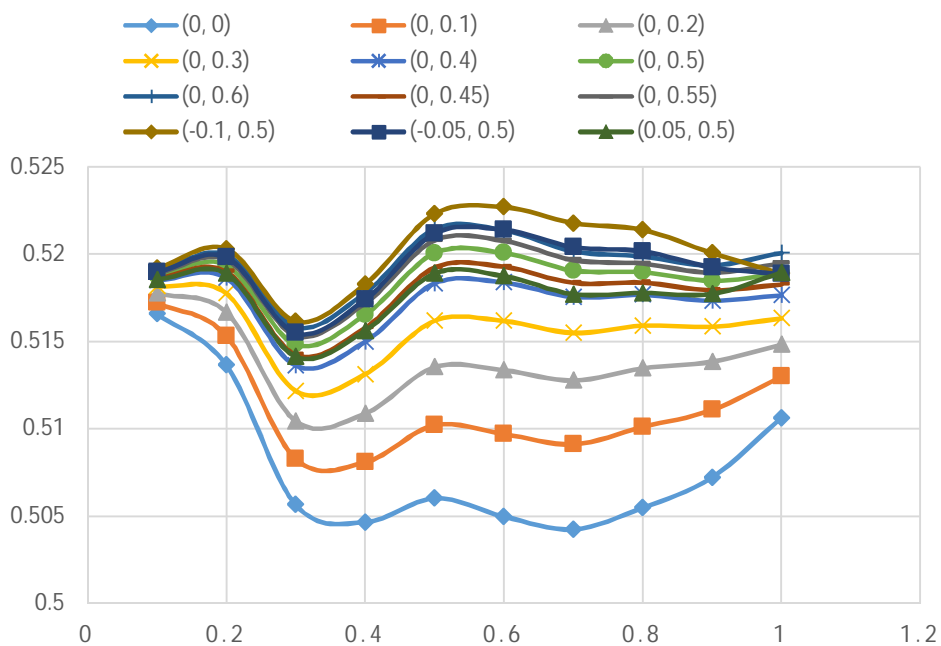


Figure 28: Resolution dependence of the scale factors.

order reflections can easily be identified. On the other hand, the high order bins contain an increasing amount of reflections so individual errors contribute less to the average. The course of the ratio is increasing for high resolutions. *Niepötter et al* concluded that this in combination with residual density at the atomic positions is indicative of resolution dependent errors.^[32] Although no residual density was observed at the atomic positions the method proposed by the authors was tested to see if this appears to be an improvement. The correction factors refined to the values $a = 0.05$ and $b = 0.5$. As can be seen from Figure 28 the course of the scale factors could be slightly improved for the high order part (0.9 to 1.2 Å⁻¹ see Figure 29).

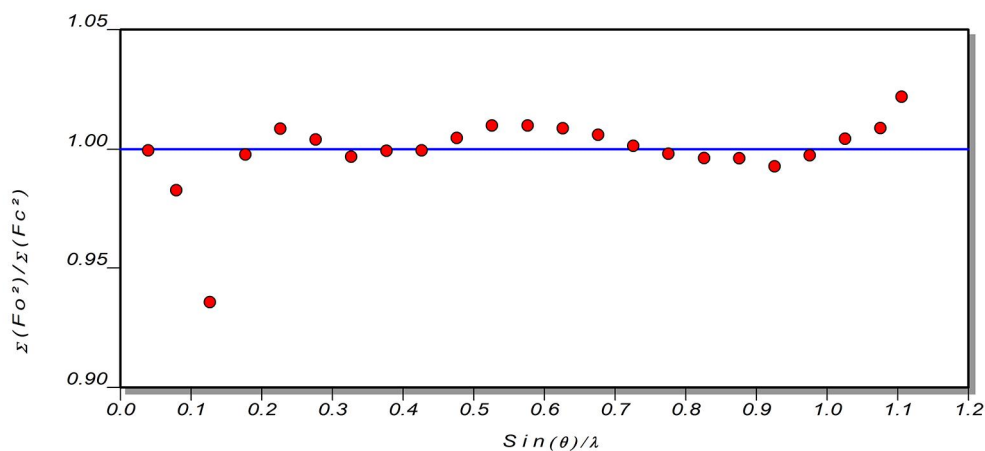


Figure 29: Course of the ratio between mean observed and calculated structure factors after empirical correction as proposed by *Niepötter et al.*^[1]

However, due to the change of the course for the low order reflections (0.0 to 0.2 \AA^{-1}) in combination with the not present residual density at the atomic positions it was decided to not correct for resolution dependent errors using this method. Instead, it was chosen to introduce resolution dependent scaling factors which improved the course of the plot (Figure 30). Table 7 summarizes the crystallographic data after the final MM refinement.

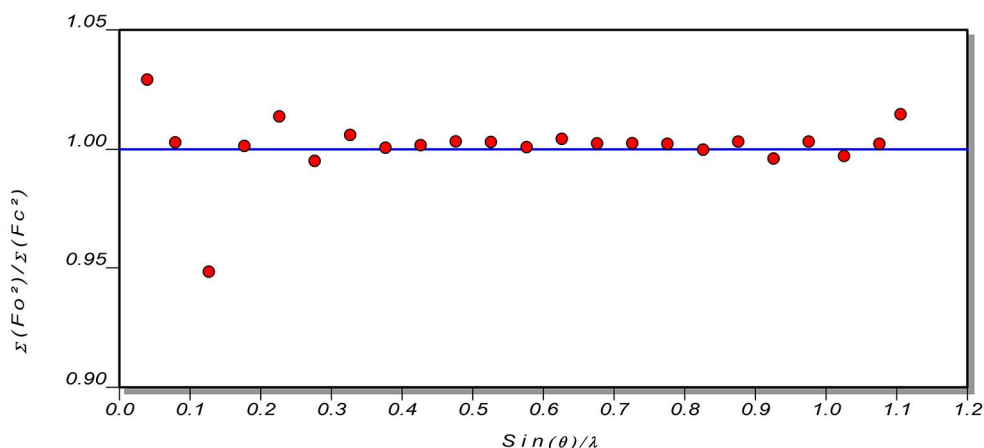


Figure 30: Course of the ratio between mean observed and calculated structure factors after introduction of resolution dependent scaling factors.

Table 7: Crystallographic data for compound 1.

Empirical formula	C H Li N	Absorption coefficient	0.068 mm ⁻¹
Formula weight	33.97	F(000)	782
Temperature	100(2) K	Crystal size	0.200 x 0.200 x 0.200 mm
Wavelength	0.71073 Å	Theta range for data collection	1.595 to 52.175°
Crystal system	Monoclinic	Independent reflections	24493
Space group	P2 ₁ /c	Completeness to theta = 25.242°	97.90%
Unit cell dimensions	a = 12.799(1) Å b = 9.710(1) Å c = 18.674(1) Å	Absorption correction	Semi-empirical from equivalents
	b = 94.26(2)°	Max. and min. transmission	0.7503 and 0.7289
Volume	2314.7(3) Å ³	Refinement method	Full-matrix least-squares on F ²
Z	46	Data / parameters	24649 / 542
Density (calculated)	1.121 Mg/m ³	Goodness-of-fit on F ²	2.2491
		R indices (all data)	R ² = 0.0260, wR ² = 0.0375
		Largest diff. peak and hole	0.159 and -0.189 eÅ ⁻³

3.6 Topological analysis of Lithium[2,5-bis((dimethylamino)-methyl)pyrrolide]

A complete topological analysis within the QTAIM framework has been carried out. First of all, a search for all critical points in the electron density ρ and the associated bond path resulted in the molecular graph shown in Figure 31.

At first glance the molecular graph looks fairly complicated. Nonetheless, the *Poincaré – Hopf* relation^[89] is still satisfied. It can clearly be seen that the automatic routine included in the XDPROP program of the XD2006 program suite^[29] finds many hydrogen-hydrogen interactions. The nature of these interactions is still under discussion.^[90–95] While *Cioslowski et al*^[91] characterise these interactions as repulsive, *Novoa et al*^[93] found in their theoretical study that these interactions have dissociation energies of up to 0.4 kcal/mol. *Wolstenholme et al* did a comparative study on this topic and therein tried to classify these C-H...H-C interactions in contrast to hydrogen bonds (X-H...Y) and dihydrogen bonds.^[94] One difference associated to these interactions is the charge of the hydrogen atoms involved. While for C-H...H-C interactions both hydrogen atoms bear a positive charge in dihydrogen bonds one bears a positive charge the other a negative one. From Table 11 (see page 42) it is evident that for the interactions found in this study all hydrogen atoms bear a rather small positive charge. *Koch* and *Popelier* proposed criteria for

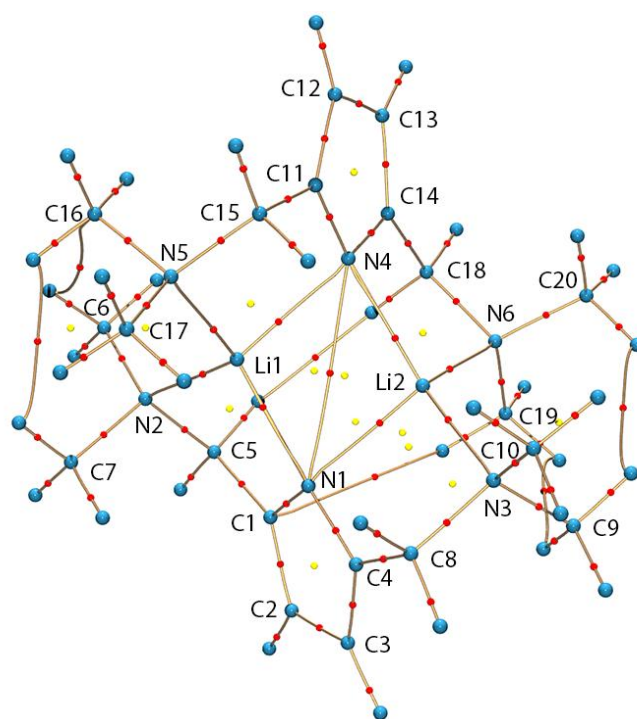


Figure 31: Molecular graph of compound 1. Red spheres: BCPs; yellow spheres: RCPs; blue spheres: atomic positions. Hydrogen atoms not labeled.

Table 8: Electron Density ρ and Laplacian $\nabla^2\rho$, at the BCP linking atoms A and B. ΔR_X values are calculated as van der Waals radius minus distance to BCP

A	B	d / Å	R_{AB} / Å	ρ / eÅ ⁻³	$\nabla^2\rho$ / eÅ ⁻³	ΔR_A	ΔR_B
H20B	H9B	2.3370(0)	2.3647	0.04	0.48	0.0314	0.0121
H9C	H19C	2.4444(0)	2.5013	0.04	0.46	-0.035	-0.0537
H18A	H5A	2.1118(0)	2.1155	0.06	0.6	0.1486	0.1377
H6C	H16B	2.7562(0)	2.8133	0.03	0.42	-0.0964	-0.3122
H16B	H7B	2.5274(0)	2.5621	0.03	0.33	-0.0709	-0.0767

hydrogen
bonding of
which the
first four can
also be

applied to C-H...H-C interactions. [94,94,96] The first criterion is the topology meaning the BCPs as well as the eventually associated RCPs need to be found. The second and third criterion involve the charge density and the Laplacian at the bond critical point. The charge density is expected to be at least an order of magnitude smaller than typical covalent bonds and the Laplacian at the BCP needs to be positive. The fourth criterion is the mutual penetration of the hydrogen and acceptor atom (in this case the other hydrogen atom). From Table 8 it is evident that all of these criteria are fulfilled for the bond path linking H20B and H9B as well as for the one between H18A and H5A. For the other ones the first three criteria are fulfilled but the bond path is significantly longer than the sum of *van der Waals* radii. The values obtained are comparable to those found in the experimental study of *Wolstenholme et al.* [94] Although these interactions are small there might be influence on parts of structures like the conformation of methyl groups. Certainly in this study their influence on the structure is small. Additional to the hydrogen-hydrogen interactions a N-N trans annular interaction can be found. However, the close vicinity of the BCP and RCPs suggest that this is close to a catastrophe point, where these critical points coincide and therefore vanish.

The focus of this study however lies on the nitrogen – lithium interactions. Table 9 summarises the properties at the BCPs for the central Li₂N₂ ring. It can be seen that the shortest bond path (Li2 – N4, $R_{AB} = 2.0368$ Å) also shows the highest values for ρ (0.143 eÅ⁻³) and $\nabla^2\rho$ (4.068 eÅ⁻⁵) at the bond critical point. The BCP associated

with the
second
shortest
bond path

Table 9: Properties at the BCPs for the Li - N interactions within the central Li₂N₂ ring.

A	B	d / Å	R_{AB} / Å	ρ / eÅ ⁻³	$\nabla^2\rho$ / eÅ ⁻⁵	d_A / Å	d_B / Å
Li1	N1	2.0461(0)	2.0463	0.136(1)	4.003(1)	0.7624	1.2839
Li2	N1	2.1212(0)	2.1212	0.110(1)	3.147(1)	0.7890	1.3322
Li1	N4	2.0711(0)	2.0712	0.129(0)	3.718(0)	0.7701	1.3011
Li2	N4	2.0368(0)	2.0368	0.143(0)	4.068(0)	0.7593	1.2775

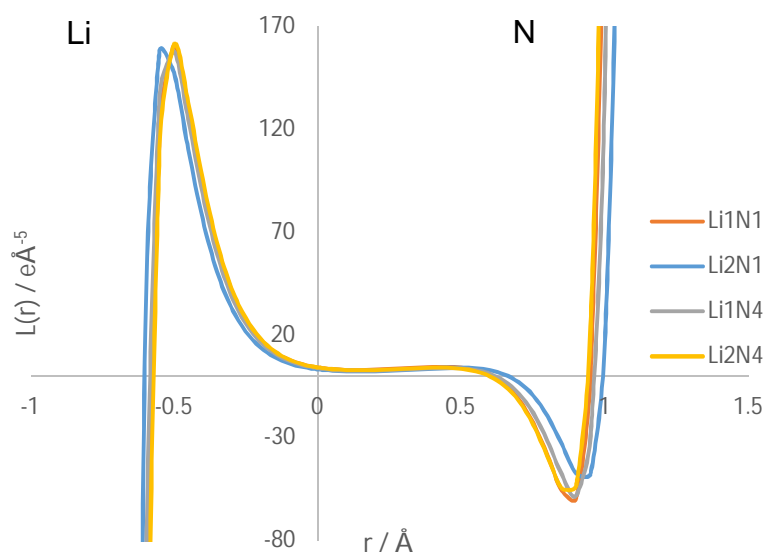


Figure 32: Plot of the Laplacian along the bond path for the lithium nitrogen bonds within the Li_2N_2 four membered ring. The BCP is put to the origin of the plot. Positive values of the abscissa point towards nitrogen, negative ones towards lithium.

are significantly longer ($R_{\text{AB}}(\text{Li1} - \text{N4}) = 2.0712 \text{ \AA}$, $R_{\text{AB}}(\text{Li2} - \text{N1}) = 2.1212 \text{ \AA}$) decrease further in their properties at the BCP. From this it is evident that the properties at the BCPs decrease in correlation with an increase in bond path length. All of the bonds show typical values for open shell interactions. An analysis of the Laplacian distribution along the bond path of the lithium – nitrogen bonds reveals that in fact the longest bond within the Li_2N_2 ring shows a different course than the others (cf. Figure 32). The bonds Li1 – N1, Li1 – N4 and Li2 – N4 show a similar course and a similar local charge density concentration at the nitrogen atom. The local charge density concentration at the Li2 – N1 bond is by about 10 e\AA^{-5} smaller and slightly closer to the nitrogen atom (Figure 32). For comparison the data from

(Li1 – N1), which is only about 0.1 \AA longer exhibits values of ρ (0.136 e\AA^{-3}) and $\nabla^2\rho$ (4.003 e\AA^{-5}) which are comparable to those of the Li2 – N4 bond path.

The other two bond paths which

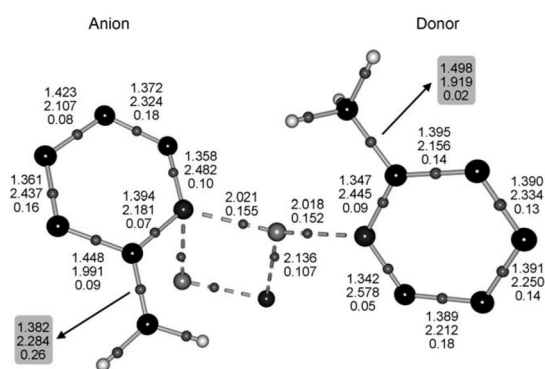


Figure 33: BCPs found for 2-Picolylithium. Upper values denote the bond length [\AA], middle ones ρ [e\AA^{-3}] at the BCP and bottom values are ellipticities ϵ .

Ott et al was used.^[81,82] The bonding situation in 2-Picolylithium is in some points very similar to the studied compound **1**. In Figure 33 the structure as well as properties at the bond critical points are shown. It can be seen that there is also a difference of about 0.9 \AA in bond length and a difference of 0.4 e\AA^{-3} in the electron

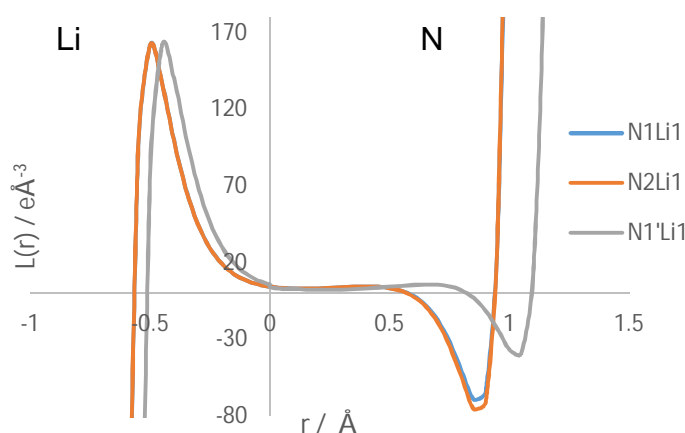


Figure 34: Course of the Laplacian along the bond path for 2-Picolylithium.

nitrogen bond (N1' – Li1) and the non-bridging donor molecule however, look quite similar. Also the local charge concentrations for the N1' – Li1 bond is closer to the nitrogen atom, as in compound **1**. The authors attribute this to the preferred orientation of the lithium towards the lone pair of the nitrogen atom. This conclusion is also in agreement with the current situation. One of the pincer type ligands can form the preferred geometry with one lithium atom closer to the pyrrole plane while the other one is probably not able to achieve this, for steric reasons. The consequence is a compromise where the bond situation is more symmetric and both bonds Li1 – N4 as well as Li2 – N4 show similar values of ρ and a similar course

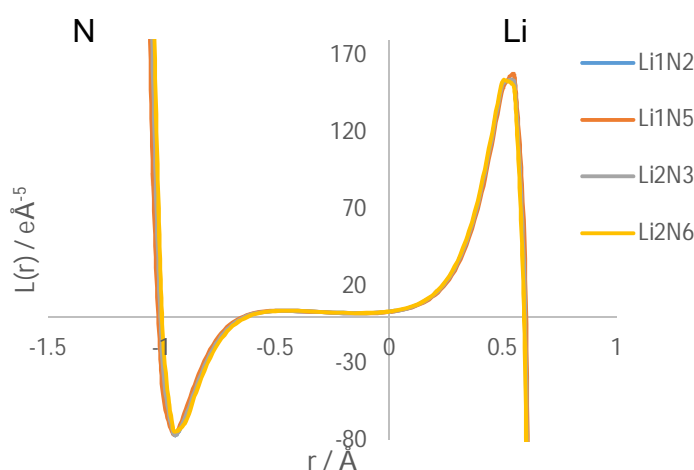


Figure 35: Plot of the Laplacian along the bond path for the lithium nitrogen bonds of the side chain amine nitrogen atoms. The BCP is put to the origin of the plot. Positive values of the abscissa point towards lithium, negative ones towards nitrogen.

density at the BCP. From the course of $\nabla^2\rho$ (see Figure 34) it is clear that, similar to compound **1**, the longest lithium – nitrogen bond (N1' – Li1) is quite different from the other two.

The shorter lithium – nitrogen bond (N1 – Li1) and the non-bridging donor molecule however, look quite similar. Also the local charge concentrations for the N1' – Li1 bond is closer to the nitrogen atom, as in compound **1**. The authors attribute this to the preferred orientation of the lithium towards the lone pair of the nitrogen atom. This conclusion is also in agreement with the current situation. One of the pincer type ligands can form the preferred geometry with one lithium atom closer to the pyrrole plane while the other one is probably not able to achieve this, for steric reasons. The consequence is a compromise where the bond situation is more symmetric and both bonds Li1 – N4 as well as Li2 – N4 show similar values of ρ and a similar course

of $\nabla^2\rho$. As a further comparison the amine nitrogen – lithium bonds can be considered. Figure 35 shows the plot of the Laplacian along the nitrogen – lithium bond path of the pincer side arms. It can be seen that the charge density concentration at the

nitrogen atoms (region of negative values of the abscissa) is higher than at the pyrrole nitrogen atoms (Figure 32). The local minimum of the plot shows a value of approximately $-80 \text{ e}\text{\AA}^{-5}$ for the amine nitrogen atoms while the pyrrole nitrogen atoms only exhibit a minimum of around $-60 \text{ e}\text{\AA}^{-5}$. The higher electron density concentration at the amine nitrogen atoms is certainly a consequence of the more localized sp^3 hybridisation.

The regions of highest charge concentration at the nitrogen atoms of compound **1** also show typical shape of bridging lone pair. In contrast to a singly donating sp^2 -nitrogen atom which shows a more symmetric distribution (cf. *Ott et al*^[81,82]) the isosurface of $\nabla^2\rho$ around the bridging sp^2 -nitrogen atoms in **1** is elongated so both lithium atoms can access the charge concentration (cf. Figure 36). Furthermore it can be seen that the VSCC for nitrogen atom N1 is clearly directed towards Li1 (Figure 36a) while for N4 (Figure 36b) the VSCC is directed towards the angle bisector of the Li1-N4-Li2 angle. This fact is especially evident if the critical points instead of the regions of the Laplacian are considered (Figure 37). For both pyrrole nitrogen atoms the expected number

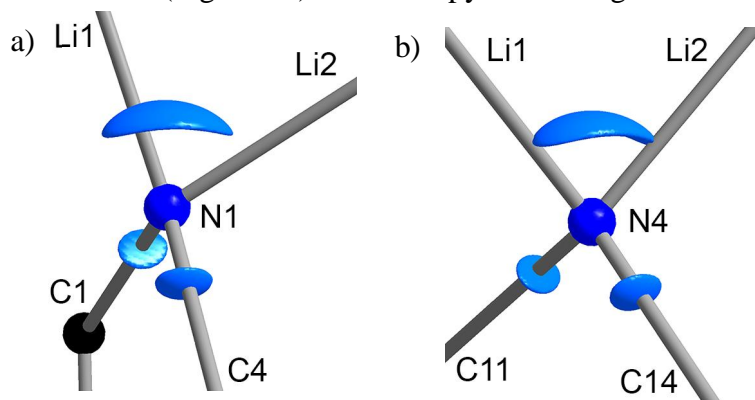


Figure 36: Isosurface representation of $\nabla^2\rho$ around a) N1 and b) N4. Isosurfaces depicted at a level of $-55 \text{ e}\text{\AA}^{-5}$. Atoms depicted as spheres with a radius of 0.1 \AA .

Table 10: Values for the distance d from the critical point to the atomic centre, ρ and $\nabla^2\rho$ for the critical points in $\nabla^2\rho$ of compound **1**. CP1 always denominates the not bond directed critical point.

	CP	$d / \text{\AA}$	$\rho / \text{e}\text{\AA}^{-3}$	$\nabla^2\rho / \text{e}\text{\AA}^{-5}$
N1	1	0.399	3.605	-63.964
	2	0.407	3.579	-58.739
	3	0.407	3.597	-60.656
N4	1	0.399	3.606	-63.963
	2	0.407	3.580	-58.753
	3	0.407	3.595	-60.636
N2	1	0.393	3.915	-78.209
	2	0.410	3.338	-52.884
	3	0.410	3.348	-53.129
	4	0.408	3.404	-57.215
N3	1	0.393	3.912	-78.222
	2	0.410	3.337	-52.958
	3	0.410	3.328	-52.854
	4	0.408	3.401	-57.218
N5	1	0.393	3.952	-78.215
	2	0.410	3.336	-52.885
	3	0.410	3.345	-53.065
	4	0.408	3.398	-57.188
N6	1	0.393	3.915	-78.212
	2	0.410	3.327	-52.696
	3	0.410	3.344	-53.179
	4	0.408	3.399	-57.187

of three critical points could be found.

Furthermore, for the amine nitrogen atoms situated at the side chains all four expected critical points are

observed. In Figure 37, it can be clearly seen that the critical point for N1 almost lies on the connection line between N1 and Li1. Table 10 lists all the critical points and their properties in the Laplacian for the nitrogen atoms in compound **1**. Looking at the values for N1 and N4 it is obvious that the values for ρ at the corresponding critical points (CP1 at N1 and N4 etc.) are nearly identical as well as the distance to the atomic centre (e.g. $\rho(N1_{CP1}) = 3.605 \text{ e}\text{\AA}^{-3}$, $\rho(N4_{CP1}) = 3.659 \text{ e}\text{\AA}^{-3}$). The values of $\nabla^2\rho$ also do not differ significantly. This is also true for the sp^3 amine nitrogen atoms at the side chains. However, while for the sp^2 -nitrogen atoms the values of ρ for the not bond and the bond directed critical points are close to each other (e.g. $\rho(N1_{CP1}) = 3.605 \text{ e}\text{\AA}^{-3}$, $\rho(N1_{CP2}) = 3.579 \text{ e}\text{\AA}^{-3}$, $\rho(N1_{CP3}) = 3.597 \text{ e}\text{\AA}^{-3}$), the not bond directed critical point for the amine nitrogen atoms is significantly higher ($\rho(N2_{CP1}) = 3.915 \text{ e}\text{\AA}^{-3}$, $\rho(N2_{CP2}) = 3.338 \text{ e}\text{\AA}^{-3}$). This is of course a consequence of the incorporation of the sp^2 -nitrogen within the aromatic pyrrole system. This fact is additionally emphasised by the Laplacian $\nabla^2\rho$. The values indicate that the electron density is more concentrated at the amine nitrogen ($\overline{\nabla^2\rho(N_{\text{sp}^3})} = -78.214 \text{ e}\text{\AA}^{-5}$) than at the sp^2 pyrrole nitrogen atoms ($\overline{\nabla^2\rho(N_{\text{sp}^2})} = -63.964 \text{ e}\text{\AA}^{-5}$).

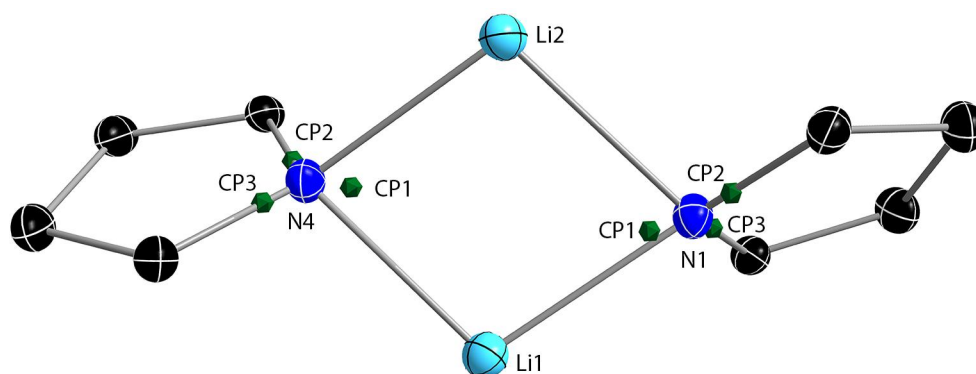


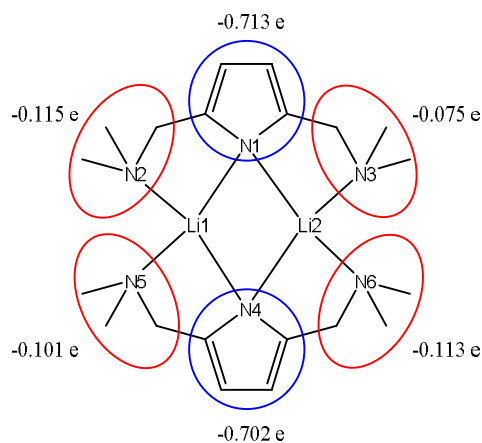
Figure 37: Position of the critical points in $\nabla^2\rho$ (green spheres). Thermal parameters depicted at 50 % probability level.

Table 11: Integrated Bader charges for all atoms in compound 1. Sum of all charges $q = 0.048 e$.

Atom	q/e	Atom	q/e
N1	-0.96	H6A	0.03
N2	-1.04	H6B	0.03
N3	-1.03	H6C	0.02
N4	-0.96	H7A	0.03
N5	-1.03	H7B	0.02
N6	-1.03	H7C	0.03
C1	0.18	H8A	0.08
C2	-0.23	H8B	0.09
C3	-0.23	H9A	0.03
C4	0.19	H9B	0.02
C5	0.14	H9C	0.02
C6	0.23	H10A	0.03
C7	0.23	H10B	0.03
C8	0.16	H10C	0.02
C9	0.24	H12	0.17
C10	0.23	H13	0.17
C11	0.18	H15A	0.08
C12	-0.23	H15B	0.08
C13	-0.23	H16A	0.03
C14	0.19	H16B	0.02
C15	0.14	H16C	0.02
C16	0.23	H17A	0.03
C17	0.23	H17B	0.03
C18	0.13	H17C	0.02
C19	0.23	H18A	0.08
C20	0.23	H18B	0.09
Li1	0.93	H19A	0.03
Li2	0.93	H19B	0.03
H2	0.17	H19C	0.02
H3	0.17	H20A	0.03
H5A	0.08	H20B	0.02
H5B	0.09	H20C	0.03

The integration of the atomic basins resulted in the integrated *Bader* charges (cf. Table 11). Looking at the values calculated for the nitrogen atoms a difference between the pyrrole and the amine nitrogen atoms becomes evident. The pyrrole nitrogen atoms N1 ($q = -0.96 e$) and N4 ($q = -0.96 e$) bear somewhat smaller charges than the amine nitrogen atoms ($\langle q \rangle = -1.03 e$). By summing up the charges to group charges it can be visualised which group of the molecule counterbalances most of the positive charge of the lithium cations. The ligand molecules have been divided in the pyrrole rings and the individual side chains (cf. Scheme 4). Although the amine nitrogen atoms carry a slightly higher charge than the pyrrole nitrogen atoms, the pyrrole rings in total contribute most of the charge ($-1.415 e$)

that counterbalances the positive charge of the lithium atoms ($1.867 e$). The side chain amine nitrogen donor atoms of the pincer ligands fill up the coordination sphere to form a distorted tetrahedron.



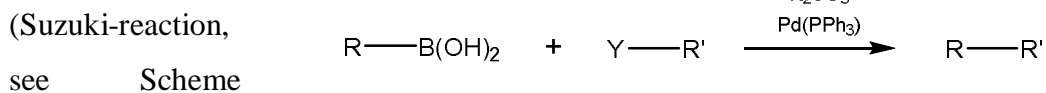
Scheme 4: Calculated Group charges of the ligands from the individual charges of the contained atoms (charge Li1 $q = 0.934 e$; charge Li2 $q = 0.933 e$).

3.7 Conclusion

Due to the high-quality, high resolution dataset obtained on compound **1** a well suited multipole model could be obtained. In the subsequent topological analysis an experiment based approach was added to the contradictory theoretical models explaining the bonding situation of dimeric lithium amides. It could be shown that the theoretical symmetric model of two sp^3 hybridised nitrogen atoms coordinating two lithium atoms proposed by *Fressigné et al*^[62] is rarely found in reality. The electron densities at the bond critical points within the Li_2N_2 ring do show significant differences. Despite the fact that all of the lithium-nitrogen bonds need to be classified as open shell or ionic interactions this shows that they are different. This implies that not only electrostatic interactions are involved. The results obtained within this study are in agreement with the theoretical models proposed by *Pople et al* and *Weinhold et al* who proposed significant contribution of $N(sp^2)$ π -density to the vacant lithium p orbitals in mono- and dimeric lithium amides.^[57,97]

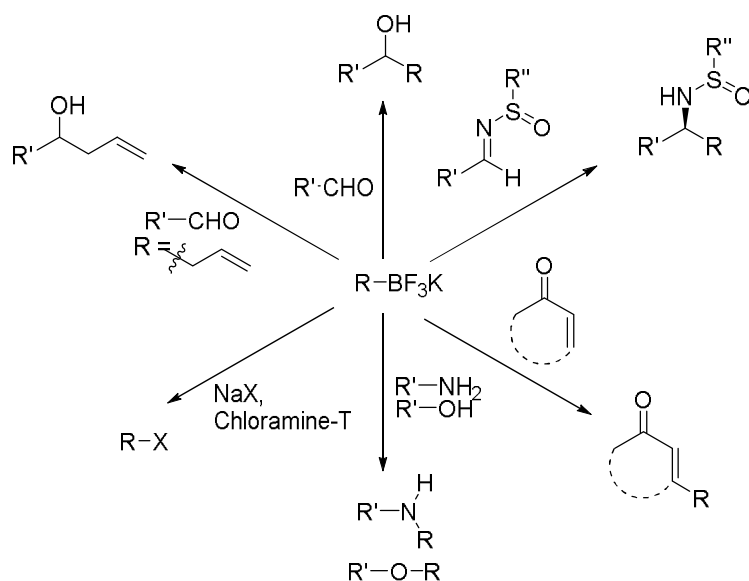
4 Charge Density Analysis of dipotassium phenylene-1,4-bis(trifluoroborate)

Organoboron compounds have proven to be valuable reagents in modern synthesis. An outstanding example, awarded with the Nobel prize in 2010, is the palladium catalysed cross-coupling reaction of organoboronic acids with vinyl and aryl halides



Scheme 5: Reaction scheme of a classic Suzuki coupling.

research by *Genêt et al* and *Xia et al* also enabled the use of organotrifluoroborates in palladium-catalysed C-C bond forming reactions.^[100-103] Besides metal catalysed reactions boronic acids may also be reacted directly with tosylhydrazones.^[104] Organotrifluoroborates also may be reacted directly with a wide variety of substrates to form C-C, C-N and C-O bonds (Scheme 6). Using organoboron compounds, especially organotrifluoroborates, in C-C bond forming reactions show



Scheme 6: Selected reactions feasible with organotrifluoroborates.

some advantages over the wide range of other cross-coupling reactions. Amongst these are the relatively easy access to them, their stability against polymerisation (in contrast to organoboron acids)

and the non-toxic and easy to remove inorganic byproducts. In contrast to the large number of scientific papers focussing on the synthetic use of organotrifluoroborates

the number of detailed structural investigations on them is limited. A search within the CSD resulted in solely 38 structures containing potassium organotrifluoroborates. A recurring pattern within the found structures is the formation of extended networks of close potassium fluorine contacts. A similar type of interactions, C-F \cdots M⁺ interactions, is already subject of many research papers.^[105–110] Undoubtedly these interactions are of small energy. However, it are exactly these weak interactions that are considered to govern the solid state structure according to the concept of crystal engineering.^[111,112] In crystal engineering intermolecular interactions are regarded as building blocks. By choosing the right building blocks, according to *Desiraju*, it would be possible to purposefully design new crystalline materials. To achieve this, it is of great importance to understand these weak interactions. Several efforts have been undertaken to gain insight in a wide range of intermolecular interactions such as C-H \cdots π , C-H \cdots N, O-H \cdots O and $\pi\cdots\pi$.^[113–119] Recent articles add interactions involving organic fluorine to the list.^[120,121]

In 2015 *Falcicchio et al* reported on the interesting solid state structure of dipotassium phenylene-1,4-bis(trifluoroborate) (**2**).^[122] Within their study they

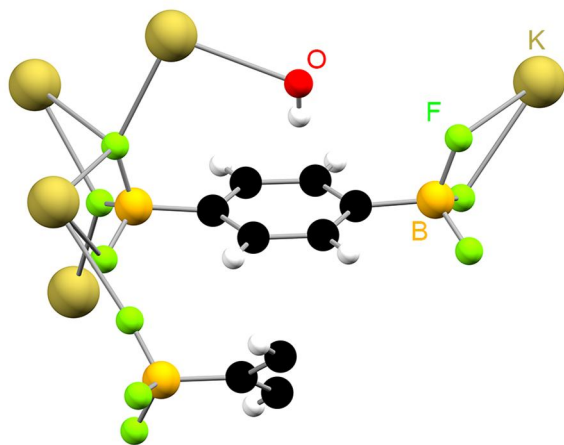


Figure 38: Asymmetric unit of compound **2** as determined by *Falcicchio et al*. Size of the spheres is calculated as 0.19 times the van der Waals radius of the respective atom.

investigated in detail the crystal structure within the IAM. In Figure 38 the asymmetric unit of **2** is shown. The authors focus on short intermolecular contacts. The hydrogen of the water molecule for example points directly towards the benzene ring, forming an O-H \cdots π interaction. A significant part in stabilizing this crystal structure however, seems

to originate from short K⁺ \cdots F contacts. Three out of the five potassium cations in compound **2** show ten short contacts to fluorine. Another one shows eight short contacts and the last one seven close contacts to fluorine, oxygen and carbon atoms.

The found short contacts have subsequently been analysed using DFT calculations by employing M06/LACVP+ (d,p). An analysis within the QTAIM framework showed that each short contact also shows a distinct bond path. In addition, the authors performed the rather recent non-covalent interaction (NCI) analysis and thus were able to theoretically confirm the presence of these interactions.^[45,123]

To complement the results of *Falcicchio et al* with experimental results using the same framework and therefore produce comparable results a high resolution X-ray dataset was recorded and subsequently analysed during this thesis.

4.1 Data collection and data processing

A sample of compound **2** was kindly provided by *Falcicchio et al*. A suitable colourless crystal of needle shaped habit was selected with the use of the X-Temp2 device.^[65] The crystal, mounted to a MiTEGEN MICROMOUNTTM, was directly transferred to the goniometer equipped with a BRUKER KRYOFLEX2 open flow nitrogen cold gas stream device set to 100 K. The data set was collected on a BRUKER D8 ULTRA diffractometer using a BRUKER TURBO X-RAY SOURCE molybdenum rotating anode. The data collection strategy was calculated with the COSMO^[67] plugin as implemented in the APEX2 software suite.^[68] The collected data was integrated with SAINT v8.30C^[69] and SADABS 2014/5^[16] was used for scaling and absorption correction. The data statistics have been determined with XPREP

Table 12: Statistics from XPREP 2014/5 after scaling and absorption correction with SADABS 2014/5

d [Å]	#Data	#Theory	Compl.	Red.	$\langle I \rangle$	$\langle I/\sigma \rangle$	R_{int}	R_{sigma}
Inf - 1.22	1094	1097	99.7	26.35	16.2	82.68	0.0278	0.0092
1.22 - 0.95	1144	1144	100	27.73	4.9	69.77	0.0415	0.0085
0.95 - 0.82	1186	1186	100	28	2.6	64.22	0.0583	0.0096
0.82 - 0.74	1196	1196	100	31.06	1.8	68.55	0.0649	0.009
0.74 - 0.68	1295	1295	100	24.8	1.4	63.35	0.0512	0.0098
0.68 - 0.64	1163	1163	100	21.8	1.1	51.8	0.0508	0.0118
0.64 - 0.6	1477	1477	100	20.41	0.9	44.89	0.0628	0.0142
0.6 - 0.57	1396	1396	100	16.3	0.6	34.67	0.0732	0.0191
0.57 - 0.55	1132	1132	100	10.34	0.5	29.87	0.0553	0.0232
0.55 - 0.53	1292	1292	100	9.93	0.4	25.42	0.0634	0.028
0.53 - 0.51	1492	1492	100	9.51	0.3	21.77	0.075	0.0339
0.51 - 0.49	1757	1757	100	8.98	0.2	17.6	0.0924	0.0435
0.49 - 0.47	2063	2063	100	7.63	0.2	14.35	0.1035	0.055
0.47 - 0.46	1196	1196	100	7.04	0.2	12.22	0.1205	0.0676
0.46 - 0.45	1249	1280	97.6	4.97	0.1	9.65	0.1206	0.0894
0.45 - 0.44	1201	1406	85.4	3.03	0.1	7.58	0.12	0.1127
0.44 - 0.42	311	875	35.5	0.91	0.1	6.87	0.1124	0.1256
0.51 - 0.42	8558	9358	91.5	6.27	0.2	13.38	0.0993	0.0607
Inf - 0.42	21644	22447	96.4	14.77	1.7	36.18	0.0427	0.0124

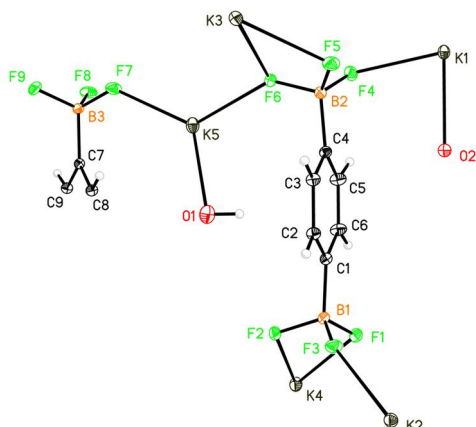


Figure 41: Depiction of the asymmetric unit of **2**. Thermal ellipsoids drawn at 50% probability level. Hydrogen atoms except the one bonded to oxygen atom O1 have been omitted for clarity.

2015/1 (cf. Table 12). Due to the decreasing completeness and redundancy the resolution was cut to 0.45 Å.

4.2 Structure solution and refinement

The analysis of the systematic absences with XPREP 2015/1 gave rise to the space group $I4_1/acd$. The structure was solved using SHELXT.^[71] All further refinement steps were done with SHELXL of the SHELXTL program suite without any resolution cutoffs.^[72] All non-hydrogen atom positions as described by *Falcicchio et al* could be identified by SHELXT and the non-hydrogen atoms were refined using anisotropic displacement factors. The aromatic hydrogen atoms were introduced by using the appropriate HFIX command as implemented in the refinement software. The hydrogen atoms were considered to vibrate isotropically and in correlation with the adjacent non-hydrogen atom. Their displacement factor was therefore set to 1.2 times the U_{eq} of the pivot atom. By difference Fourier analysis the position of the hydrogen atom bonded to the oxygen atom could be identified. The atom was set to

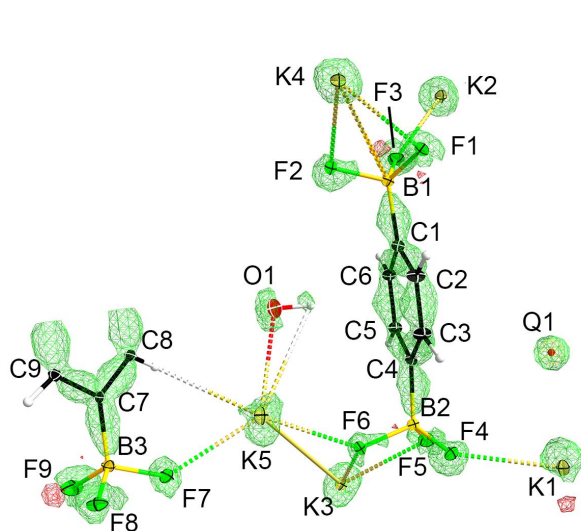


Figure 40: Depiction of the residual density of **2** after initial refinement (Map level $0.2 \text{ e}\text{\AA}^{-3}$). Red icosahedron indicates the highest residual density peak of $1.03 \text{ e}\text{\AA}^{-3}$. Thermal ellipsoids drawn at 50% probability level. Hydrogen atoms have been set to ideal calculated positions except the hydrogen atom bonded to oxygen.

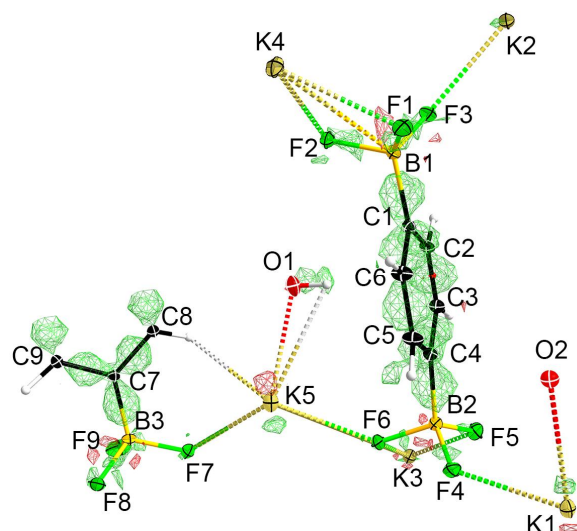


Figure 39: Residual density after adding of the second oxygen atom (Map level $0.15 \text{ e}\text{\AA}^{-3}$). Thermal ellipsoids drawn at 50% probability level. Hydrogen atoms have been set to ideal calculated positions except the hydrogen atom bonded to oxygen.

the position and then moved to the appropriate distance determined by neutron diffraction.^[79] Its isotropic displacement parameter was set to 1.5 times the U_{eq} of the pivot atom. After these refinement steps one relatively high residual density peak remained (cf. Figure 40). The height of the peak is approximately $1 \text{ e}\text{\AA}^{-3}$. The distance of the residual density peak to the adjacent potassium atom ($d = 2.724 \text{ \AA}$) is relatively close to the K-O distance also found in the compound (2.705 \AA). Based on these findings it was concluded that there may be a second, partly occupied water molecule present within the asymmetric unit. After adding refining the model with the second oxygen atom added the site occupation factor indicated an occupancy of 3 %. The second oxygen was not refined with anisotropic displacement factors due to low occupancy. For the same reason no hydrogen atoms were added. Through adding the second oxygen atom the residual density level could considerably be lowered as seen in Figure 39.

4.3 General Discussion of the IAM

In Figure 41 the asymmetric unit of compound **2** is depicted. The main features as determined by *Falcicchio et al* are present. Close contacts between the potassium ions and the fluorine atoms and oxygen atoms can easily be spotted. The refined distances K5 – O1 ($2.704(2) \text{ \AA}$) and K1 – O2 ($2.701(14) \text{ \AA}$) closely agree, which further confirms the plausibility of the presence of the second water molecule. In the packing plot (Figure 42) the layered structure is shown. The trifluoroborates form a layer with the fluorine atoms at the surfaces. The potassium atoms K1, K2, K3 and K4 distribute on this surface and form the connection to the next layer of trifluoroborates. The potassium K5 somehow deviates from this behaviour. It is

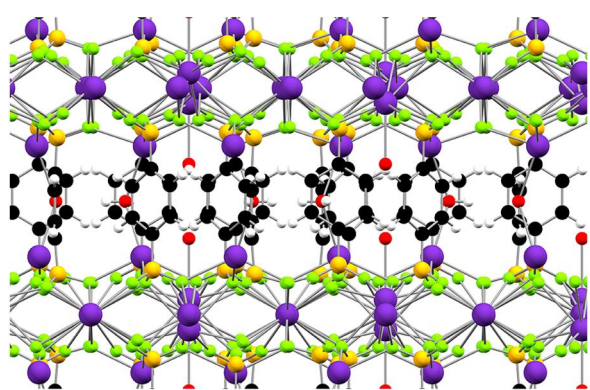


Figure 42: Packing plot of compound 2 along the a axis.

shifted into the layer of organotrifluoroborates and coordinates the oxygen atom O1. The oxygen atom O1 forms two O-H $\cdots\pi$ interactions to the adjacent phenyl moieties of the trifluoroborates (see Figure

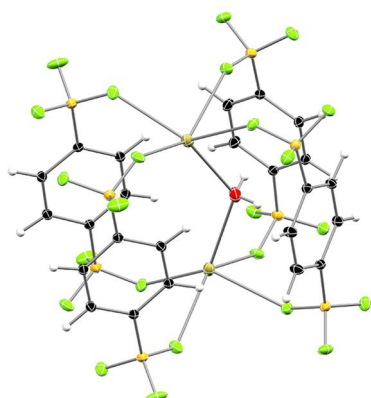


Figure 44: Section of the packing plot of compound 2. The water molecule consisting of oxygen atom O1 shows two O-H \cdots π interactions to two adjacent phenyl rings. Thermal ellipsoids drawn at 50% probability level.

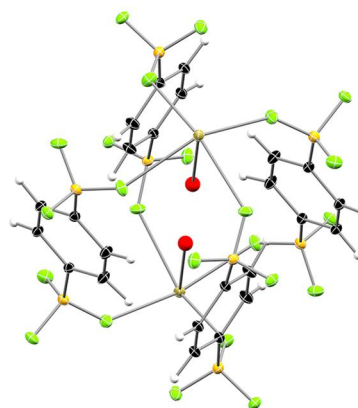


Figure 43: Section of the packing plot around oxygen atom O2. It is surrounded by four phenyl rings. Thermal ellipsoids drawn at 50% probability level.

44). These interactions certainly stabilise the trifluoroborate layer. The second oxygen atom O2 is surrounded by four phenyl rings (cf. Figure 43). The distances from the oxygen atom to the phenyl ring centres (3.934 Å and 3.755 Å) are slightly higher than for the oxygen atom O1 (3.209 Å). It is however likely that this additional water molecule also takes part in O-H \cdots π interactions. With these new findings and the results already reported by *Falcicchio et al* an inspection of compound 2 within the QTAIM framework based on the experimental data seems promising.

4.4 Multipole model refinement

The IAM as described in the previous chapter was used as starting point for the multipole model refinement. The hydrogen atom positions were again determined by difference Fourier analysis using only high order data and subsequently moved to tabulated neutron distances.^[79]

The modified IAM was then used to generate the initial model for the multipole model refinement with the XD2006 program suite by using the XDINI program.

The initial files generated by the XDINI program need to be modified. The local coordinates as well as the highest order of multipoles used and thermal parameters were adjusted to fit the needs of the compound at hand (cf. Table 13). For all carbon atoms the local coordinate systems were set in a manner that $2m$ symmetry for the multipoles can be adopted. For all boron atoms the coordinate systems were adjusted to allow $3m$ symmetry to be assumed. The fluorine atoms do not need to satisfy any specific symmetry. The oxygen atom O1 which lies on a crystallographic mirror plane was modified to adopt this mirror symmetry. The potassium atoms were assumed to be cationic. The spherical valence density of the potassium atoms was distributed over the fluorine atoms. Due to the low occupancy of oxygen atom O2 also no valence density was refined. The initial value of the spherical valence density has been kept fixed during the whole refinement. The highest order of multipoles was set to hexadecapoles for all carbon, boron and fluorine atoms. For the hydrogen atoms the monopole and a bond directed dipole were refined. For the individual atom types individual expansion–contraction parameters (κ and κ') were used. The expansion–contraction for hydrogen were fixed to values proposed by Volkov et al ($\kappa = 1.1$; $\kappa' = 1.18$).^[80] The refinement

Table 13: Definition of the local coordinate systems (columns one to five) for the non-hydrogen atoms of compound 1. Maximum level of thermal parameters (TP), maximum level of multipoles (LMX), local symmetry (Site Symm) and chemical constraints (Chem Con)

Atom	Atom 1	Ax1	Atom 2	Ax2	R/L	TP	LMX	Site Symm	Chem Con
K(1)	F(4)	Z	O(2)	Y	R	3	0		
K(2)	F(3)	Z	B(1)	Y	R	3	0		
K(3)	F(5)	Z	F(6)	Y	R	3	0		
K(4)	F(2)	Z	F(1)	Y	R	3	0		
K(5)	F(6)	Z	F(7)	Y	R	3	0		
F(1)	B(1)	Z	F(2)	Y	R	2	0		
F(2)	B(1)	Z	F(3)	Y	R	2	4	No	F(1)
F(3)	B(1)	Z	F(1)	Y	R	2	4	No	F(1)
F(4)	B(2)	Z	F(5)	Y	R	2	4	No	F(1)
F(5)	B(2)	Z	F(6)	Y	R	2	4	No	F(1)
F(6)	B(2)	Z	F(4)	Y	R	2	4	No	F(1)
F(7)	B(3)	Z	F(8)	Y	R	3	4	No	F(1)
F(8)	B(3)	Z	F(9)	Y	R	3	4	No	F(1)
F(9)	B(3)	Z	F(7)	Y	R	3	4	No	F(1)
O(1)	DUM1	Z	H(1)	Y	R	2	4	m	
O(2)	H(5)	Z	K(1)	Y	R	2	1		
C(1)	B(1)	Z	C(2)	Y	R	2	4	2m	
C(2)	C(1)	Z	C(6)	Y	L	2	4	2m	
C(3)	C(4)	Z	C(5)	Y	R	2	4	2m	C(2)
C(4)	B(2)	Z	C(3)	Y	L	2	4	2m	C(1)
C(5)	C(4)	Z	C(3)	Y	L	2	4	2m	C(2)
C(6)	C(1)	Z	C(2)	Y	R	2	4	2m	C(2)
C(7)	B(3)	Z	C(8)	Y	L	2	4	2m	C(1)
C(8)	C(7)	Z	C(9)	Y	R	2	4	2m	C(2)
C(9)	C(7)	Z	C(8)	Y	L	2	4	2m	C(2)
B(1)	C(1)	Z	F(2)	Y	R	2	4	3m	
B(2)	C(4)	Z	F(6)	Y	L	2	4	3m	B(1)
B(3)	C(7)	Z	F(9)	Y	R	2	4	3m	B(1)

Table 14: Detailed description of the refinement strategy (Abbreviations: Sca, scale factor (refined in every step, only mentioned in the first one); CC, chemical constraints; LS, local symmetry; SIGOBS, data with I/σ smaller than the number is excluded from the refinement; M, monopoles; D, dipoles; Q, quadrupoles; O, octapoles; H, hexadecapoles; $\kappa\kappa'$, expansion-contractions parameters; (H)XYZ, positional parameters; U2, displacement parameters; U3, third order Gram-Charlier coefficients).

#	Parameter Groups	SIGOBS	CC	LS
1	Scale	3	1	1
2	M	3	1	1
3	MDQOH	3	1	1
4	U2 MDQOH	3	1	1
5	XYZ U2 MDQOH	3	1	1
6	HXYZ	3	1	1
7	XYZ U2 MDQOH	3	1	1
8	κ	3	1	1
9	XYZ U2 MDQOH κ	3	1	1
10	κ'	3	1	1
11	XYZ U2 MDQOH κ	3	1	1
12	XYZ U3 U2 MDQOH κ	0	1	1
13	XYZ U3 U2 MDQOH κ	0	1	0
14	XYZ U3 U2 MDQOH κ	0	0	0

strategy was chosen according to the block refinement approach and tested for overfitting with the help of k-fold cross validation.^[24,26,30,88]

In the first refinement step only the scale factor is refined. Then the mono- and multipole parameters are introduced (steps 1 and 2). Next the thermal displacement parameters and the coordinates of the hydrogen as well as the non – hydrogen

atoms are refined. Thereafter, the expansion – contraction parameters κ and κ' are added. Due to shashlik like residual density patterns around the potassium atoms K1, K2, K3 and K5 and the fluorine atoms F7, F8 and F9 third order Gram - Charlier parameters were added in the next step.^[124] Furthermore, the σ cut off was removed. In the last two refinement steps the local symmetry and the chemical constraints were removed from the refinement.

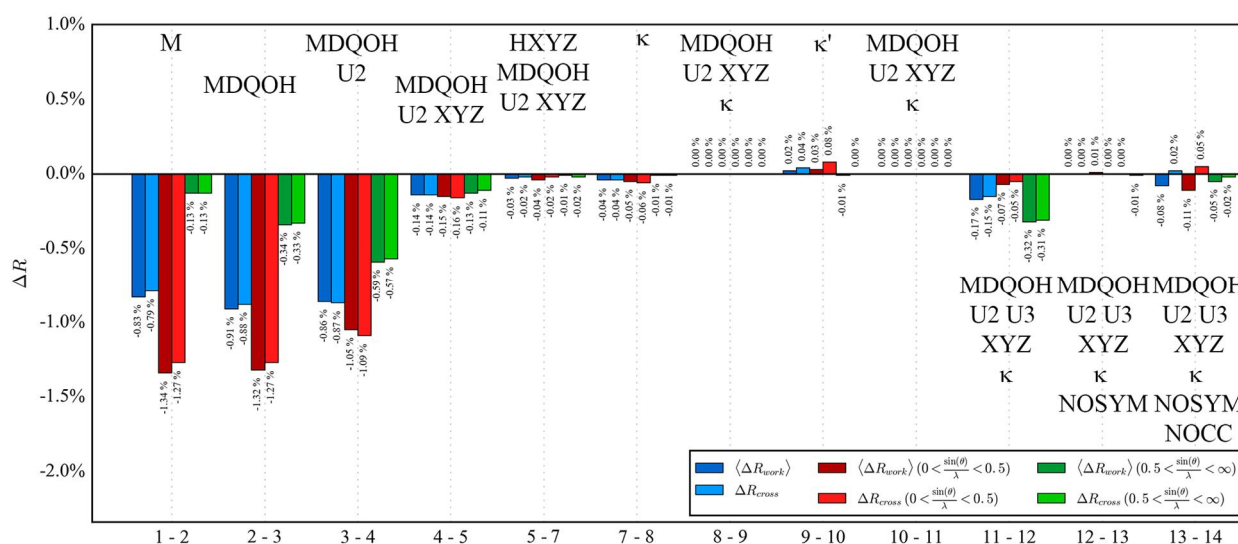


Figure 45: Course of the R_{free} over the whole refinement strategy.

The results of the k-fold cross validation suggest that the last refinement step, which is the removal of the chemical constraints would overfit the data (Figure 45). Furthermore, step 13, the removal of the local symmetry at the carbon and boron atoms, does not improve the model. Therefore, the final refinement strategy consists of steps 1 to 12 from Table 14.

4.5 Validity of the model

The quality of the model has been carefully investigated. The first indicator of the quality of the model are the residuals of the least squares fit based on the squared

structure factors. For the present refinement this equals to 2.00 % which is an adequate value.

Since only investigating the residuals of the least squares may be misleading also the residuals of the difference density must be closely investigated. The visual inspection of the residual density reveals that a slightly bigger amount of residual density is located around the potassium

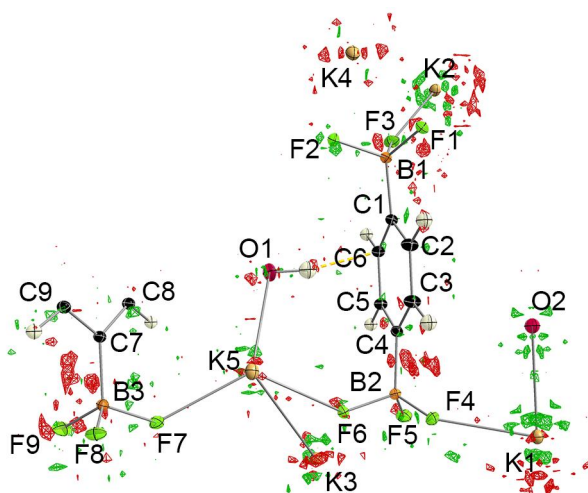


Figure 46: Residual density depicted at a level of $0.12 \text{ e}\text{\AA}^{-3}$ without any resolution cut off. Graphics rendered with MoleCoolQt.^[1] Thermal ellipsoids drawn at 50% probability level.

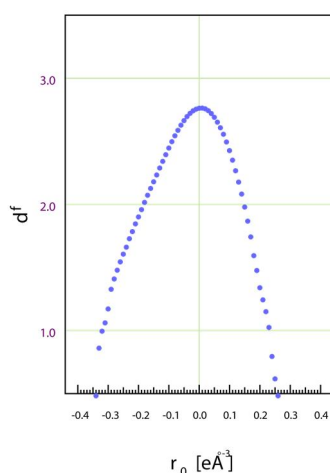


Figure 47: Plot of the fractal dimension of the residual density. $D_f(\text{max}) = 2.7630$.

atoms. The rest of the structure shows a low level of residual density. The highest residual density peak is $0.261 \text{ e}\text{\AA}^{-3}$, the deepest hole $-0.345 \text{ e}\text{\AA}^{-3}$. During the refinement strategy, testing it was investigated if refining mono- as well as multipoles for the potassium ions copes with this residual density. However, the monopoles tend to take unphysical values and refining the multipoles did not improve the residual difference density maps.

The analysis of the fractal dimension of the residual

density confirms the conclusions from the visual inspection of the residual density.^[31] The maximum value of $D_r(\max) = 2.7630$ suggests that the residual density is almost featureless. Although the residual density is not as flat as for other compounds it is still satisfactory for a sample containing fourth row elements.

The course of the ratio between the observed and calculated structure factors reveals larger deviations from unity in the low and high angle regions as was already shown in chapter 3.5.

However, the deviations are

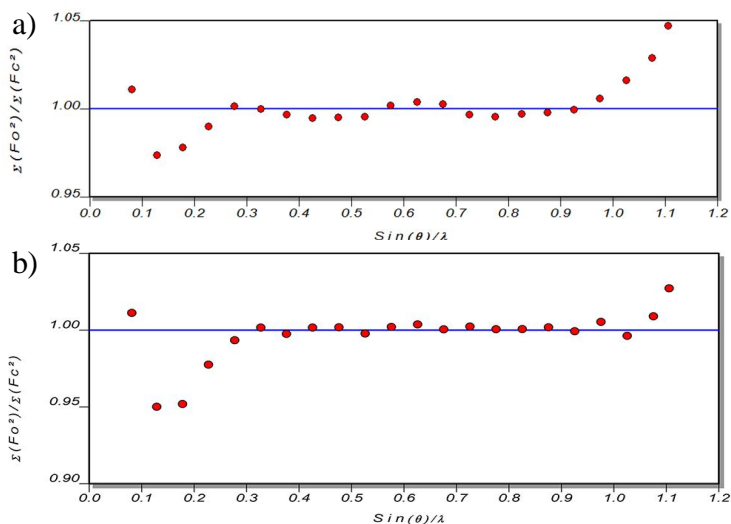


Figure 48: Resolution dependence of the ratio between mean observed and calculated structure factors a) before and b) after the use of resolution dependent scaling.

smaller than five percent over the whole resolution range which is generally accepted and still suggests a good model. As for compound **1** in Chapter 3 a refinement as suggested by *Niepötter et al* has been tried but no improvement in the course of the ratio of the calculated and observed structure factors was noticeable.^[32] Therefore, ten resolution dependent scaling factors were introduced which improved the course of the plot.

All investigated model quality indicators show that the quality of the model is sufficient for further analysis within the QTAIM framework. Table 15 summarises the crystallographic data after the final multipole model refinement.

Table 15: Crystallographic data for compound 2.

Empirical formula	C H B F K O	Absorption coefficient	1.595 mm ⁻¹
Formula weight	87.18	F(000)	7315
Temperature	101(2) K	Crystal size	0.200 x 0.200 x 0.200 mm
Wavelength	0.71073 Å	Theta range for data collection	1.938 to 57.161°
Crystal system	Tetragonal	Reflections collected	16781
Space group	I4 ₁ /acd	Completeness to theta = 25.242°	99.10%
Unit cell dimensions	a = 17.4440(5) Å	Absorption correction	Semi-empirical from equivalents
	b = 17.4440(5) Å	Max. and min. transmission	0.7503 and 0.6757
	c = 40.1485(13) Å	Refinement method	Full-matrix least-squares on F2
	α=β=γ= 90°	Data / parameters	16781 / 371
Volume	12216.9(8) Å ³	Goodness-of-fit on F2	1.8477
Z	170	R indices (all data)	R ₂ = 0.0200, wR ₂ = 0.0242
Density (calculated)	2.014 Mg/m ³	Largest diff. peak and hole	0.261 and -0.345 eÅ ⁻³

4.6 Topological Analysis of dipotassium phenylene-1,4-bis(trifluoroborate)

The search for critical points in the electron density ρ and the associated bond paths has been carried out. The search resulted in the molecular graph for the asymmetric unit shown in Figure 49. This initial search has been carried out without

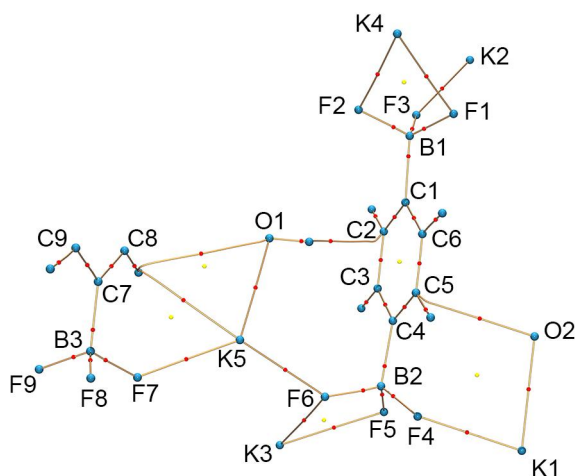


Figure 49: Molecular graph of the asymmetric unit of compound 2. Red sphere: BCP; yellow sphere: RCP; blue sphere: atom position.

atoms by bond paths (Figure 50). The potassium atom K5 which is shifted into the trifluoroborate layer shows the smallest number of interactions associated with a bond path. It shows four bond paths to fluorine atoms, one to the adjacent oxygen atom O1 and one to a hydrogen of a trifluoroborate. The mean value of ρ at the bond critical points for the four bond paths to the fluorine atoms equals to

taking the symmetry equivalent fluorine into account. In this compound the interactions involving the potassium atoms are of special interest. Therefore, the environment of each potassium was searched for BCPs taking the symmetry of the crystal into account (Table 16). It can be seen that each potassium atom is linked to numerous fluorine

0.105 eÅ⁻³ (range 0.104 - 0.110 eÅ⁻³). The BCP linking O1 and K5 shows an electron density of 0.111 eÅ⁻³. The value of the electron density at the BCP for the H8 – K5 interaction is 0.034 eÅ⁻³. The interactions involving the fluorine and the oxygen atoms are close in their values of ρ at the BCP. This suggest that the interaction with the hydrogen atom is significantly weaker.

The interactions for potassium atom K1 with the neighbouring fluorine atoms show a wider distribution than at potassium atom K5. The smallest value of ρ at the BCP is 0.046 eÅ⁻³ and maximum value is 0.115 eÅ⁻³. The value for the bond path linking K1 and O2 shows a value of 0.071 eÅ⁻³. However due to the low occupancy of O2 an interpretation of the value for this bond path seems not to be sensible.

The potassium atoms K2, K3 and K4 only show interactions with fluorine atoms. The electron density at the BCP ranges from 0.029 eÅ⁻³ for bond path K2 F9 to 0.100 eÅ⁻³ for bond path K2 F3.

Considering all bond paths linking potassium and fluorine atoms, from Table 16 it can also be seen that the length of the bond

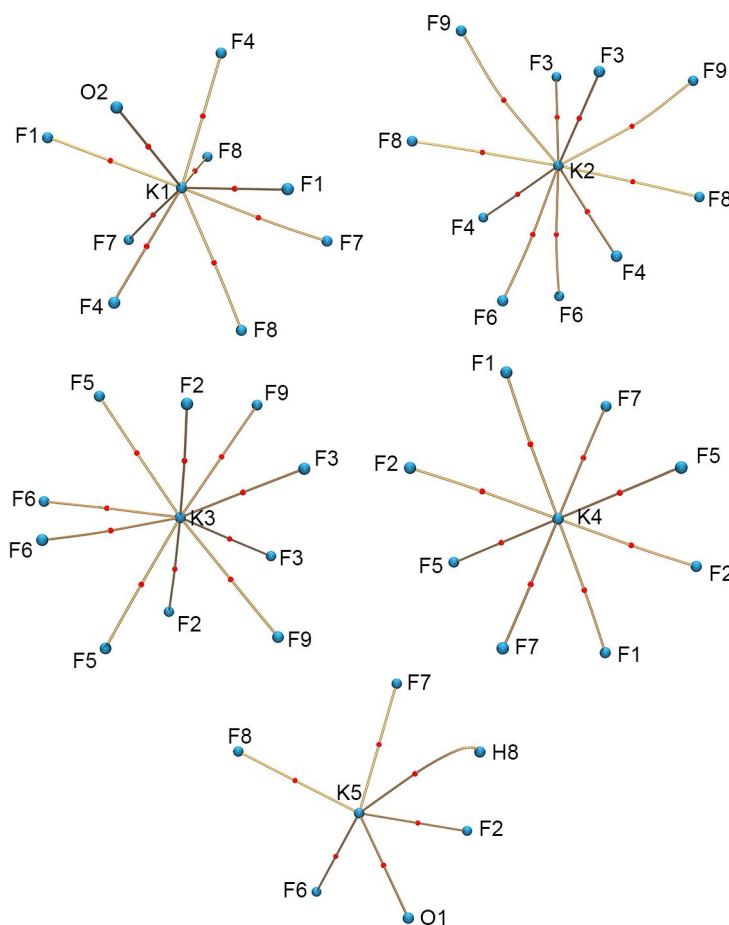


Figure 50: Molecular graph of the environment of the five potassium atoms. Blue spheres: atom positions; red spheres: BCPs.

path correlates with the electron density at the BCP. The highest electron density of 0.115 eÅ⁻³ at the BCP is found for the bond Path K1 F4 (2.6014 Å). The same is

also true for the Laplacian of the electron density. The shorter the bond path, the higher the values for ρ and $\nabla^2\rho$ (cf. Table 16). Also the slightly positive values of the Laplacian indicate that the potassium and fluorine atoms form closed-shell interactions.

However, to judge the interaction type solely

Table 16: Values of ρ , $\nabla^2\rho$ and the length of the bond path for unique interactions involving potassium atoms.

Atom A	Atom B	$\rho / \text{e}\text{\AA}^{-3}$	$\nabla^2\rho / \text{e}\text{\AA}^{-5}$	$d / \text{\AA}$
K1	F4	0.115(0)	2.442(0)	2.6014
K1	X24_F1	0.098(0)	2.079(0)	2.6601
K1	O2	0.071(0)	1.394(0)	2.7266
K1	X6_F8	0.056(0)	1.202(0)	2.8822
K1	X6_F7	0.046(0)	0.981(0)	2.9591
K2	F3	0.100(0)	2.126(0)	2.6516
K2	X11_F4	0.095(0)	2.038(0)	2.6742
K2	X24_F8	0.068(0)	1.433(0)	2.8075
K2	X11_F6	0.050(0)	1.058(0)	2.9416
K2	X24_F9	0.029(0)	0.646(0)	3.1543
K3	F5	0.082(0)	1.741(0)	2.7358
K3	X21_F3	0.073(0)	1.606(0)	2.7568
K3	X18_F9	0.063(0)	1.390(0)	2.8054
K3	F6	0.066(0)	1.406(0)	2.8231
K3	X21_F2	0.057(0)	1.263(0)	2.8474
K4	F2	0.083(0)	1.759(0)	2.7336
K4	X31_F7	0.076(0)	1.612(0)	2.7632
K4	F1	0.076(0)	1.615(0)	2.7665
K4	X24_F5	0.061(0)	1.309(0)	2.8335
K5	F6	0.110(0)	2.356(0)	2.6143
K5	F7	0.107(0)	2.272(0)	2.6293
K5	X31_F2	0.104(0)	2.224(0)	2.6347
K5	X19_F8	0.100(0)	2.122(0)	2.6544
K5	O1	0.111(0)	2.173(1)	2.7061
K5	H8	0.034(0)	0.566(0)	2.9416

on the value of the Laplacian at the bond critical point might be misleading.^[38] To confirm the closed-shell interactions type of the fluorine potassium interactions plots of the Laplacian along the bond path were considered.

In Figure 51 plots of the Laplacian along the bond path are drawn. Three bond paths have been chosen. The bond paths K1 F4 and K2 X32_F9 are the ones with the minimum and maximum value of ρ at the bond critical point. The bond path K4 F1 was chosen because it shows an intermediate value between these two extremes. The course of the Laplacian along the bond path shows two charge depletion regions along with a large charge concentration close to the fluorine atom position

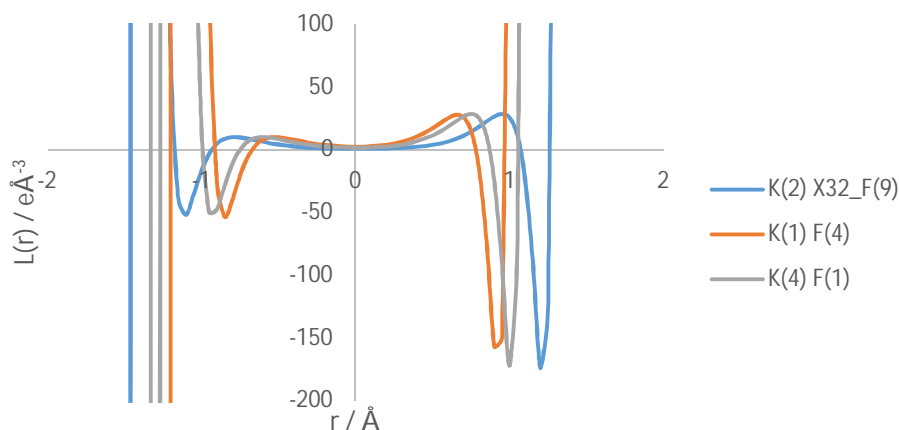


Figure 51: Plot of the Laplacian along the bond path. The BCP is put to the origin. Negative values along the abscissa point towards the potassium atom, positive values towards the fluorine atom.

(around 1 Å depending on the bond path length). It is also clear that the depth of the local minima of the Laplacian is only varying slightly.

When compared to the statement by *Falccichio et al* about the short contacts present in the compound it is apparent that almost all potassium atoms show less BCPs associated with bond paths than the proposed number. The potassium atoms K2, K3 and K4 show according to *Falccichio et al* 10 short contacts to fluorine atoms. However only K2 and K3 do show ten bond paths to the adjacent fluorine atoms. K4 does only show eight bond paths. Potassium atom K5 does show all the four proposed bond paths linking potassium and fluorine and the one linking it with O1, however it lacks the proposed bond paths to the carbon atoms. Instead, a bond path linking K5 and hydrogen atom H8 is detectable. Potassium atom K1 shows the proposed eight bond paths to fluorine plus one to the partly occupied oxygen atom.

The existence of a bond path as a criterion to decide whether a bonding interaction is present or not is subject to discussion. *Bader* stated that the existence of a BCP is a sufficient and necessary condition for a bonding interaction within the QTAIM.^[38,91,125–127] The subject of the discussion is whether a bond path is equivalent to a chemical bond. In early studies it has been noticed that not only *chemical bonds* are accompanied by BCPs but also secondary interactions.^[128–130] *Haaland et al* showed from their theoretical study on the inclusion complex of helium in adamantane that the interactions between the carbon atoms and the helium atom are in fact antibonding.^[131] They concluded that these interaction lines could not be classified as *chemical bonds* due to their antibonding nature. Within the QTAIM, atoms are bonded if they share an atomic surface and are thus linked by a bond bath with its accompanying BCP. However, the presence or absence of a bond path is influenced by many contributions.^[90,128] Certainly the geometry of the molecule has an impact on the electron density distribution. It is possible that especially in experimental charge density the geometry of the molecule does deviate from the theoretically calculated one due to the crystal environment.^[118,132] One of the situations where bond paths are missing are so called catastrophe points. At such a point for example a bond critical point and a ring critical point coincide and therefore vanish.^[35] Another way to identify and classify weak interactions is the

NCI descriptor (see Chapter 2.4). With its help it is possible to reveal interactions not manifested in the form of a bond path or a bond critical point. Plots of the RDG versus the electron density reveal non-covalent interactions in the low density, low RDG region.^[45] In Figure 52 these plots are shown for all potassium ions in 2. As pointed out in Chapter 2.4 noncovalent interactions are accompanied with low values of the RDG in regions of low electron density. All of the plots in Figure 52 spikes within the RDG can be found in the region from 0.0 to 0.2 $e\text{\AA}^{-3}$. This does correspond well to the values of ρ at the found bond critical points from Table 16. It is however difficult to conclude on the number of interactions linked with the potassium atoms from these plots alone. Therefore, three-dimensional isosurfaces of the RDG were calculated. As proposed by *Johnson et al* the property $\rho \cdot \text{sign}(\lambda_2)$ was mapped onto the isosurfaces. The outcome of this is particularly interesting for potassium atom K4 which shows less bond paths and BCPs to fluorine atoms as proposed by *Falccichio et al*. In addition, the nature of the interactions may be identified.

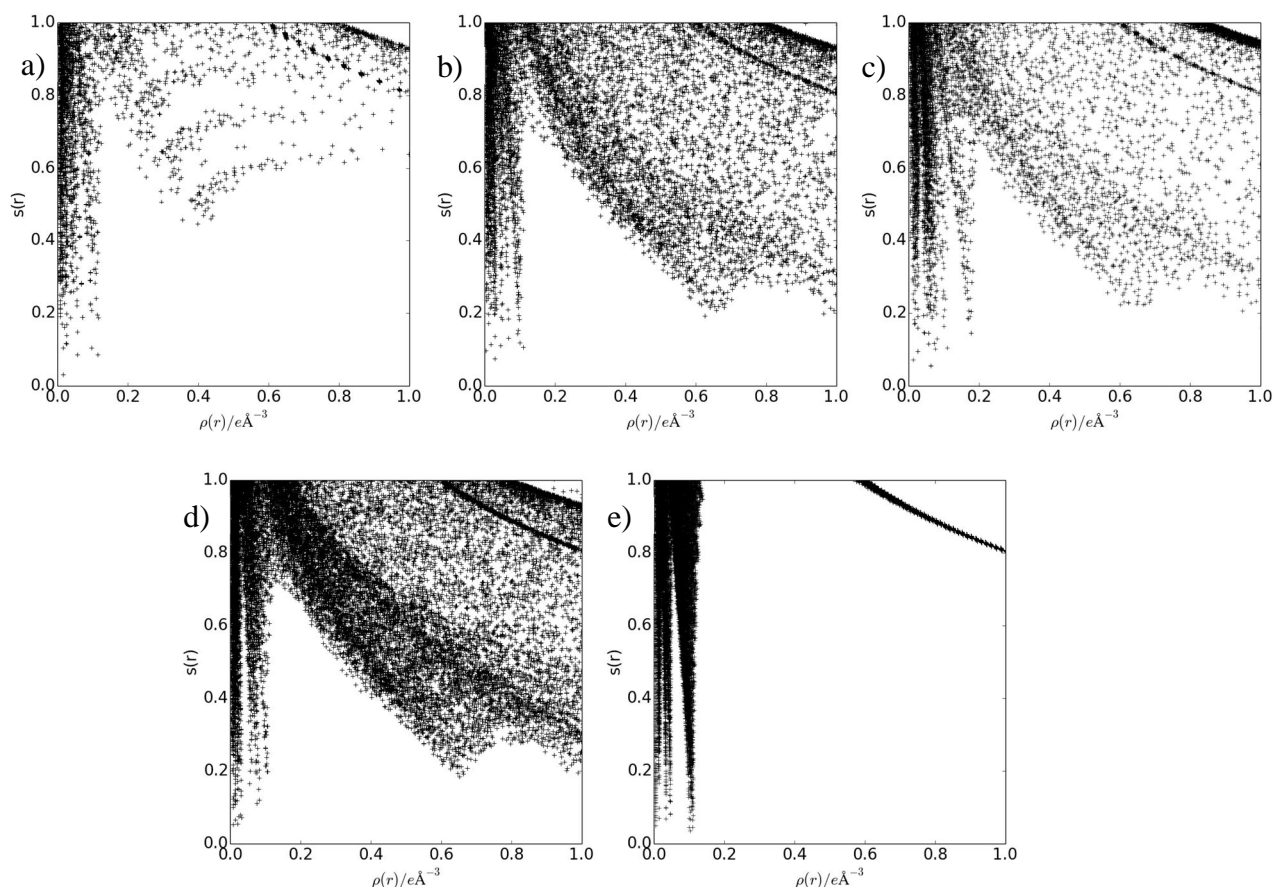


Figure 52: Plots of the reduced density gradient $s(r)$ vs. the electron density $\rho(r)$ for the region around the potassium atoms K1 to K5 (a-e). The spikes in the low electron density and low RDG region indicate non-covalent interactions.

In Figure 53 the isosurface representation of the RDG around K4 is drawn at a

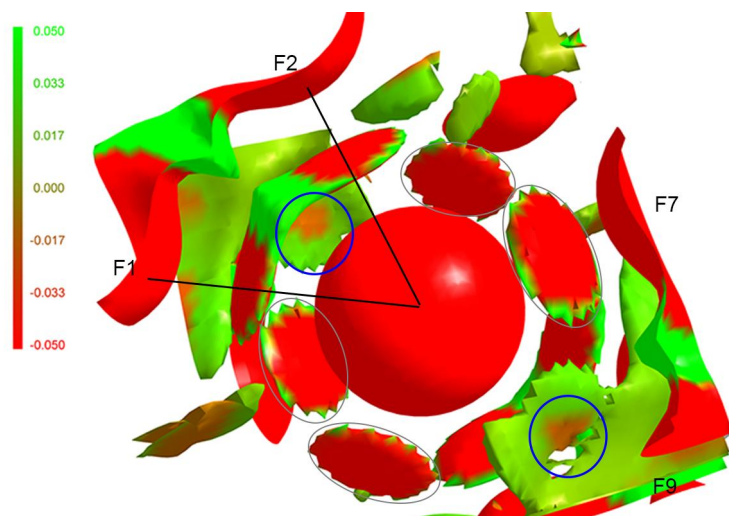


Figure 53: $\rho \text{sign}(r)$ mapped onto the reduced density gradient $s(r)$ around K4 at a level of 0.9. Red shows attractive, green repulsive interactions. Interactions to fluorine F5 and F7 marked in grey, to fluorine F9 marked in blue.

level of 0.9 with the property $\rho \text{sign}(\lambda_2)$ mapped onto it. The interactions are clearly visible. The interactions to F1, F2, F7 and F5 and their symmetry equivalents are represented by disc shaped volumes indicated by grey circles in Figure 53. The values of $\rho \text{sign}(\lambda_2)$ indicate that these are attractive interactions. The outer edges of the discs show additional features of repulsive interactions. It may also be seen that there are weak attractive interactions to fluorine atom F9 (indicated by blue circles) and its symmetry equivalent. However, these interactions are considerably weaker than the others which explains the lack of a BCP and the corresponding bond path.

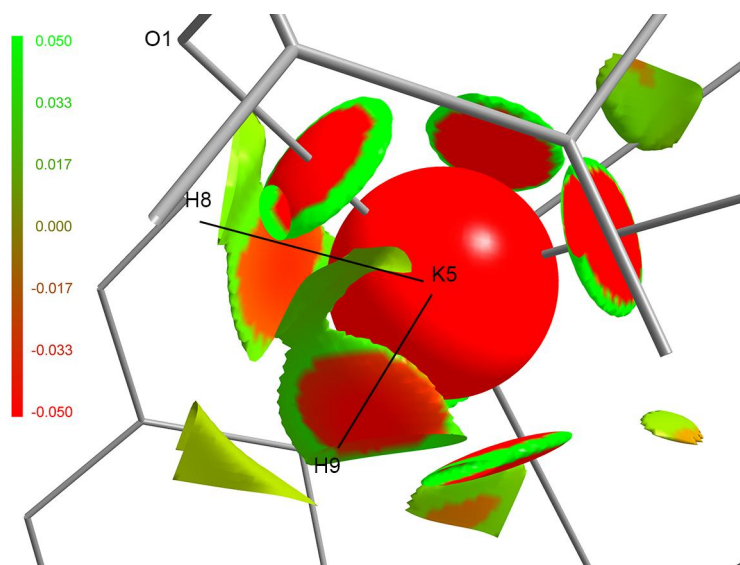


Figure 54: $\rho \text{sign}(r)$ mapped onto the reduced density gradient $s(r)$ around K5 at a level of 0.9. Red shows attractive, green repulsive interactions.

For both potassium ions K4 and K5 all interactions are showing areas where repulsive interactions are visible. It needs to be mentioned that this should not be

Falccichio et al proposed two close contacts to the carbon atoms C8 and C9 adjacent to potassium atom K5. However, only one BCP was found between H8 and K5. The NCI analysis reveals two attractive interactions to H8 and H9 (cf. Figure

over interpreted because the regions of noncovalent interactions are governed by low electron density. Therefore, the sign of the Hessian eigenvalues may change rapidly.

4.7 Conclusion

In conclusion, by having been able to record a high resolution data set it could be shown that there is an additional water molecule present within the asymmetric unit of compound **2**. This solvent molecule however exhibited a very low occupancy. Despite the fact that the XD2006 program suite^[29] is limited in its capabilities of handling partial occupation of atoms the multipole model refinement has been carried out successfully. The topological analysis showed that the theoretically proposed non-covalent interactions could also be found experimentally. It could be shown that the presence of a bond path for non-covalent interactions is not always given. The bond critical points of the bond paths associated with non-covalent interactions are usually located in regions of very shallow electron density and may thus be absent. By using the reduced density gradient as an indicator, interactions without an associated bond path could be visualized.

5 Influence of the Estimated Standard Deviation on Charge Density Refinements

Charge density investigations require not only high resolution data sets but these need to also be of exceptional high quality for meaningful interpretation of the calculated model.^[133] One import factor in estimating the quality of the data is the standard uncertainty of the measurements. Recently *Henn et al* and *Jørgensen et al* reported on the significance of Bragg reflections.^[134–136] In their article *Henn et al* argue that the significance of the raw data limits the significance of the processed Bragg data.

$$\frac{I_{raw}}{\sigma_{raw}} \geq \frac{I_{Bragg}}{\sigma_{bragg}} \quad (15)$$

In eq. (15) I_{raw} and σ_{raw} denote the unprocessed intensity and standard uncertainty while I_{Bragg} and σ_{Bragg} stand for the processed ones. They introduce the descriptor W which is defined as the mean intensity divided by the mean standard uncertainty for a given number of data (cf. (16)). Within the Poisson limit the standard uncertainty is $\langle I^{1/2} \rangle$. By processing the data only $\langle \sigma(I) \rangle$ should increase which leads to the conclusion that W for real processed data should always attain values smaller than 1.

$$W = \frac{\langle I^{1/2} \rangle}{\langle \sigma(I) \rangle} < 1 \quad (16)$$
$$W_2 = \frac{\langle I \rangle}{\langle \sigma^2(I) \rangle} < 1$$

However, the averaging may lead to false conclusions due to bias introduced by standard uncertainties exhibiting extreme values. *Henn et al* therefore examine plots of the significance $\frac{I}{\sigma(I)}$ of the raw versus the processed data. They compare the two commonly used programs SADABS^[16] and SORTAV. In Figure 55 one of the plots by Henn et al is shown. The

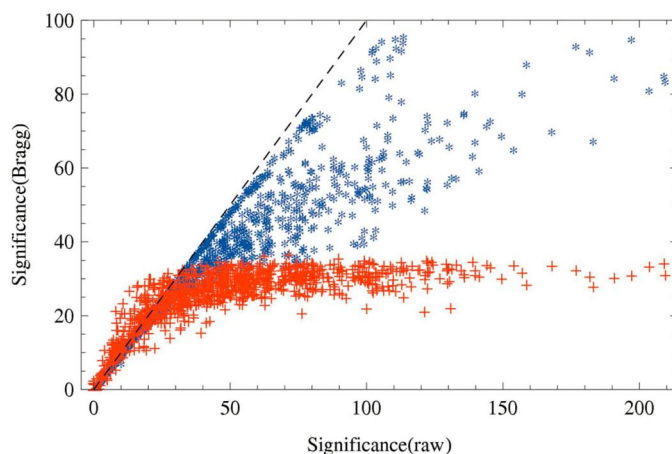


Figure 55: Plot of the raw versus Bragg significance as shown by Henn et al.^[1] Blue stars refer to data processed with SORTAV, red crosses to data processed with SADABS, black line represents Poisson limit.

black dashed line therein represents the Poisson limit of $W = 1$. It can be seen that for the data processed with SADABS (red) the Bragg significances do not exceed a certain value whereas for the data processed by SORTAV (blue) the Bragg significance increases with increasing raw significance. Furthermore for the data processed with SADABS it can be seen that for low raw significances the inequation (15) is not fulfilled. In consequence, this means that after processing the data former less significant reflections suddenly become more significant and a majority of the reflections end up with almost equal significances. This behaviour is a consequence of the error model applied within SADABS. Using an error model is a generally used and accepted method for routine crystallography.^[22,137–141] Within SADABS an empirical model is used to scale the standard uncertainties.

$$\sigma^2(I)_{corrected} = [K\sigma(I)_{raw}]^2 + [g\langle I \rangle]^2 \quad (17)$$

Herein the corrected standard uncertainty $\sigma^2(I)_{corrected}$ is calculated from square of the raw standard uncertainty $\sigma(I)_{raw}$ and the raw intensity I by introducing two parameters K and g . These parameters are refined so that the weighted mean square deviation χ^2 is close to unity.^[16] As *Krause et al* state, this is a standard statistical procedure and not only used in SADABS but also in other programs (XDS^[142], AIMLESS^[143], HKL-2000^[144]) used for data processing. Within recent versions of SADABS the possibility to choose different combinations of

refining values for g and K and keeping them fixed is implemented. This enables the user to choose the error model to their convenience.

An interesting point in this discussion is that neither *Henn et al* nor *Jørgensen et al* examine the influence of the error model on the refined model. *Jørgensen et al* at least mention that in their experience the influence on the refined model seems to be not significant but do not show results. In their response to *Jørgensen et al*, *Henn et al* speculate that despite the small influence on the refined model the influence on the topology of the derived density and Laplacian distribution might be significantly affected.

A detailed investigation on this matter has not yet been published. The newly introduced possibility to choose the error model in SADABS however simplifies an investigation. By using the same program with different error models on the same raw data other influences as for example outlier rejection do not influence the study. To contribute to this interesting discussion the influence of the error model on the refined model as well as on the derived properties for the two data sets discussed in the previous two chapters has been undertaken.

5.1 Descripton

As already mentioned in recent SADABS versions a multitude of different combination of fixed and refined values can be chosen. In Table 17 all possible combinations are given. For the present study the first six were chosen to be examined. In principle option 0 translates to using the raw standard uncertainties. The next two options add the intensity dependent term by refining either an overall g value or one g value for each run. Options 3 and 4 refine an overall scale factor K for the raw standard uncertainties whereas options 5 and 6 refine one scale factor K for each run. The options 7 to 11 include the possibility to keep one or both parameters fixed.

Table 17: Overview of all combinations for the parameters K and g in (17). Refined(overall) indicates one parameter is used for all runs; refined(all) means one parameter is refined for each run.

#	K	g
0	1	0
1	1	refined(overall)
2	1	refined(all)
3	refined(overall)	refined(overall)
4	refined(overall)	refined(all)
5	refined(all)	refined(overall)
6	refined(all)	refined(all)
7	refined(overall)	fixed input
8	refined(all)	fixed input
9	fixed input	refined(overall)
10	fixed input	refined(all)
11	fixed input	fixed input

The individual refinement strategies developed for compounds **1** and **2** have been applied to data processed using options 0 to 6. All other data processing steps have been kept identical. Within this study the influence on the refined model as well as on the thereof determined properties will be examined.

5.2 Examination of the raw and processed data

At first plots of the significance of the raw versus the processed data were made.

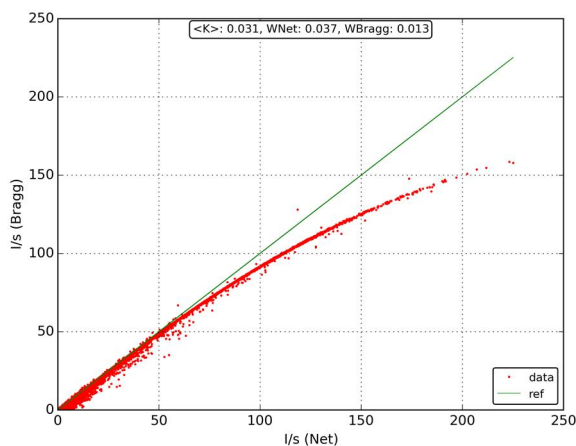


Figure 56: Plot of the significance of the processed vs the raw data for compound **1** with error model option 1 used.

From Figure 56 it may be seen that the influence of one refinable g is higher for higher significances. The curve starts to take a sigmoidal shape (Figure 56). The significance of the processed data in this region is lowered compared to the raw

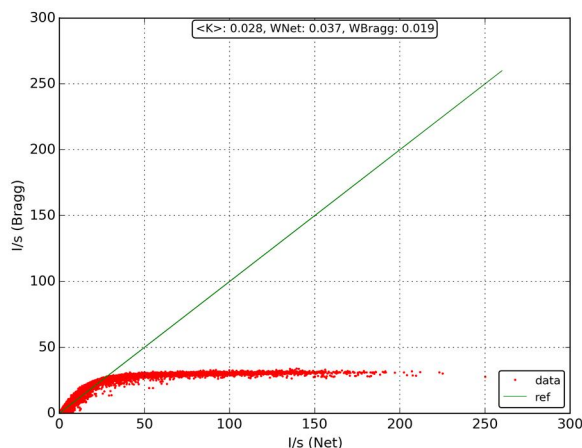


Figure 57: Plot of the significance of the processed vs the raw data for compound **1** with error model option 3 (left).

data. The same is also visible when one parameter g is refined for each run of the experiment. The plot then branches out for high significances. Each of these branches is associated with one value of g . In this low order range reflections are typically strong and thus more significant. However, the low order reflections are also influenced by systematic errors

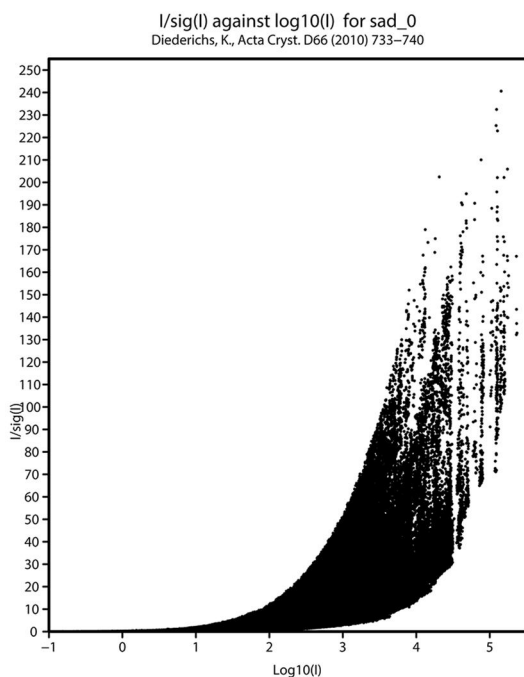


Figure 59: Plot of $I/\sigma(I)$ vs $\log(I)$ for error model option 0.

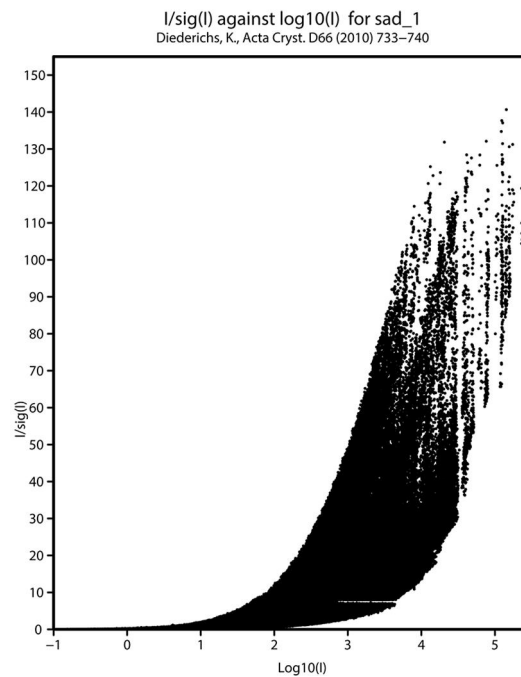


Figure 58: Plot of $I/\sigma(I)$ vs $\log(I)$ for error model option 1.

like overexposures or being close to the beam stop which would justify a lowering of their significance.

The introduction of the parameter K does lead to the typical overestimation of the low significance reflections after processing the data as observed by *Jørgensen*

et al and *Henn et al* (Figure 57).

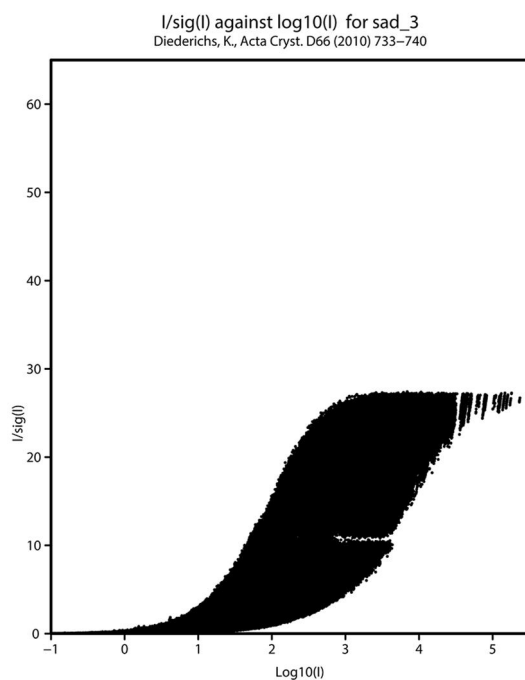


Figure 60: Plot of $I/\sigma(I)$ vs $\log(I)$ for error model option 3.

The Influence of the used error model can also be studied from plots of the logarithm of the intensity versus the significance for compound 2 as introduced by *Diedrichs*.^[22] Figure 59 shows the plot for using error model option 0. In general from this plot it is evident that stronger reflections are usually more significant. It may be seen that the highest significance is in the range of 240. By introducing the refinable parameter g the highest

significance drops to 140 (Figure 58). Through the addition of the parameter K the range of significances is lowered down further. In consequence most reflections will exhibit an almost equal significance (Figure 60).

5.3 Differences in the model for compound 1

To judge on the influence on the model for all error model options the refinement with the in Chapter 3 determined strategy have been carried out. No weighting scheme was applied. To get a first impression the residuals of the least squares refinement are reviewed (Table 18). The lowest R-value is achieved by using the error model option 0. A general trend visible from Table 18 is that the options which use a g parameter per experimental run seem to exhibit a higher R-value than the error model options utilizing one overall parameter g . The R-values of the error model options 1, 3 and 5 differ from their corresponding options 2, 4, and 6 by about 0.05%. Furthermore, it can be seen that the introduction of the refinable parameter K introduces an increase in R-value (error model option 0 $R(F^2) = 2.43\%$; error model option 3 $R(F^2) = 2.63\%$). However, it needs to be noted that the R-value is influenced by a lot of factors such as the number of reflections and the data to parameter ratio. While the number of parameters is the same for all of the compared models the number of reflections is not. Therefore, also the data to parameter ratio has been compared (Table 18). It may be seen from Table 18 that the data to parameter ratio does only deviate for the error model options 5 and 6. While for error model option 5 (48.8099) the ratio is slightly higher than for options 1 – 4 (48.8079) it is slightly lower for error model option 6 (48.7980).

Table 18: Final R-values, Goodness-of-Fit, data to parameter ratio and highest peak and deepest hole for compound 1 using error model options 0 to 6.

Error model	R(F ²)	GoF	N _{data} /N _{par}	highest peak / eÅ ⁻³	deepest hole / eÅ ⁻³
0	2.43%	1.7991	48.8079	0.158(34)	-0.174(34)
1	2.43%	1.7991	48.8079	0.158(34)	-0.174(34)
2	2.49%	1.6980	48.8079	0.159(34)	-0.178(34)
3	2.63%	2.1082	48.8079	0.161(34)	-0.179(34)
4	2.68%	2.3039	48.8079	0.170(34)	-0.186(34)
5	2.60%	2.2491	48.8099	0.159(34)	-0.178(34)
6	2.65%	2.3165	48.7980	0.168(34)	-0.189(34)

A generally accepted indicator of model quality is the residual density. From the values for the highest peak and deepest hole in Table 18 it may be seen that also these also show a narrow distribution. The lowest value of the positive residual density is given as $0.158 \text{ e}\text{\AA}^{-3}$ when using error model option 0 or 1. The smallest value for the deepest hole is also achieved by using error model options 0 or 1 ($-0.174 \text{ e}\text{\AA}^{-3}$). However, taking the deviation into account the values do not differ significantly. Since the values for the highest peak and the deepest hole do not give any information about the spatial distribution of the residual density the fractal dimension of the residual density is examined. Figure 61 shows an overlay of the plots of the fractal dimension versus the residual electron density for all refined models. It needs to be noted that these plots are displayed at a different scale (X-axis range -0.2 to $0.2 \text{ e}\text{\AA}^{-3}$) than usual (X-axis range from -1 to $1 \text{ e}\text{\AA}^{-3}$). The highest maximum of the fractal dimension is achieved by using error model option 0 ($D_f(\text{max}) = 2.764$). As discussed in Chapter 3 the plot of the fractal dimension of the residual density for error model option 5 exhibits a small shoulder in the negative region. It can be said that the main differences can be spotted in the regions

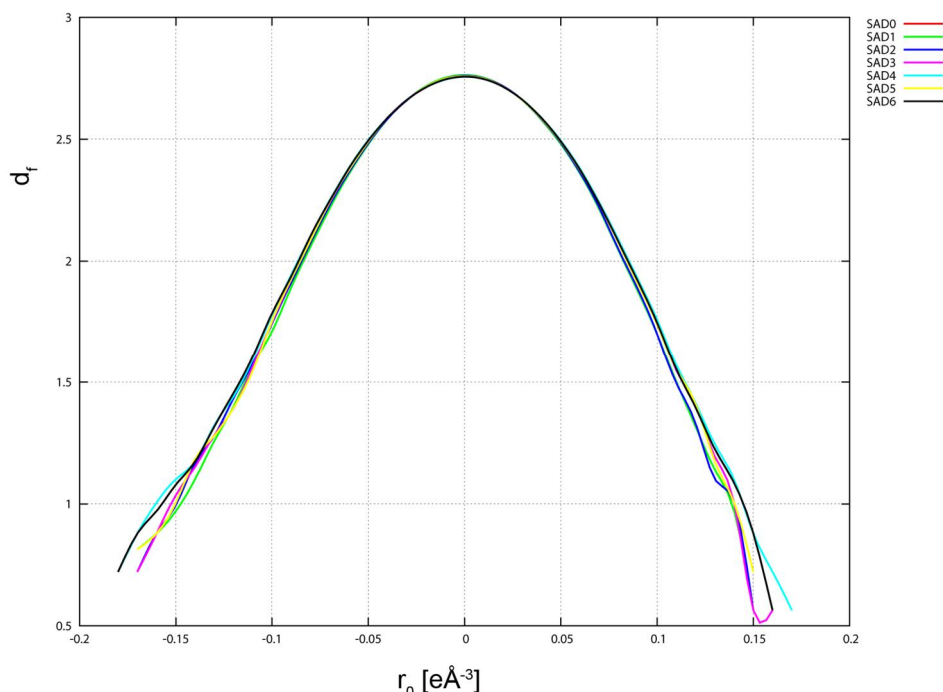


Figure 61: Plot of the fractal dimension of the residual density for all error model options. Error model 0 $D_f(\text{max}) = 2.764$; error model 1 $D_f(\text{max}) = 2.764$; error model 2 $D_f(\text{max}) = 2.761$; error model 3 $D_f(\text{max}) = 2.758$; error model 4 $D_f(\text{max}) = 2.756$; error model 5 $D_f(\text{max}) = 2.759$; error model 6 $D_f(\text{max}) = 2.757$.

Table 19: e_{gross} for compound **1**. Coefficient of variation: 1.5%.

Error model	e_{gross}
0	30.818
1	30.818
2	31.137
3	31.679
4	31.961
5	31.595
6	31.823

of high positive and negative residual density. The error model options 4 (cyan) and 6 (black) seem to perform slightly worse than the other options. These options show a less featureless distribution. The error model options 0 (green) and 1 (red) are exactly the same which is why the red curve can not be seen in Figure 61. However, the shape is almost paraboloid and sufficiently flat and featureless for

all models. Also the number of gross residual electrons within the unit cell e_{gross} shows that all models perform good. The lowest value for the e_{gross} is achieved by using the error model option 0 or 1. Furthermore the same trend as from the fractal dimension plots is visible. Error model options 5 and 3 are almost even. Error model option 2 performs slightly better than error model options 5 and 3. The error model options 4 and 6 perform worst. The overall variance of the e_{gross} equals to 1.5 %

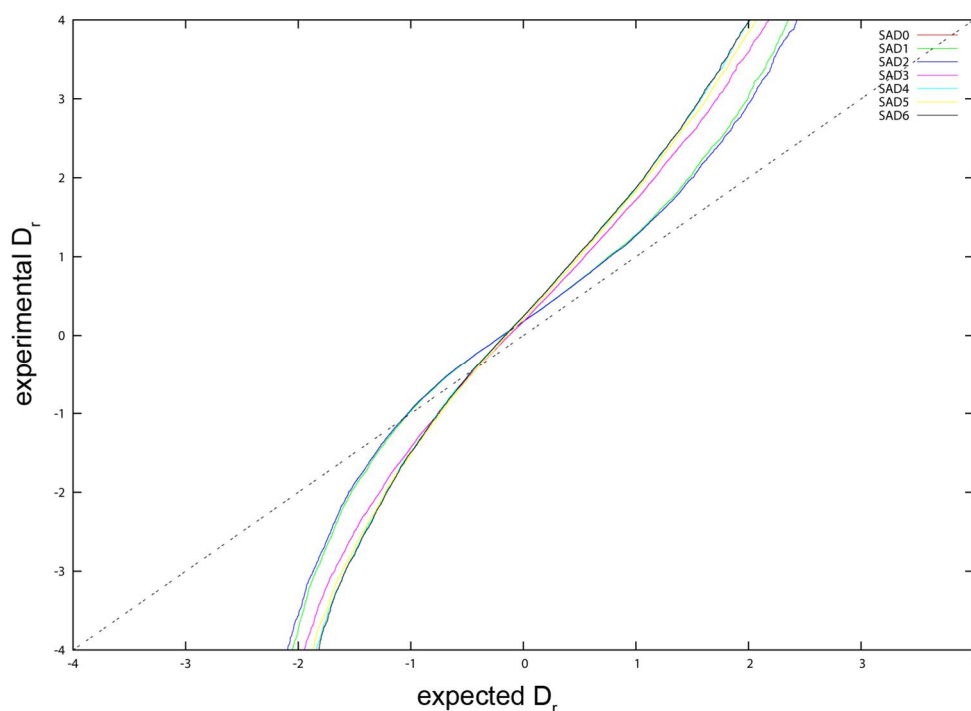


Figure 62: Overlay of the normal probability plots for error model options 0 to 6 for compound **1**.

which can be considered a low value.

In addition the normal probability plots for all error model options were analysed. It can be seen from Figure 62 that the distribution of the squared differences between expected and experimental structure factors is not normal for

the error model options 3 to 6 (Figure 62). For the error model options 0 to 2 the distribution does also deviate from normal distribution but not as pronounced as for the other options.

The analysis of the resolution dependence of the ratio between mean observed and calculated structure factors reveals that there is an influence on it. For error model option 0, 1 and 2 no value does exceed a variation of 5% from unity. The other error model options however do only slightly exceed this value (maximum deviation of $\frac{\sum F_o^2}{\sum F_c^2}$ for error model option 3 0.9482, error model option 4 0.9456, error model option 5 0.9485 and 0.9456 for error model option 2). When comparing the course of the plots in Figure 63 it may be seen that the main effects of the error model can be seen in the low resolution range from 0.0 to 0.2 $\sin(\theta)/\lambda$.

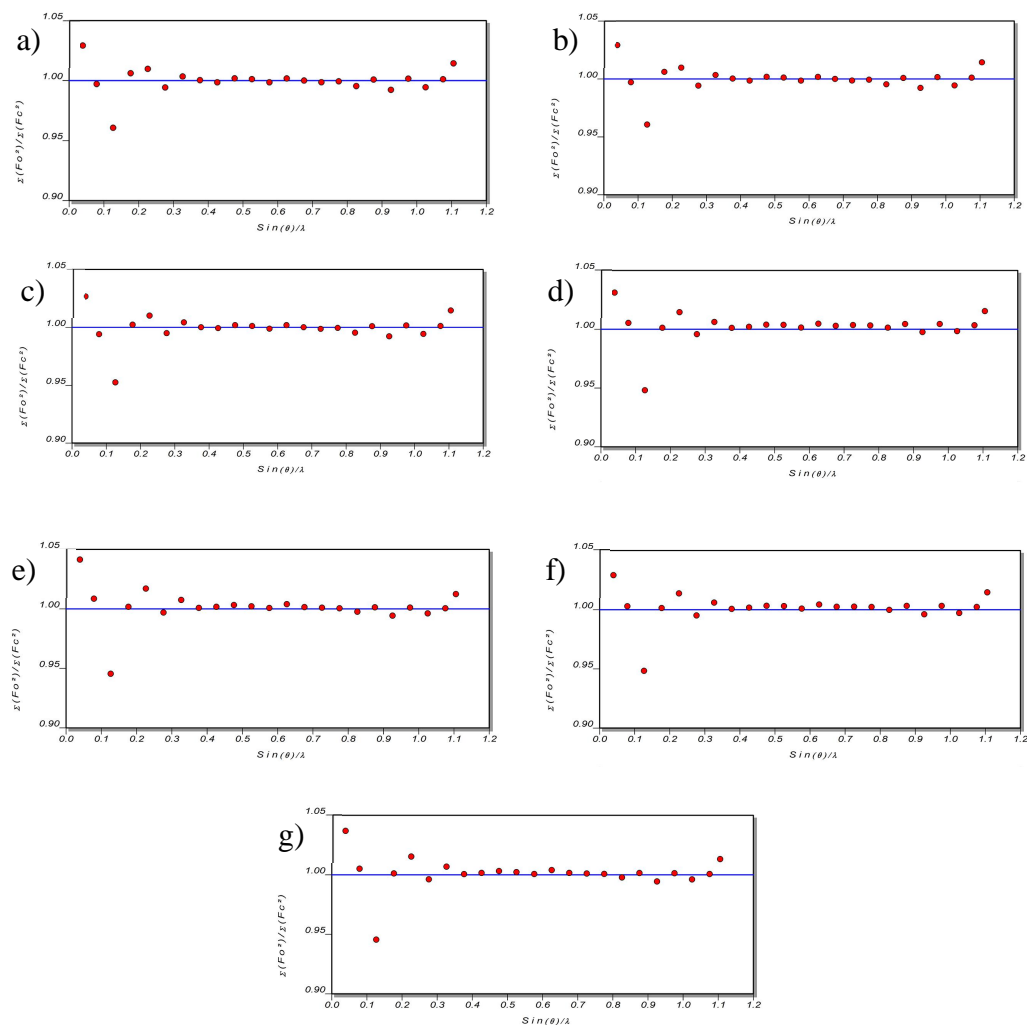


Figure 63: Resolution dependence of the ratio between mean observed and calculated structure factors. a) error model option 0; b) error model option 1; c) error model option 2; d) error model option 3; e) error model option 4; f) error model option 5; g) error model option 6.

Besides the model quality indicators also the refined parameters need to be closely examined. The properties calculated after the multipole model refinement are solely based on these parameters. Thus it needs to be revealed if deviations of these parameters are introduced by the error model. To test for deviations bigger than 3σ between the different models an automated program was written. The program first plots the parameter values for all error model options and then tests if the parameters deviate more than 3σ from each other. For the present compound the

monopole population and the population of the octupole O3+ for nitrogen atom N1 and thus also the thereupon constraint mono- and octupole population N4 deviate more than 3σ . Furthermore, the values of the expansion-contraction parameter κ for the nitrogen atoms N1 and N4 deviate (Figure 64). The monopole parameter M1 for nitrogen atom N1 shows a significantly higher value when using error model option 0, 1 and 2 whereas the linked expansion-contraction parameter κ shows a

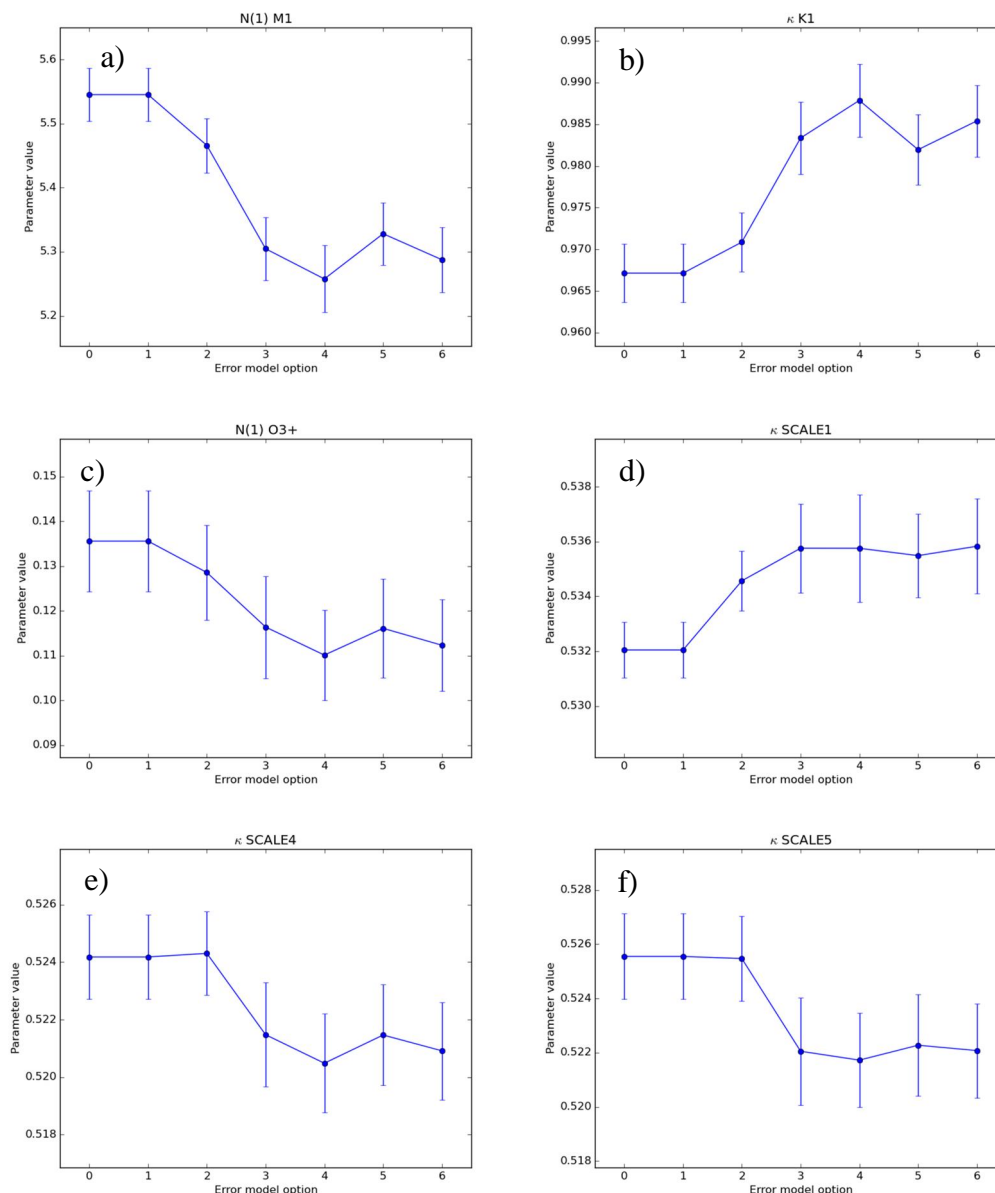


Figure 64: Plots of the values of the parameter a) monopole M1 for N1, b) κ 1 for nitrogen atoms N1 and N4 and c) octupole O3+ for the nitrogen atoms N1 and N4 d) scale factor number 1 e) scale factor number 4 f) scale factor number 5 in dependence of the error model option used. Error bars indicate 3σ range.

significantly lower value. The graphs in Figure 64 a) and b) show an inverse relationship. This is of course a consequence of the correlation between these two parameters. The trend observed from the model quality indicators can also be found in these plots. The error model options 0 to 2 form a group while a second group is formed by the error model options 3 to 6. Within the second group the absolute values of the error model options 3 and 5 are almost even. The same is true for options 4 and 6.

In summary it can be stated that for compound **1** only slight differences in the refined model are detectable. However, it needs to be examined if this does have an impact on the thereupon derived properties.

5.4 Differences in the derived properties for compound 1

In this chapter the influence of the error model on the derived properties shall be examined. Therefore a few remarks on the XDPROP program of the XD2006 suite need to be made.

As starting point, a search for bond critical points for all refined models has been carried out. Within the boundaries of the search criteria all refined models yielded in the same number of 70 BCPs and 2 RCPs found. As a first indicator this reveals that even the BCPs between lithium and nitrogen which are located in a region of shallow electron density are reliably found.

The value of ρ at the BCP has been examined including the estimated standard deviation. Considering the bonds involving atoms actually refined within the ligand molecule (see Table 5 on page 28) it may be seen that the values agree quite good (Figure 67). In general, all values lie within a 3σ range which indicates that these values are well defined and the influence of the error model option used is minimal. If only the absolute values are considered it can be seen that the error model options

0 to 3 exhibit slightly higher values of electron density than the options 3 to 6 (Figure 67). However, these are all covalent bonds which are relatively high in electron density compared to the closed shell interactions present in this molecule. The lithium - nitrogen closed shell interactions as discussed in Chapter 3 may show a stronger dependence on the used error model option than the covalent bonds.

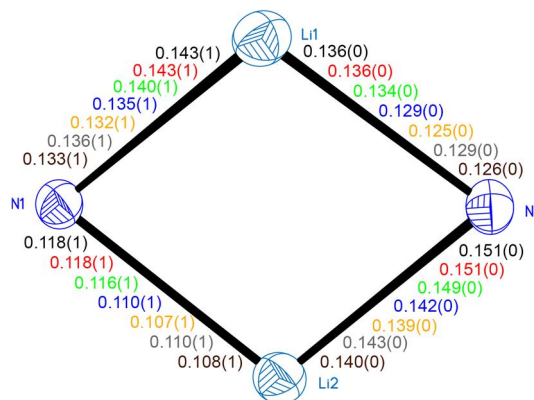


Figure 65: Values of ρ [$\text{e}\text{\AA}^{-3}$] at the BCPs for the central four membered Li_2N_2 ring. Black, error model option 0; red, option 1; green, option 2; blue, option 3; orange, option 4; grey, option 5; brown, option 6.

Therefore, these are examined in detail. For all error model options, the general trend between these bonds is preserved. This means in all cases the $\text{N4} - \text{Li2}$ bond shows the highest the $\text{N1} - \text{Li1}$ bond the second highest, the $\text{N4} - \text{Li1}$ the third highest and the $\text{N1} - \text{Li2}$ the least electron density at the BCP (Figure 65). Furthermore, it can be seen from Figure 65 that for all bonds the value of ρ at the BCP is highest for error model option 0 and error model option 1 and decreases with increasing error model option. In contrast to the covalent bonds, the values for both the $\text{Li1} - \text{N1}$ and the $\text{Li2} - \text{N1}$ bond differ by more than 3σ (Figure 65). However the absolute values show in general the same trend as the covalent bonds.

In contrast to the electron density the Laplacian of the electron density does show significant differences in between the seven compared models. Figure 68 shows the value of the Laplacian in dependence of the used error model option. It can be seen that for the graphs in Figure 68 a) to f) the error model options 0, 1 and 2 form a group of more similar values. The same is true for options 3, 4, 5 and 6 which form a second group. Within this group the absolute values of the options 3

and 5 do show lower values of the Laplacian than the options 4 and 6. The same trend can be observed for the lithium – nitrogen bonds (Figure 66).

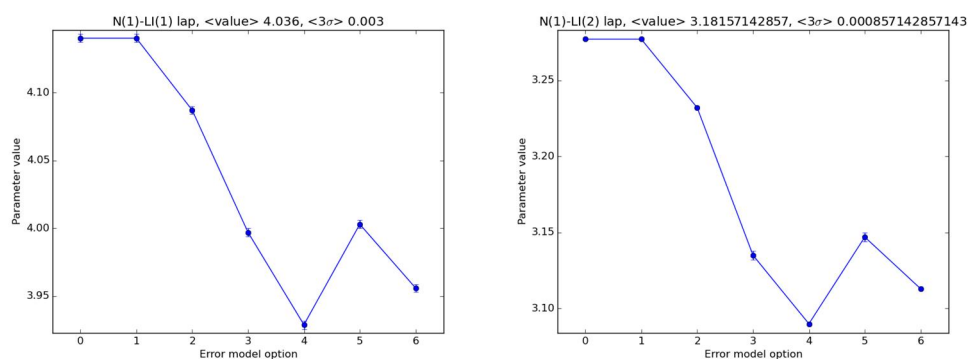


Figure 66: Plots of the Laplacian of the electron density $\nabla^2 \rho$ vs the error model option used including standard deviation for the Li1-N1 and Li2-N1 bond.

The deviations within the derived properties correlate well with the observations made for the model quality indicators and model parameters. In almost all model quality indicators considered, the options 0, 1, 2 performed slightly better than the options 3 to 6. Furthermore, the options 3 and 5 performed slightly better than the options 4 and 6.

Influence of the Estimated Standard Deviation on Charge Density Refinements

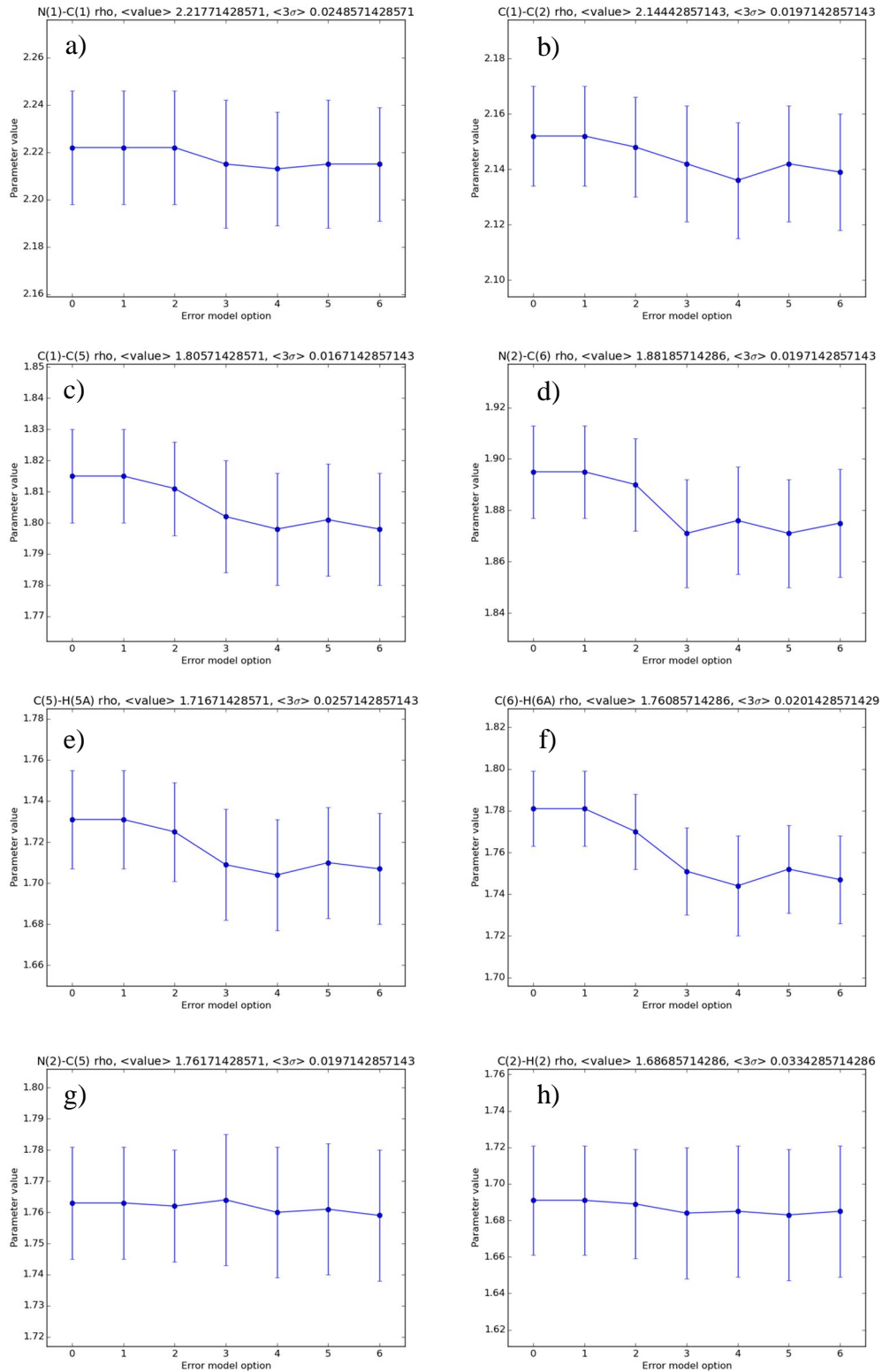


Figure 67: Plots of the electron density ρ vs the error model option used including 3 times the standard deviation.

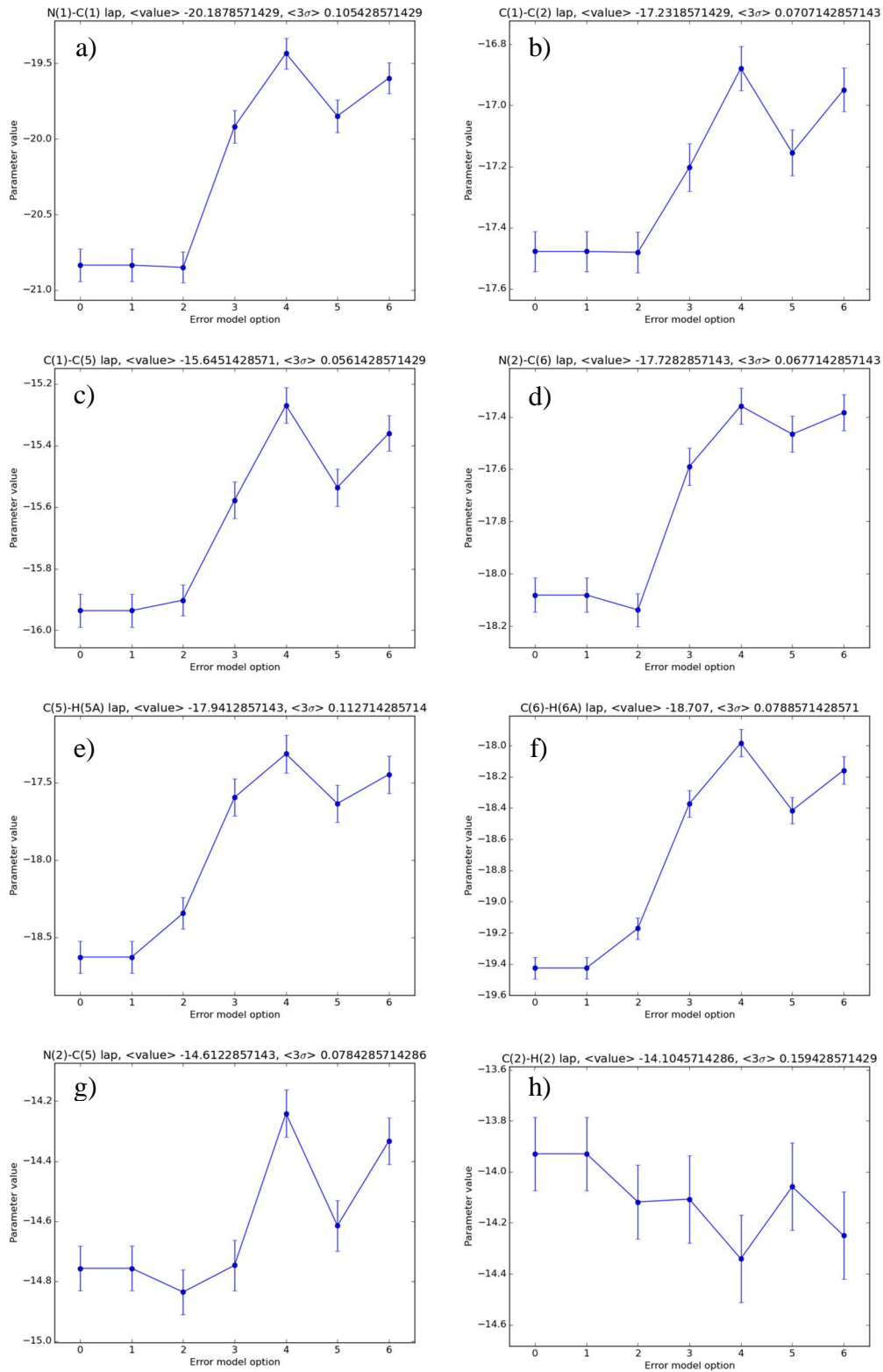


Figure 68: Plots of the Laplacian of the electron density $\nabla^2\rho$ vs the error model option used including 3 times the standard deviation.

5.5 Differences in the model for compound 2

A detailed analysis of the model quality indicators has also been carried out for compound 2. As for compound 1 the lowest R-value is achieved when using error model option 0 (1.88% see Table 20). The highest R-value of 2.32% is observed by using error model option 3. It is noteworthy that, in consistency with the R-values of compound 1, the error model options 3 and 4 perform worst.

The Goodness of Fit is closest to one for error model option 2. The error model options 5 and 6 exhibit the highest values of the GoF. This is also the fact for compound 1 (cf. Table 20).

Table 20 Final R-values, Goodness-of-Fit, data to parameter ratio and highest peak and deepest hole for compound 2 using error model options 0 to 6.

Error model	R(F ²)	GoF	N _{data} /N _{par}	highest peak / eÅ ⁻³	deepest hole / eÅ ⁻³
0	1.88%	1.6706	46.3398	0.295(56)	-0.347(56)
1	1.88%	1.5365	46.3398	0.244(57)	-0.338(57)
2	1.92%	1.4175	46.3398	0.246(56)	-0.337(58)
3	2.32%	1.6895	46.3453	0.291(61)	-0.363(61)
4	2.31%	1.7992	46.3453	0.293(61)	-0.357(61)
5	2.00%	1.8454	46.3564	0.261(34)	-0.345(59)
6	2.01%	1.8863	46.3425	0.250(59)	-0.350(59)

While the data to parameter ratio for the error model options 0 to 2 is invariant, it changes for the error model options 3 to 6. However, it does not vary drastically. For the second group it is slightly higher than for the error model options 0 to 2.

The analysis of the residual density regarding the highest peaks and deepest holes reveals that, the absolute values of the highest peak and deepest hole show a slightly higher distribution as for compound 1. But again, taking the deviation into account these differences are insignificant.

The analysis of the fractal dimension of the residual density as proposed by *Henn et al* confirm the observations made from the highest peaks and deepest holes (Figure 69). The featurelessness of the residual density as indicated by the maximum of the fractal dimension does vary in a narrow range (see Figure 69). In general, it can be seen that the features of the distribution of the fractal dimension of the residual density are preserved for all

Table 21: c_{gross} for compound 2. Coefficient of variation: 3.2%.

Error model	c_{gross}
0	271.084
1	273.595
2	276.750
3	293.642
4	292.981
5	280.727
6	280.715

error model options. All plots in Figure 69 show slight shoulders in the negative region of the residual density. It can be seen that the shoulder is more pronounced for the error model options 4 and 6 while it is minimal for error model option 0. Additionally, the error model option 0 does show a slight shoulder in the positive region, which is less pronounced for the other error model options. In the positive

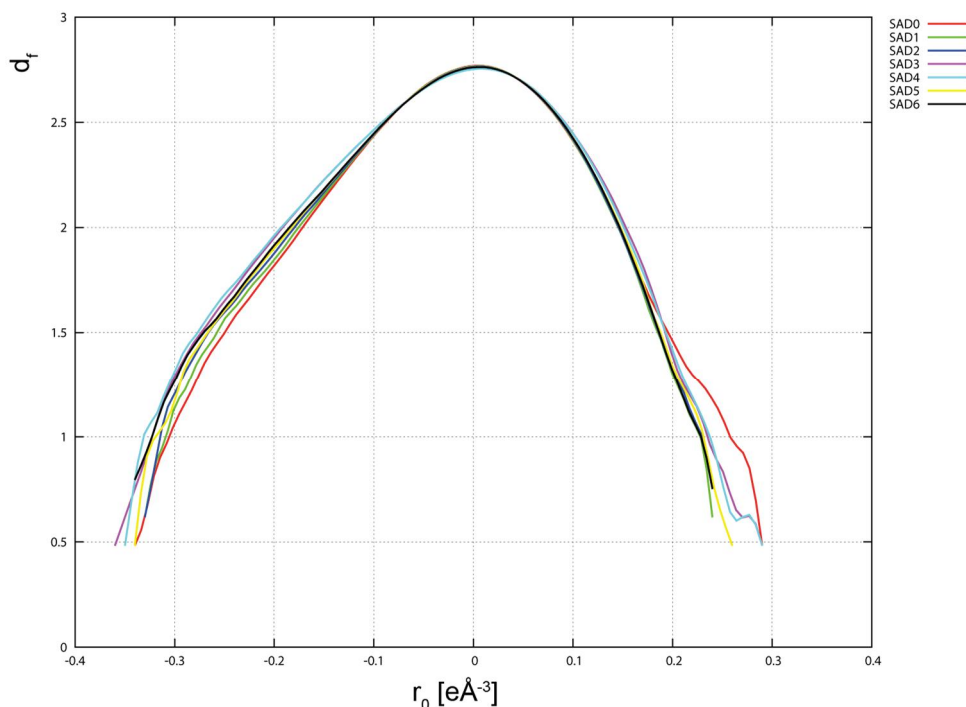


Figure 69: Plot of the fractal dimension of the residual density for all error model options. Error model 0 $D_f(\max) = 2.769$; error model 1 $D_f(\max) = 2.767$; error model 2 $D_f(\max) = 2.765$; error model 3 $D_f(\max) = 2.753$; error model 4 $D_f(\max) = 2.753$; error model 5 $D_f(\max) = 2.763$; error model 6 $D_f(\max) = 2.762$.

region the error model options 1 to 6 perform equally well. The lowest value for the e_{gross} is achieved by using error model option 0 (Table 21). The e_{gross} increases with ascending error model option until it reaches its maximum at error model option 4. For the error model options 5 and 6 it then again slightly decreases. The coefficient of variation calculates to 3.2% which can still be regarded small.

The ratio of the observed and calculated mean structure factors in dependence of the resolution for compound **2** shows similar trends as for compound **1**. For the present compound the ratio of the observed and calculated mean structure factors for the error model options 3 to 6 do almost exceed the range of 5% deviation from unity. The highest deviation does occur in the resolution range from 0.1 \AA^{-1} to

Influence of the Estimated Standard Deviation on Charge Density Refinements

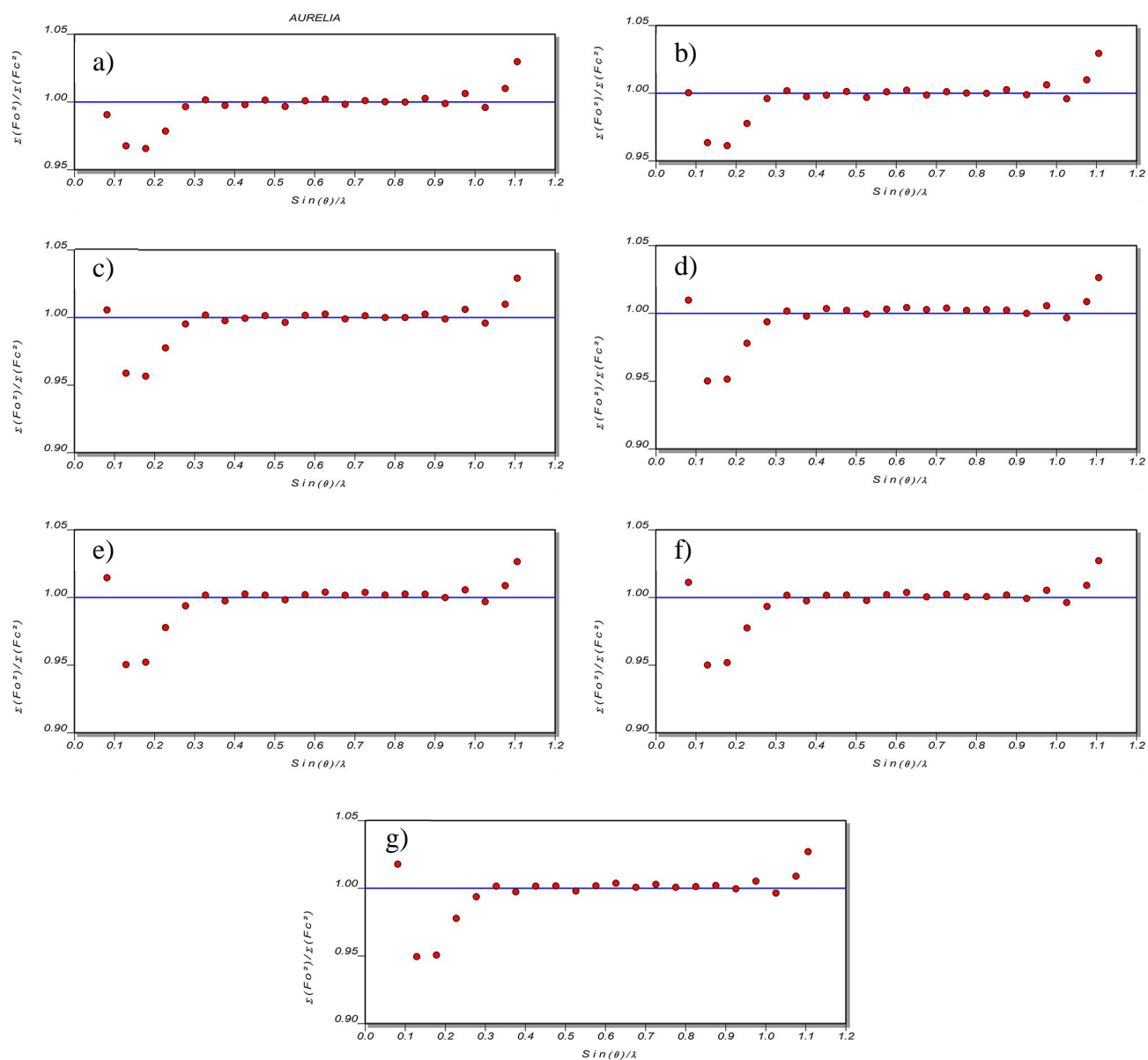


Figure 70: Resolution dependence of the ratio between mean observed and calculated structure factors. a) error model option 0; b) error model option 1; c) error model option 2; d) error model option 3; e) error model option 4; f) error model option 5; g) error model option 6.

0.2 \AA^{-1} . The most noticeable changes do occur in the low resolution range. This does confirm the observations made for compound **1** that the influence on the ratio of the mean observed and calculated structure factors is biggest in the low resolution region. From this criterion, it seems to be favourable to use error model options 0 or 1.

In addition the normal probability plots for all error model options were analysed. It can be seen from that the distribution of the squared differences

between expected and experimental structure factors is not normal for the error model options 3 to 6 (see Figure 71). The slope of the lines for the error model options does in no range show a normal distribution (indicated by the dashed line)

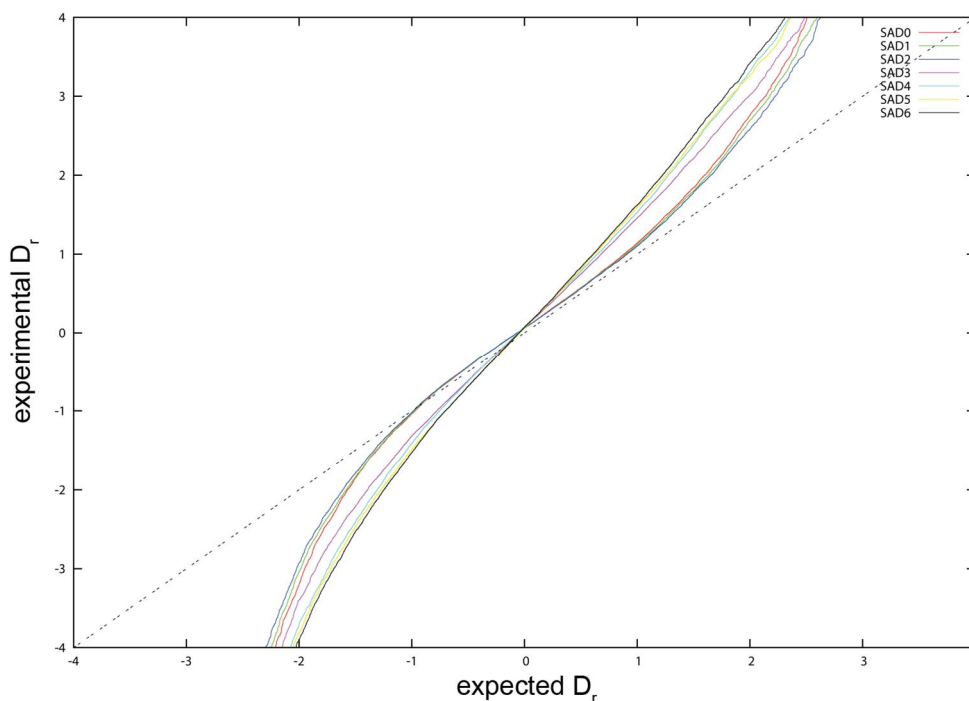


Figure 71: Overlay of the normal probability plots for error model options 0 to 6 for compound 2.

For the error model options 0 to 2 the distribution does also deviate from normal distribution but not as pronounced as for the other options. Within the X-axis range of -1 to 1 these error model options exhibit normal distribution. Error model option 2 (blue line in Figure 71) is the one closest to normal distribution.

Table 22: List of refined parameter that vary more than 3σ .

Atom	Parameter	Atom	Parameter
F(1)	M1	F(7)	C333
K(1)	U33	O(1)	X
K(1)	C333	O(1)	Y
K(1)	C123	O(1)	U22
O(2)	U11	B(1)	D0
F(9)	C333		SCALE 1
K(4)	U33		SCALE 3
K(3)	U33		SCALE 4
K(5)	U33		SCALE 5
K(5)	C333		SCALE 6
K(5)	C113		

The analysis of the refined parameters reveals that mostly the thermal motion parameters and Gram-Charlier coefficients do show a deviation larger than 3σ . Regarding the multipole populations, only the monopole population (M1) of Fluorine atom F1 and a dipole population (D0) of B1 do vary significantly. In total 21 of 371 refined parameters vary more than three times the standard deviation (see Table 22). It can be seen that 6 of the deviating parameters are Gram-Charlier coefficients.

This is due to the fact that these are, for this compound, small in their absolute value and the resulting esd is calculated to a value of 0.0. These parameters will therefore not be discussed further. It is also not surprising that the thermal parameters and the scaling factors deviate more than 3σ as these are correlated.

The values of the multipole parameters of boron atom B1 and fluorine atom F1 that deviate more than 3σ in dependence of the error model option used are shown in Figure 72. In general, it can be seen, that the absolute values are close and the

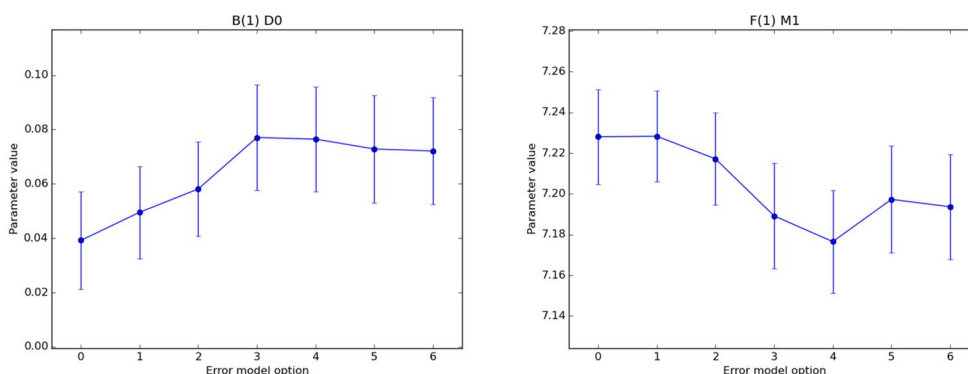


Figure 72: Plots of the refined multipole parameters for boron atom B1 and fluorine atom F1 which deviate more than 3σ in dependence of the used error model.

deviation is close to 3σ

In conclusion it can be said that for the present compound the models do exhibit only slight significant differences. The R-value as well as the resolution dependence of the observed and calculated mean structure factors, the normal probability plot and the number of gross residual density electrons seem to favour error model option 0 to 2. Still, most of the refined parameters are in good agreement between the models. From the R-values and the analysis of the fractal dimension of the residual density the error model options divide in three groups, error model options 0 to 2 which perform best, error model options 5 and 6 performing second best and error model options 3 and 4 performing worst.

5.6 Differences in the derived properties for compound 2

From Table 13 in Chapter 4 it can be seen that only multipoles for the atoms C1, C2, B1, F1, O1, H1 and H2 are refined. Therefore, meaningful standard deviations can only be obtained for bonds involving these atoms. In Figure 73 plots of the electron density in dependence of the error model option used are shown. In

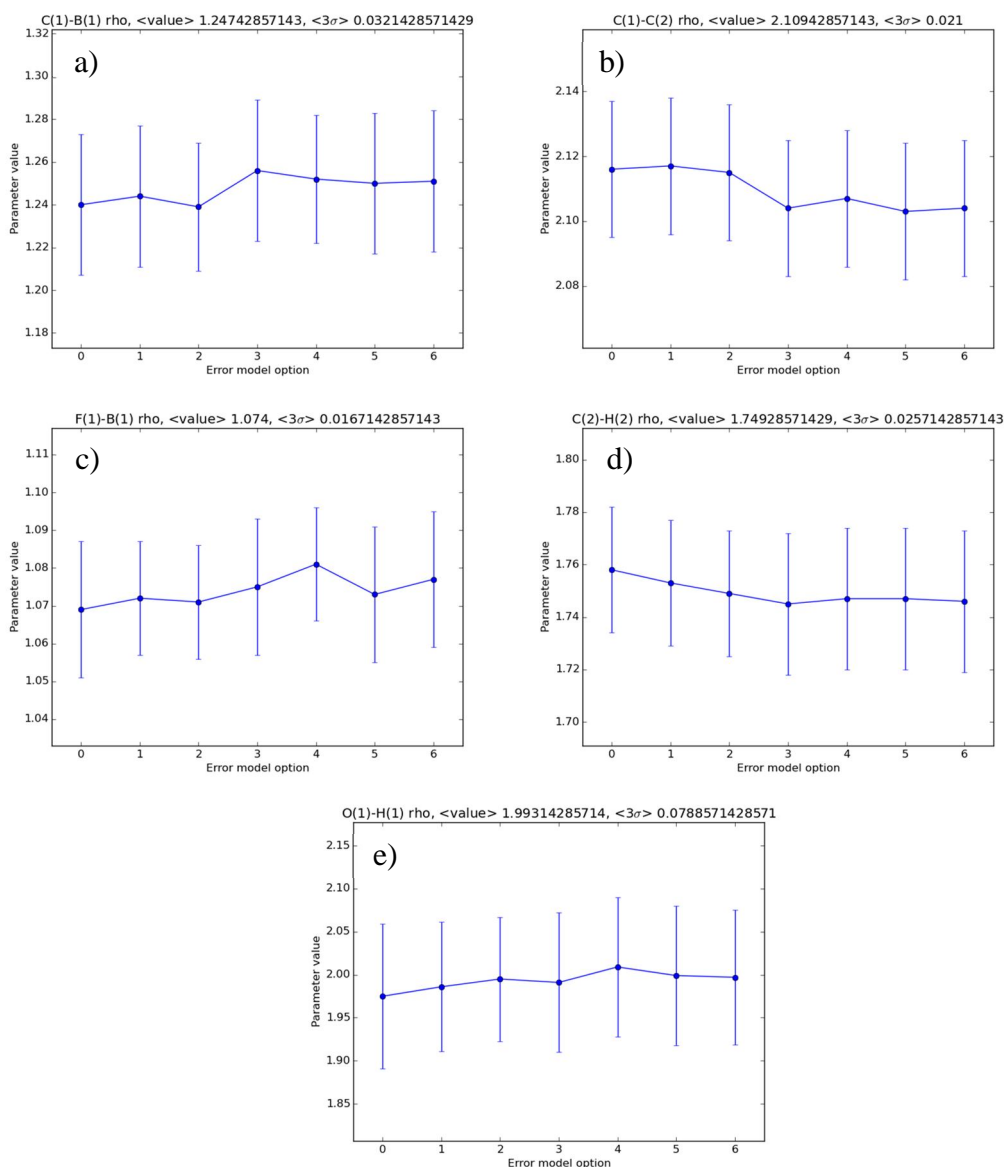


Figure 73: Plots of the electron density ρ vs the error model option used including 3 times the standard deviation.

general, it can be seen that all the values show no significant deviation. When only considering the absolute values of ρ at the bond critical points it can be seen that for the C1-B1 bond and the C1-C2 bond the error model options 0 to 2 and 3 to 6

seem to form two groups. The agreement within the groups seems to be better than between the groups. However, it needs to be noted that within a 3σ range these values are the same.

In contrast to ρ the Laplacian of the electron density does show significant deviations (Figure 74). Except for the oxygen–hydrogen bonding O1 – H1 of the

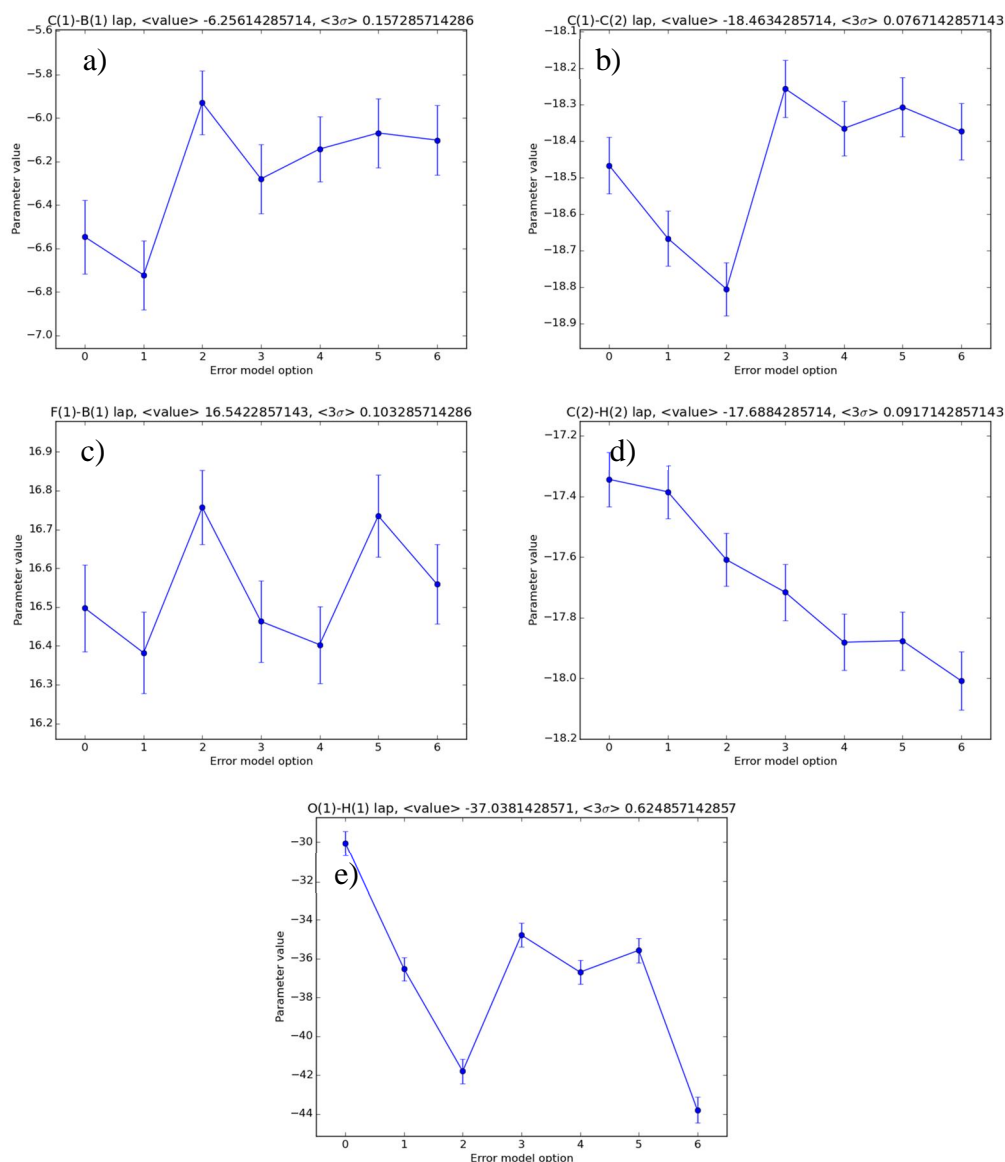


Figure 74: Plots of the Laplacian of the electron density $\nabla^2\rho$ vs the error model option used including standard deviation.

water molecule the absolute values of the Laplacian shows a narrow distribution ($\approx \pm 1 \text{ e}\text{\AA}^{-5}$). In contrast to that the oxygen hydrogen bond shows a difference between

minimum and maximum value of approximately $14 \text{ e}\text{\AA}^{-5}$. From Figure 74 a) to d) no clear trend as for compound **1** is visible. In addition, the grouping observed for the model quality indicators is not resembled within the values of the Laplacian, as for compound **1**. It can be seen that there is no obvious trend. This is also true for potassium fluorine interactions which represent regions of shallow electron density. In Figure 75, plots of the electron density and the Laplacian for selected potassium fluorine contacts are shown. It can be seen that the electron density at the BCP does hardly vary even for this type of interaction. The Laplacian shows some variations but the distribution of the values is quite flat.

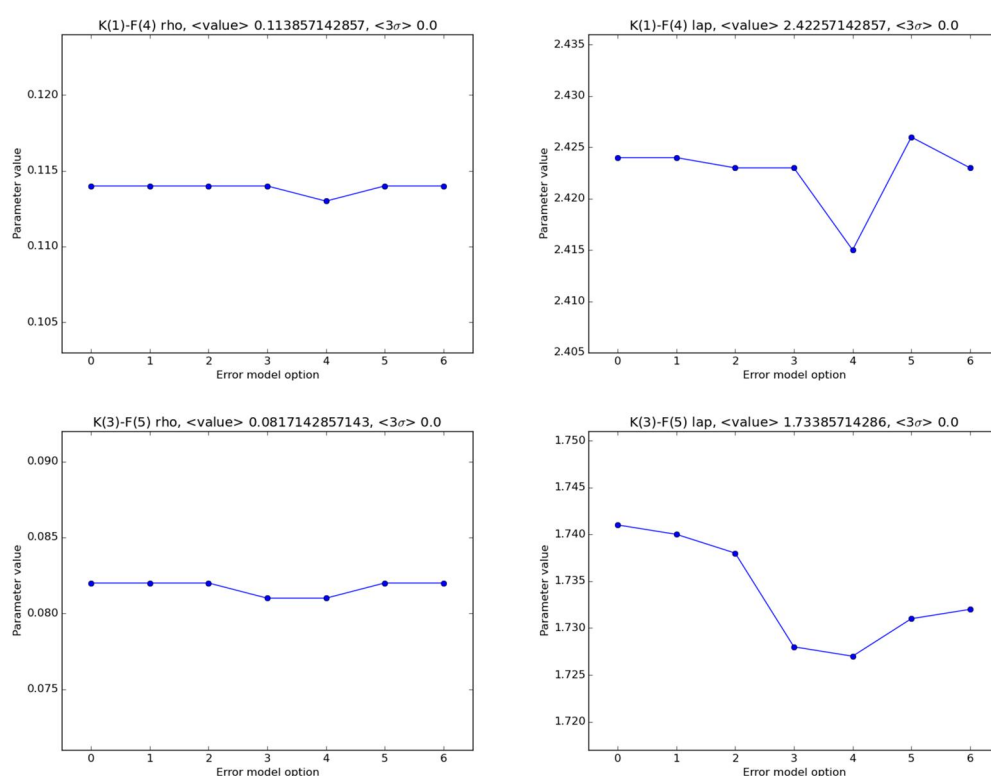


Figure 75: Plots of the value of ρ (right) and the Laplacian (left) at the BCP in dependence of the error model used for selected potassium fluorine contacts.

5.7 Conclusion

In conclusion it could be confirmed that as *Jørgensen et al* stated the influence of the error model on the refined model within a multipolar model refinement is in fact minimal.^[135] If the model quality indicators are considered it seems favourable to use error model options 0 to 2. For these error model options, in both cases tested, the R-values as well as the e_{gross} exhibit the lowest values. Furthermore, the

distribution of the squared differences of the experimental and calculated structure factors is more normal for these error model options. It could be shown that the model parameters are hardly deviating in dependence of the error model.

The influence on the derived properties of the electron densities has also been examined. The electron density ρ itself has proven to be quite stable. Significant deviations have only been observed for the lithium – nitrogen bonds in compound **1**. As well as the potassium – fluorine interactions they are characterised by low electron densities at the bond critical points. Therefore, it is not unexpected that these interactions show the highest deviation for the values at the BCP. However, even the distribution of the absolute values of the lithium – nitrogen and potassium fluorine interactions shows a narrow range. From the lithium – nitrogen interactions it could be shown that the relation between the electron densities for the Li₂N₂ ring in compound **1** is preserved for all error model options.

The Laplacian, which reveals the subtle features of the electron density, shows significant deviations for the examined compounds. At least for compound **1** the deviations show a similar behaviour as the model quality indicators. However, the calculation of the estimated standard deviations (esd) within XDPROP is in the current version of the program severely limited. First of all the calculation of esds is only possible for dipole moments, ρ and $\nabla^2\rho$. The calculation of the esds for ρ and $\nabla^2\rho$ does at the moment only take contributions from the multipole populations into account. This means neither coordinates or thermal vibration nor the expansion contractions parameters do have an effect on the standard uncertainties. Additionally, symmetry generated atoms are not taken into account. Furthermore, the standard deviations for atoms chemically constraint to another atom do not appear in the variance-covariance matrix on which the estimated standard uncertainties are calculated. This means meaningful esds are only calculated for atoms that are not chemically constraint to any other atom. *Kaminski et al* and *Krause et al* already addressed this topic in two different ways. *Kaminski et al* used a large number of measurements of α -oxalic acid dihydrate which is used for diffractometer calibration to calculate standard deviations.^[145] They could thereby

show that the standard deviation of the electron density as calculated by XD2006 is in good agreement with those calculated from multiple measurements. However, their study showed that the standard deviations of the Laplacian of the electron density is underestimated by XD2006 ($> 1 \text{ e}\text{\AA}^{-5}$) compared to the one obtained from multiple measurements (several $\text{e}\text{\AA}^{-5}$). To estimate standard deviations of the properties *Krause et al* use the refinements obtained from their implementation of R_{free} .^[30] Using their method, the authors showed that the standard deviation of $\nabla^2\rho$ is underestimated by a factor of ten by XD2006. Bearing this in mind, even the deviations in the Laplacian can be considered insignificant.

To further confirm or falsify these results more and as different as possible compounds should be tested. *Hilke Wolf* already showed that for crystal structures containing only light atoms the influence on the derived parameters can be considered negligible.^[146] However she did not comment on the thereupon derived properties. Especially compounds where open shell interactions with values of the Laplacian at the BCP very close to zero exist. It would be interesting to see if the value of the Laplacian changes sign from positive to negative. This would be in contrast to the definition of an open shell interaction according to Baders quantum theory of atoms in molecules. If only a singular error model option is evaluated this may be misleading.

In summary, the error model options 0 to 2 should be used to ensure the best model quality even if the model parameters and the derived properties are barely influenced.

6 Short Term Stability of X-ray detectors

Modern high resolution X-ray crystallography requires sufficiently brilliant sources. With the increase in brilliance it is possible to get complete datasets in less time. Furthermore, macromolecular crystallography which is usually carried out at synchrotron facilities can be achieved in house.^[147] However, with increasing source intensities by using for example *excillums MetalJet* or new high brilliance rotating anodes the demands for the detector also rise. *Howard et al* elaborated on the desirable properties and characteristics an X-ray detector should have.^[148] The characteristics they list are:

- detection efficiency η
- linearity of response
- proportionality
- sensitivity
- dynamic range
- spectral sensitivity
- energy resolution
- spatial resolution
- stability in time
- resistance against radiation damage

From these some are of bigger importance when it comes to high resolution data measurements with high-brilliance sources. As *Jakob Hey* already concluded in his PhD thesis the *dynamic range* (which is in general defined by the ratio of the highest and smallest detectable value) is of high interest especially when using high energy X-rays (synchrotron radiation, silver or indium sources). In this case, due to the compressed reciprocal space reflections with a broad variety of intensities occur in one frame. Furthermore, the *stability in time* is of importance. In principle, as defined by *Aslanov et al* this translates to the precision of the detector. This point is of great importance for modern area detectors because reflections are measured numerous times and later on used for example for computational methods like semi-empirical absorption correction.

X-Ray detectors have come a long way from Laue cameras through point detectors and charge-coupled devices (CCD) and complementary metal-oxide-semiconductor (CMOS) sensors to the most recent hybrid pixel counting and charge-integrating pixel array detectors (HPC, CPAD respectively).^[149,150] During the work on this thesis the acquisition of a new specialised high resolution diffractometer for the work group was envisaged. Therefore, several tests regarding the source as well as the most suitable detector were carried out by different members of the work group. In this thesis 3 different detectors (APEXII, PHOTON 100, PILATUS3 X CdTe) from 2 manufacturers (BRUKER and DECTRIS) have been tested for their stability in time.

6.1 Working principle of the used X-ray detectors

The three detectors used for the stability test all differ by the sensor used. The detectors manufactured by BRUKER, the APEXII and the PHOTON 100, are so called integrating detectors while the DECTRIS PILATUS3 R CdTe is of the HPC type. The major difference between these two types of detectors is that integrating detectors sample a charge, generated by photons within a semiconductor sensor, over a certain integrating time while counting detectors do count charge pulses induced by single photons. Furthermore, the two integrating detectors differ by the choice of their sensors. The APEXII features a CCD as sensor. The PHOTON 100 makes use of a CMOS for converting photons to electrons. In the next three sections the different sensor types will be explained. Another major difference is that the PILATUS3 R CdTe does not use a scintillator but the X-ray photons are directly converted in the cadmium telluride semiconductor material.

6.1.1 CCD sensors vs CMOS sensors

The basic layout of a CCD based X-ray detector is presented in Figure 76. A CCD is built up by a N-type semiconductor layer upon an P-doped layer, thus forming a diode. By applying a positive voltage to the N-doped Layer and a negative voltage to the P-doped layer a depletion area (potential well) is

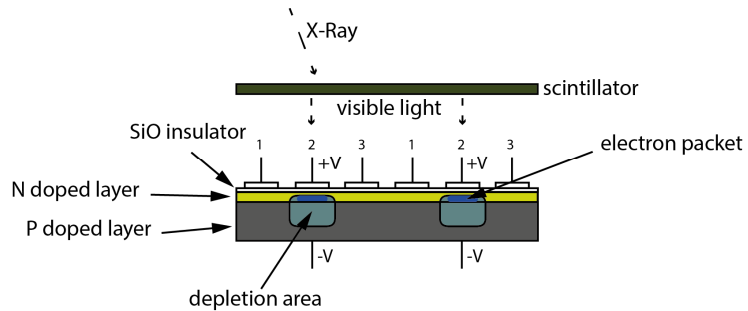


Figure 76: Schematics of a CCD based detector.

produced, in which electrons, generated by visible light, can accumulate. To produce the visible light needed for detection with a CCD the X-ray photons need to be converted. This is done by the scintillator. The scintillator, which is also called phosphor, can be produced from various materials. One of the most often employed materials is terbium doped gadolinium oxysulfide (GADOX) but for example europium doped yttrium oxide may also be used. The X-rays excite the scintillator and it emits visible light.

During the exposure time charge accumulates in the depletion area which is then without further exposure read

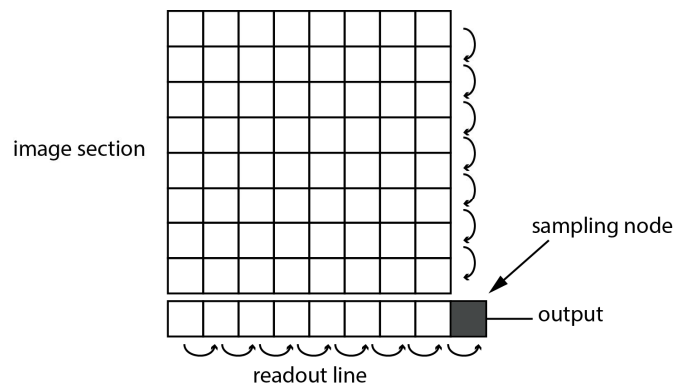


Figure 77: Readout process in Full Frame (FF) mode

out from the chip. The readout is in principle done row by row (Figure 77). By applying a cycling alternating voltage (clock) to the electrodes 1, 2 and 3 (see Figure 76) the depletion area and therewith the charge can be shifted through the chip. Because of this shifting process physical borders between pixels are only used between the columns but not between the rows of pixels. In Figure 77 the bottommost line of the frame section is shifted to the readout line while every line above is shifted one column downwards (vertical). In the readout line the charges

are shifted horizontally to the sampling node and read out. The signal is then amplified and processed after it is read out from the chip.^[151]

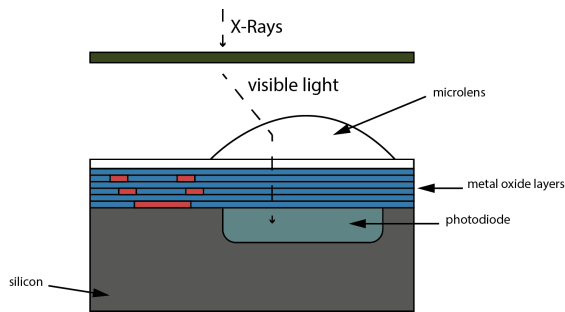


Figure 78: General layout of a CMOS pixel

Figure 78. The visible light is converted into a charge by the photodiode beneath the metal-oxide layer. Within the metal-oxide layer the wiring and transistors for read out, amplification etc. is embedded. A micro-lens is attached to direct light to the photodiode.

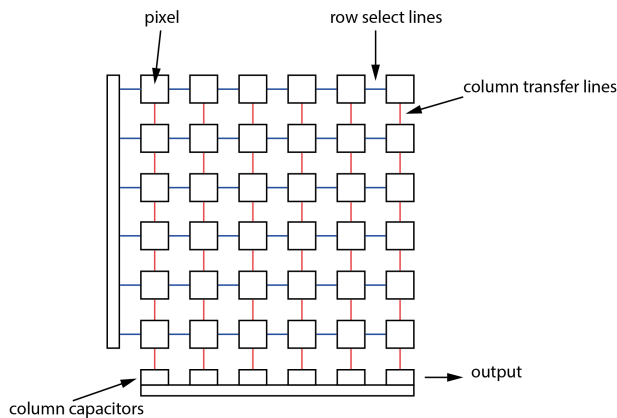


Figure 79: Schematics for the read out process in a CMOS

In contrast to that, in a CMOS sensor the amplifying, read out as well as other functionality can be embedded on the chip for each individual pixel. The general layout of a CMOS pixel is sketched in **Figure 78**. The visible light is converted into a charge by the photodiode beneath the metal-oxide layer. Within the metal-oxide layer the wiring and transistors for read out, amplification etc. is embedded. A micro-lens is attached to direct light to the photodiode.

Due to the embedded wiring and transistors each pixel can be read out individually by selecting the appropriate row select and column transfer line (**Figure 79**).^[151]

In the following paragraphs

some advantages and disadvantages of the sensors will be confronted.

Having in mind the read out schemata it is obvious that this process is much faster in a CMOS detector. There is no need for a clock that shifts the charge to the read out line as in the CCD. The faster read out not just minimizes the dead time (time between two measurements) but also enables the detector to operate in shutter less mode. However, the decrease in dead time by the faster read out in traditional shuttered measurements is minimal because most of the dead time is used for repositioning the goniometer and driving and synchronizing the movement of the stepper motors.

Another important thing to consider is the noise. The noise of these detector types however is influenced by many factors (e.g. thermal noise, shot noise). One

source of error is the amplification of the charge created by the sensor. As discussed earlier the amplification is different in the CMOS and the CCD sensor. While within the CCD sensor only one amplifier is used, in the CMOS each pixel has got its own amplifier. As each individual amplifier contributes to the noise, the CMOS should show slightly higher, more random noise. In contrast the CCD sensor only uses one amplifier which should result in a more uniform noise. However, this issue is addressed by using low noise amplifiers within CMOS detectors.^[152,153]

Another factor, which becomes obvious when Figure 76 and Figure 78 are considered is, that the actual sensitive area of a CMOS is smaller compared to a CCD sensor. This is a consequence first of amplifier and additional functionality embedded on the top side of the sensor and second that the CCD in principle is one large photodiode which is segmented into pixel while the CMOS has embedded photodiodes in a layer of silicon. In a CCD only wiring for the horizontal pixel separation is needed.

Overall, both sensor technologies are well established and show a wide variety of applications. In regard of the *stability in time* it can be expected that the sensors perform in a quite comparable way.

6.1.2 Hybrid Pixel Counting sensors

As already mentioned HPC detectors do not measure a charge accumulated over time as CCD or CMOS detectors but charge pulses. Besides this the major difference to the detectors introduced in the previous chapter is that the X-ray photons are directly converted to an electric charge without the use of a scintillator.

The detecting material used in the examined DECTRIS PILATUS3 R detector is cadmium telluride (CdTe). For the direct detection of X-Rays by this material the high atomic number ($Z_{\text{Cd}} = 48$; $Z_{\text{Te}} = 52$) of the material compared to others like silicon is beneficial for the absorption efficiency. CdTe is especially capable of detecting high energy radiation such as low wavelength X-rays and γ -radiation. This makes it ideal for synchrotron application as well as for silver and indium home lab X-ray sources. Despite these advantages CdTe has several disadvantages One of them is the contamination with impurities originating from the production

of Cd and Te. These impurities need to be compensated by doping of the CdTe sensor material. Another issue is the temporary trapping of charge carriers within the conduction band. This leads to a broadening of the detected charge pulses. Additional to this also polarisation effects occur. These can on the one hand stem from the applied high voltage and on the other hand from the photon flux itself. All these factors might decrease the short and long term stability of detectors using

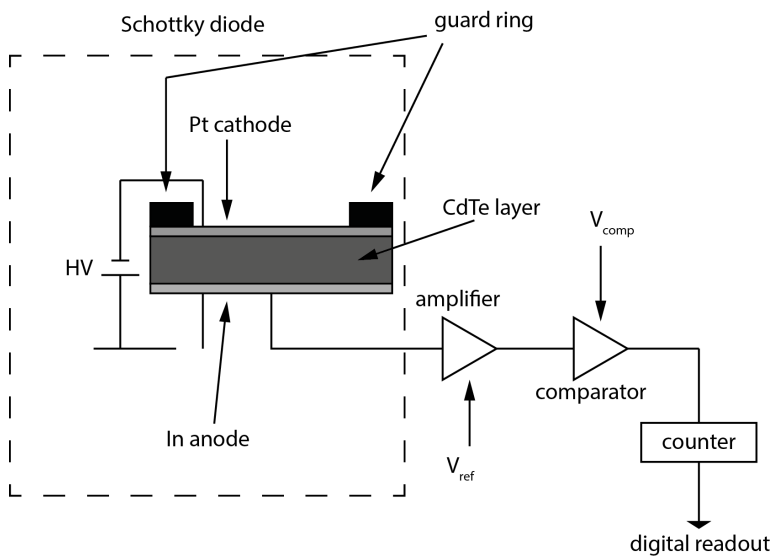


Figure 80: Schematic drawing of the working principle of a CdTe HPC

When hit by an X-ray photon an electron - hole pair is generated. The electrons move towards the indium anode while the holes are directed towards the platinum cathode. The charge is then amplified by the by the amplifier. The comparator compares the amplified charge to a reference (V_{comp}) and then emits a signal if the incoming charge exceeds this value. The emitted signal is fed into a counter which can be read out digitally. The digital storage of the number of photons is advantageous because for example a 20-bit counter (Pixel) alone is able to count ~1 million photons. Further improvement can be achieved when overflow counters are implemented. This build features a guard ring which works as the pixel border. Unfortunately, photons which hit the guard ring are not detected. This also affects the reproducibility of the measurement.

CdTe as detection material.

The general layout of a HPC detectors is depicted in Figure 80. It consists of the detection material (in this case CdTe) usually in the form of a Schottky diode.

6.2 Temporary adaption of a PILATUS3 R CdTe to a BRUKER D8 Diffractometer

While the PHOTON 100 and the APEXII are available with diffractometers sold by BRUKER and can be used without further modification the DECTRIS PILATUS3 R CdTe needs to be adapted to the respective diffractometer. In the stock configuration in a BRUKER diffractometer a measurement is planned using the frame buffer PC. The data collection strategy is transferred to the D8 goniometer

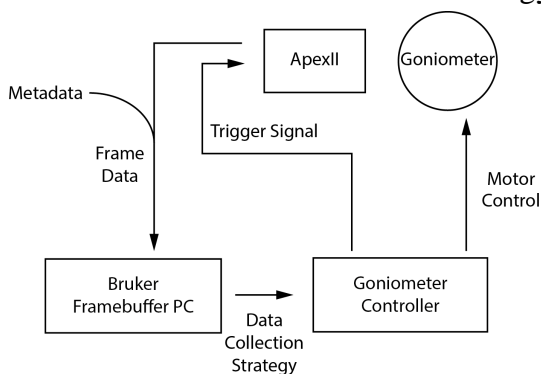


Figure 81: Normal operation of a Bruker D8 diffractometer.

controller. The goniometer controller then does open the safety and timing shutters, drives the stepper motors according to the selected scan type (ω - or ϕ -scan and κ if available) and sends the trigger signal to the detector. The trigger signal is a square-wave voltage with the duration of the exposure time

(cf. Figure 81).

When the program which establishes the connection to the goniometer controller is started, several checks are performed. One of them tests if a detector is present. This means that for operation with a non-BRUKER detector either a software

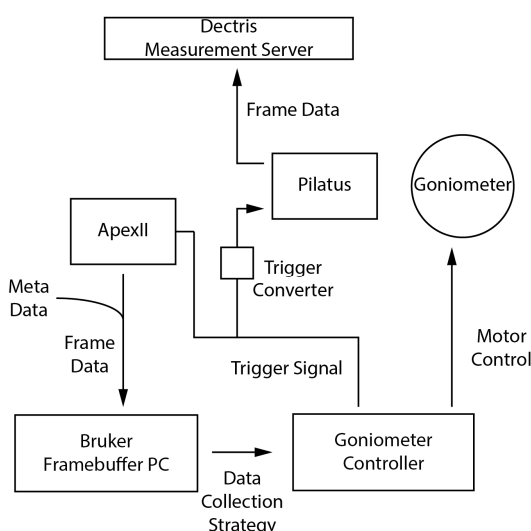


Figure 82: Operation principle with the DECTRIS PILATUS3 adapted to the diffractometer.

dummy needs to be present or the APEXII needs to be operated in parallel to the other detector. As can be seen from Figure 81 the meta data such as position of the goniometer (ω -, ϕ -, 2θ -position, exposure time) is fed into the frame data and stored within the header of the individual frames. If a software dummy is used, this information is lost. In parallel operation a frame with no

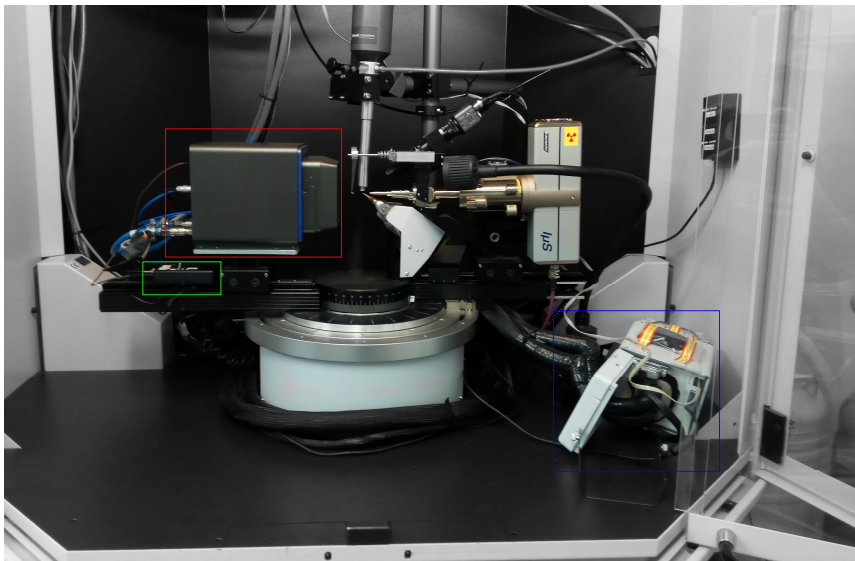


Figure 83: Photograph taken of the finished adaption of the PILATUS3 to a BRUKER D8 diffractometer. The red square encloses the PILATUS3; the green square encloses the trigger converter box; the blue square encloses the APEXII.

signals is detected, but the meta data is recorded.

To operate the DECTRIS PILATUS3 R CdTe detector the APEXII is interchanged

and put aside within the D8 housing. The trigger signal by the goniometer controller is split and fed into the APEXII and a trigger signal converter which is connected to the PILATUS3. The PILATUS3 is connected to the DECTRIS measurement server PC which controls the functions of the detector and stores the individual frames. With the measurement server rudimentary metadata can be added to the frames however with sophisticated strategies this method is not feasible. The metadata is recorded by the APEXII and later on transferred to the recorded frames. The principle of operation is shown in Figure 82. To measure, a normal experiment is planned within the APEX 2 software suite at the Bruker frame buffer PC and the PILATUS3 is set to external trigger mode from the DECTRIS measurement server. In Figure 83 a picture of the final adaption is shown.

6.3 Short-term stability tests

A method to test the stability of diffractometers has been proposed by *Dietrich* and has been further developed by *Fetisov* and *Markov*.^[148,154,155] The basic idea is that all instabilities of the diffractometer influence the peaks. While instabilities stemming from the stepper motors which drive the angles contribute most to the slope of the peaks, instabilities of the source and the detector contribute to each

point of the peak.^[154] The proposed method for checking the stability is to measure the peak profile for a number of strong reflections.

The original method was intended for point detectors. Since the examined detectors are area detectors the method was modified. A frame with a large number of reflections was chosen and then collected 100 to 500 times. To eliminate mechanical effects still images without any rotation were recorded. Additionally, for the DECTRIS PILATUS3 and the PHOTON 100 the shutterless measurement capabilities were used to further reduce mechanical instabilities. For the APEXII detector this was not possible due to the different hardware. However, through this procedure all instabilities that influence the peak intensities should be produced by either the detector or the source. All measurements have been done on 9,10-(Ph₂P=S)₂C₁₄H.^[156]

The measurements were performed on three different diffractometers. The test series for the DECTRIS PILATUS3 was conducted on a BRUKER D8 diffractometer equipped with a silver INCOATEC microfocus sealed tube with INCOATEC Quazar mirror optics. The measurements with the APEXII detector have been carried out on a BRUKER D8 diffractometer with a BRUKER molybdenum Turbo X-ray source (TXS) also equipped with INCOATEC mirror optics. Last, the data for the PHOTON 100 detector has been collected with the diffractometer of the workgroup of *Prof. Dr. S. Schneider*. The instrument is a BRUKER D8 diffractometer equipped with an INCOATEC molybdenum microfocus sealed tube with INCOATEC Quazar mirror optics.

To evaluate this large number of data a program was written in PYTHON to automatically calculate the raw peak intensity. The program first searches every frame for peaks and determines a rectangle that encloses it by using the OPEN SOURCE COMPUTER VISION PYTHON library and stores them. Then peaks at the same position are identified (using machine learning capabilities of the SCIKIT-LEARN PYTHON library) and the raw intensity of the peak is calculated by simply summing up the individual pixel values. From this the coefficient of variation

$$var(I) = \frac{\sigma(I)}{\langle I \rangle} \quad (18)$$

for the intensity I is calculated. For the DECTRIS PILATUS3 frames the API of the software ALBULA^[157] delivered by DECTRIS was used to read the frames while for the BRUKER frames an adapted version of the BRUKER100IMAGE and BRUKERIMAGE modules of the FABIO PACKAGE^[158].

6.4 Results

For the PILATUS3 detector measurements at several exposure times have been

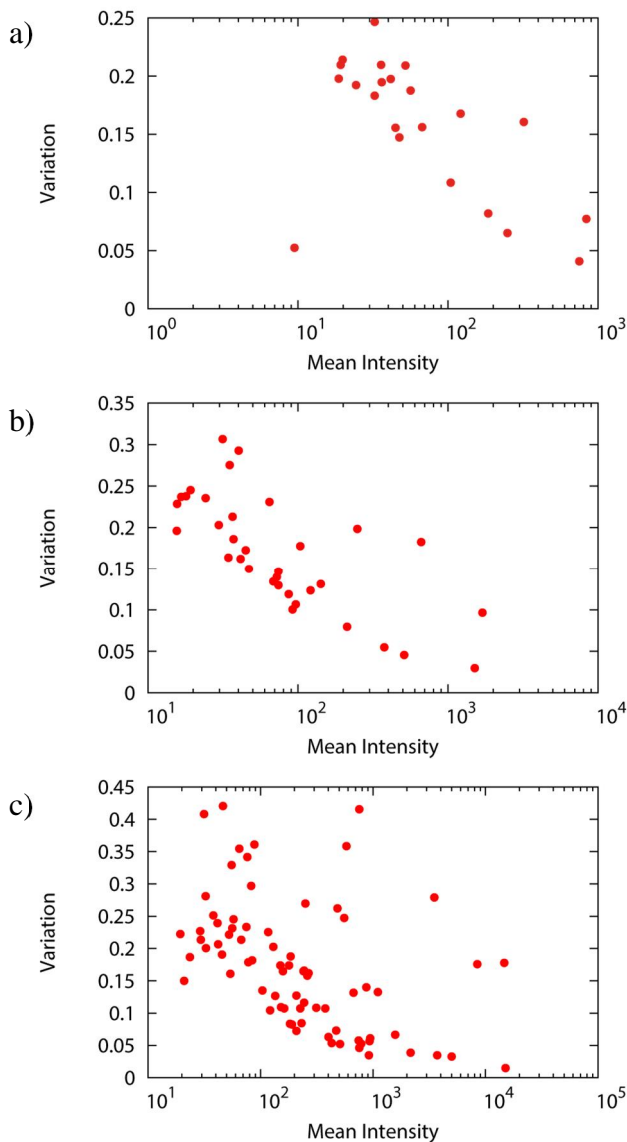


Figure 84: Half logarithmic plot of the variation of the peak intensity vs. the mean intensity for the DECTRIS PILATUS3 detector. a) 0.5 s exposure time b) 1 s exposure time c) 10 s exposure time.

carried out. For each exposure time 500 frames have been collected. The frames have been searched for reflections. Because of the fact that there has not been collected a full data set but only still frames indexed to get the respective *Miller* indices therefore the reflections will be identified by their X and Y coordinates on the frame. Obviously, the number of reflections found is depending on the exposure time. This means that especially at higher exposure times a large amount of reflections is found and therefore needs to be examined. To facilitate the evaluation the mean intensity for each reflection and the coefficient of variation have been calculated and plotted against each other. From this plot an overview of the intensity

distribution as well as the variation at the specific exposure time can be achieved. In Figure 84 a) for the 0.5 s exposure time plot the maximum variation is 24.68 % for a reflection of intensity in between 20 and 30 counts. Increasing the exposure time further increases the maximum variation up to 42 % for a reflection of mean intensity of 46 counts (Figure 84 b, c). For all plots the maxima in variation lie in a range of intensity between 10 and 100 counts. With increasing intensity, the variation lowers to under 5 %. In general it can be seen that the higher the variation decreases with increasing intensity. Reflections with intensities smaller than 1000 counts exhibit fairly high variations.

For further investigation a peak with low and high variation is chosen exemplarily. The reflection was chosen because its intensity rises with the increasing exposure time over two orders of magnitude. The reflection is located at the coordinates $X = 306$ and $Y = 356$. The right-hand side of Figure 83 shows the frame as it has been detected. The borders between the detecting modules as well as the beam stop are visible as dark blue lines. The small white areas are the detected signal. Blue areas indicate areas of no detected intensity. The left-hand side of the figure shows a plot of the calculated intensity for each of the collected frames. It can be seen that the highest intensity recorded for the reflection is 826 counts while the smallest is 659 counts. The coefficient of variation is calculated to 4.10 %. As

explained in the previous chapter the software automatically determines a rectangle,

Peak: (306, 356) Mean Intensity: 749.56 Variation Box Area: 10.92%

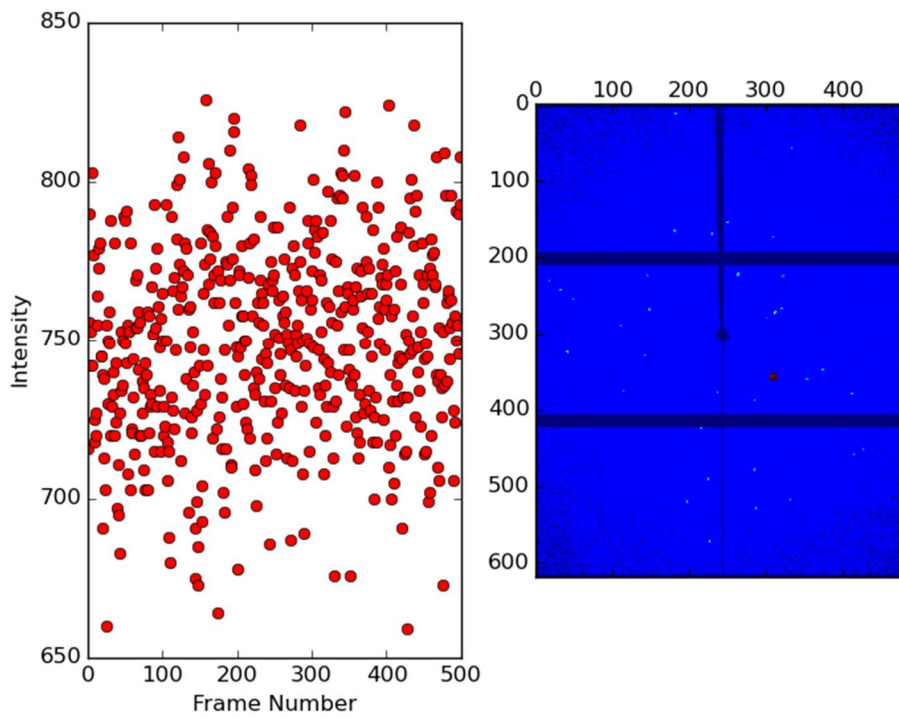


Figure 85: Plot of the intensity for the peak at the coordinates (306,356) vs the frame number (left) at 0.5 s of exposure time. Image of the frame with the position of the reflection marked in red (right).

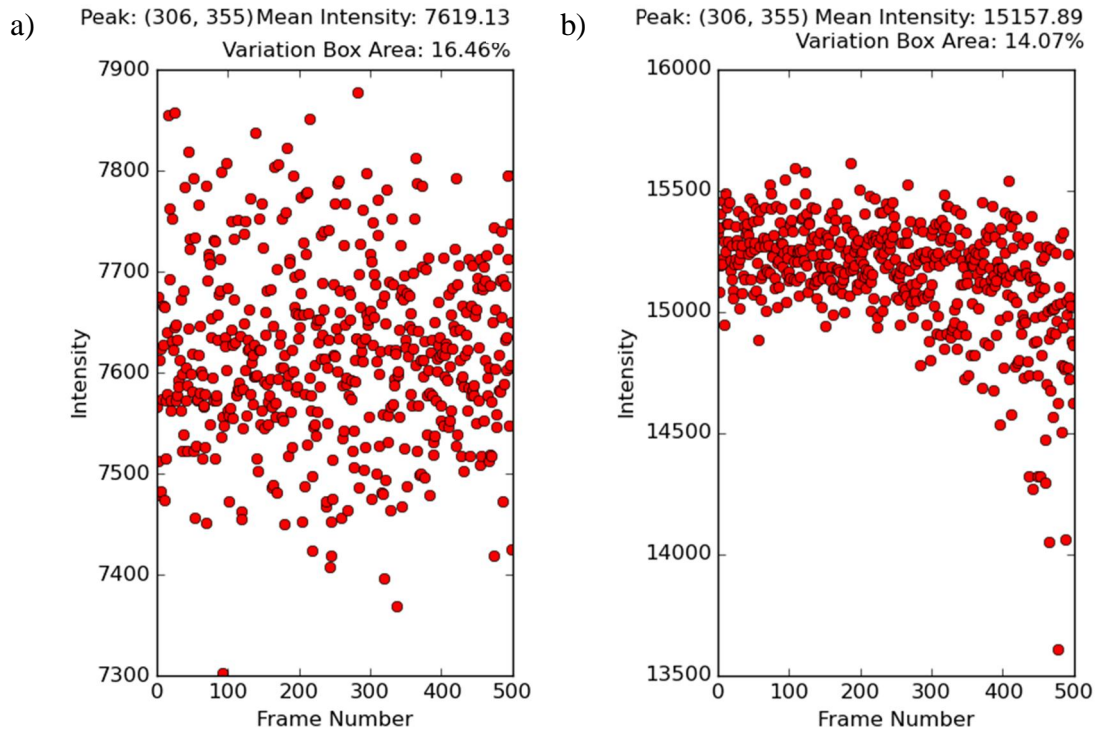


Figure 86: Plot of the intensity for the peak at the coordinates (306,356) vs the frame number a) at 5 s (coefficient of variation: 1.16 %) and b) 10 s of exposure time (coefficient of variation: 1.51 %).

which encloses the peak and then simply sums up the individual values. The variation in the size of this rectangle is also given in Figure 83 (10.92 %). For this reflection, this means that the box dimensions of the rectangle are either 4 by 4 or 5 by 4 pixels. It needs to be noted that no dependency of the intensity on the size of the rectangle could be found. Figure 86 shows the plots for the same reflection at the exposure times 5 s and 10 s. The calculated variation for the reflection are 1.16% for 5 s of exposure time and 1.51 % for 10 s of exposure time. Thus in general the variation decreases with increasing peak intensity. For the plot at exposure time of 10 s it is noticeable that towards the higher frame numbers (400 to 500) the absolute intensities drop. This leads to an increase in variation from 1.16 % to 1.51 %. This might be a consequence of the polarisation effect due to the constant photon flux mentioned in chapter 6.1.2.

Figure 86 shows the plot of the intensity versus the frame number for the reflection at frame coordinates $X = 92$ and $Y = 473$ pixels. This reflection shows a rather high coefficient of variation of 23.30 %. The mean intensity of the reflection is 75.35 counts which further supports assumption that low intensity reflections

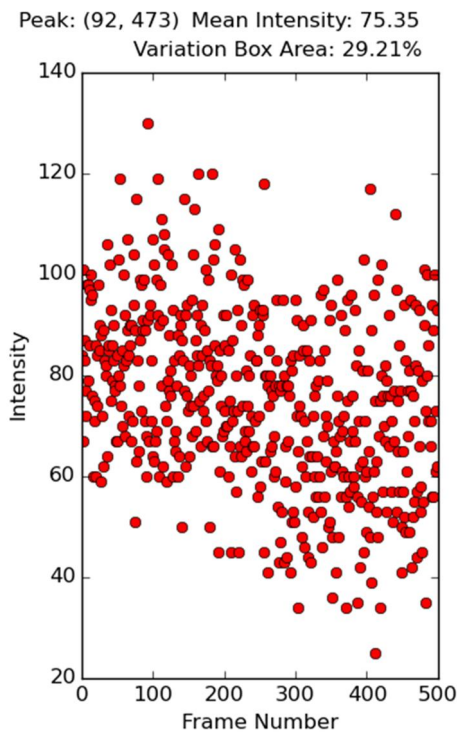


Figure 87: Plot of the intensity for the peak at the coordinates (92,473) vs the frame number at 10 s (coefficient of variation: 23.30 %).

exhibit high coefficients of variation. As for the previously discussed reflection, it might be argued that the variation in the area of the rectangle, which is used to determine the intensity, is high. However, also no dependency of the intensity on the rectangle size could be found.

The variation in intensity for the PHOTON 100 detector shows a similar trend. The higher the intensity, the lower the variation (Figure 88). It also has to be noticed that in this case the peak detection algorithm detected only peaks with intensities exceeding 10000 counts. The highest variation for this detector excluding the overloads is 7.87 %.

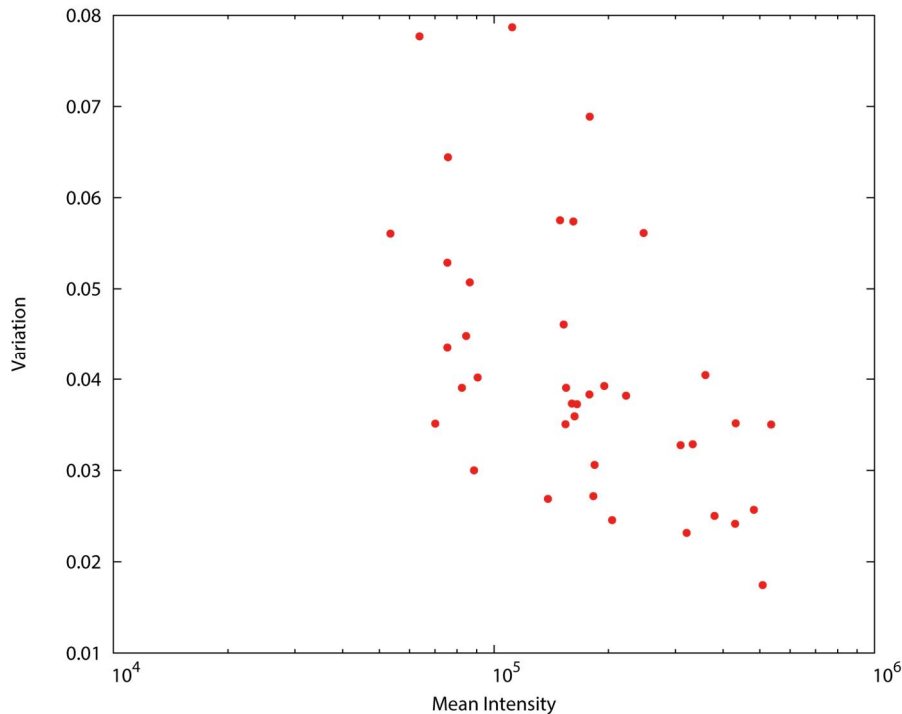


Figure 88: Half logarithmic plot of the variation of the peak intensity vs. the mean intensity for the BRUKER PHOTON 100 detector at an exposure time of 10 s.

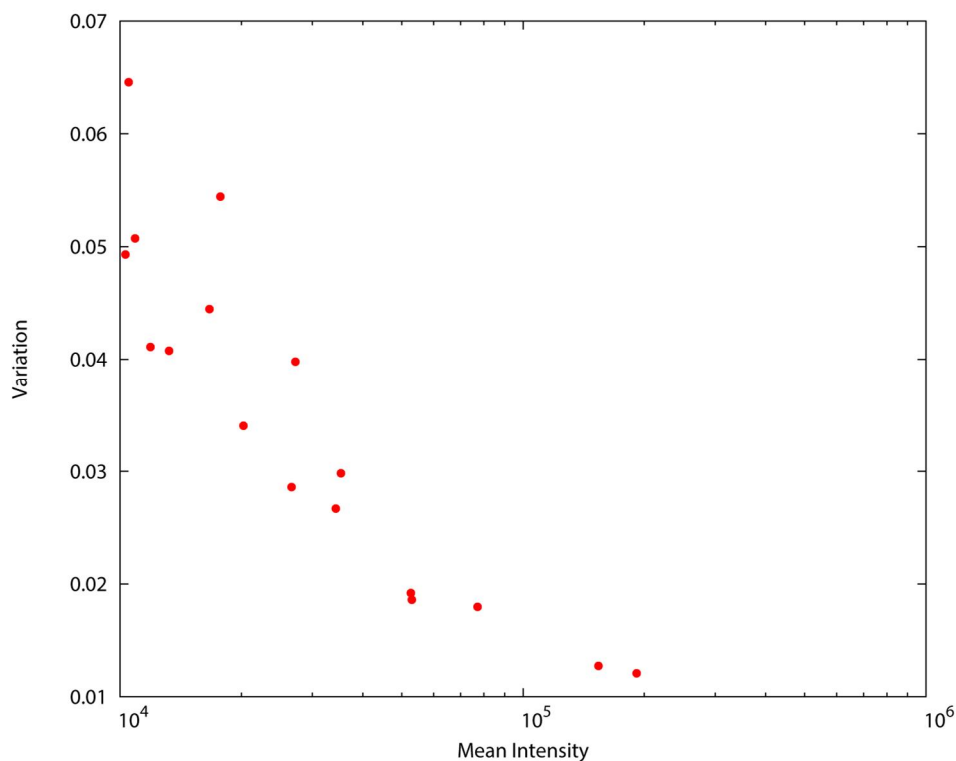


Figure 89: Half logarithmic plot of the variation of the peak intensity vs. the mean intensity for the BRUKER APEXII detector at an exposure time of 60 s.

For the last of the examined detectors, the APEXII, a similar pattern emerges. The variation decreases with increasing intensity (Figure 89). As seen before for the PHOTON 100 detector it is noticeable that the peak finding algorithm only finds peaks exceeding a certain intensity. In this particular case above 8000 counts. This is due to the fact that the APEXII as well as the PHOTON 100 exhibit, in contrast to the PILATUS3, a considerable level of background intensity.

6.5 Summary

When comparing the half logarithmic plots for all three detectors the most prominent difference is that the PILATUS3 seems to detect reflections over a wider range of intensities. However, this increase in the number of reflections comes at a price. Low intensity reflections (reflections with less than 100 counts) show variations of up to 50 %. This fact may be the consequence of the underlying working principles of the detectors. The design of the sensor features rather large pixel borders which are insensitive to X-ray photons (cf. Figure 80). All photons impinging on the border are not counted. The influence of one photon not counted

is of course bigger for low intensity reflections (< 100 counts). Something similar applies to the PHOTON 100 detector. Due to the large insensitive area some photons may not be detected. This effect is however minimised by using focusing lenses (Figure 78). Besides this it also has to be noted that the PILATUS3 practically does not have any noise. Therefore, reflections can be detected which will vanish in the noise of the APEXII and the PHOTON 100. Considering just the range of intensity which is present for all three detectors, all of them show variations below 10 %. The higher sensitivity of the DECTRIS PILATUS3 may not only be advantageous for home lab sources. On the one hand a higher number of reflections can be detected with a lower exposure time but on the other hand many of these reflections might have high standard uncertainties.

7 Evaluation of errors introduced to X-ray Data by the timing shutter

During data collections at the beamline 15-ID-B of the Advanced Photon Source (Argonne National Labs, Chicago, USA) several problems have been noticed. As stated by *Jakob Hey*, it is difficult to pinpoint one source of error. Besides the fact that the used APEXII CCD detector is not suitable for such an intense beam, our attention was drawn to the timing shutter as a potential source of error. Due to the very intense beam and the APEXII CCD detector, using exposure times in the range of 0.3 seconds is nothing unusual.

Jakob Hey already mentioned the connection between the synchronisation of the goniometer stepper motors and the timing shutter^[35]. He found out that the parameters OPENDELAY and CLOSEDELAY defined in the configuration file of the Bruker D8 Firmware are crucial to a precise measurement at such low exposure times.

Besides this source of error, the actual time the shutter is open could be subject to error at these exposure times. Due to the fact that the goniometer as well as the timing shutter used at BL 15-ID-B are stock Bruker products, a simple investigation could be carried out at one of our home diffractometers. To precisely measure the exposure time, a circuit using a LED and a phototransistor was designed in

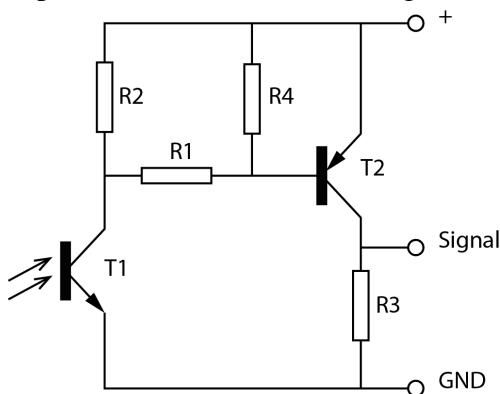


Figure 90: Circuit diagram of the detecting electronics. $R1 = 10 \text{ k}\Omega$, $R2 = 47 \text{ k}\Omega$, $R3 = 1 \text{ k}\Omega$, $R4 = 100 \text{ k}\Omega$, $T1 = \text{BPY62}$, $T2 = \text{BC557}$.

cooperation with the electronics workshop (cf. Figure 90). The phototransistor was placed at the one end of the Timing shutter while the LED was placed on the other. To tightly fit the parts to the diffractometer and shield the detecting circuit from stray light, special casings for the phototransistor and the LED were machined. By opening the timing shutter

the phototransistor gets illuminated and a signal can be detected. The signals were recorded by a Vellemann 4-channel USB-Datalogger. The frequency of the data

logger was 100 Hz, making it possible to examine shutter fluctuations of up to 0.01 s. At an exposure time of 0.3 s this translates to 3.33% error. Measurements were done at 1, 0.5 and 0.3 s of shutter opening time.

7.1 Results

Figure 91 shows square-wave signals, as detected in the measurements, for each exposure time. It can be seen that there is virtually no continuous rising of the signal. Therefore, only the high signal will be regarded as the opening time of the shutter. A program has been written in PYTHON to efficiently analyse the measured data. The program first determines the positions of the signals and then calculates the difference of the end and starting time of the signal. After

this, the mean and the standard deviation are

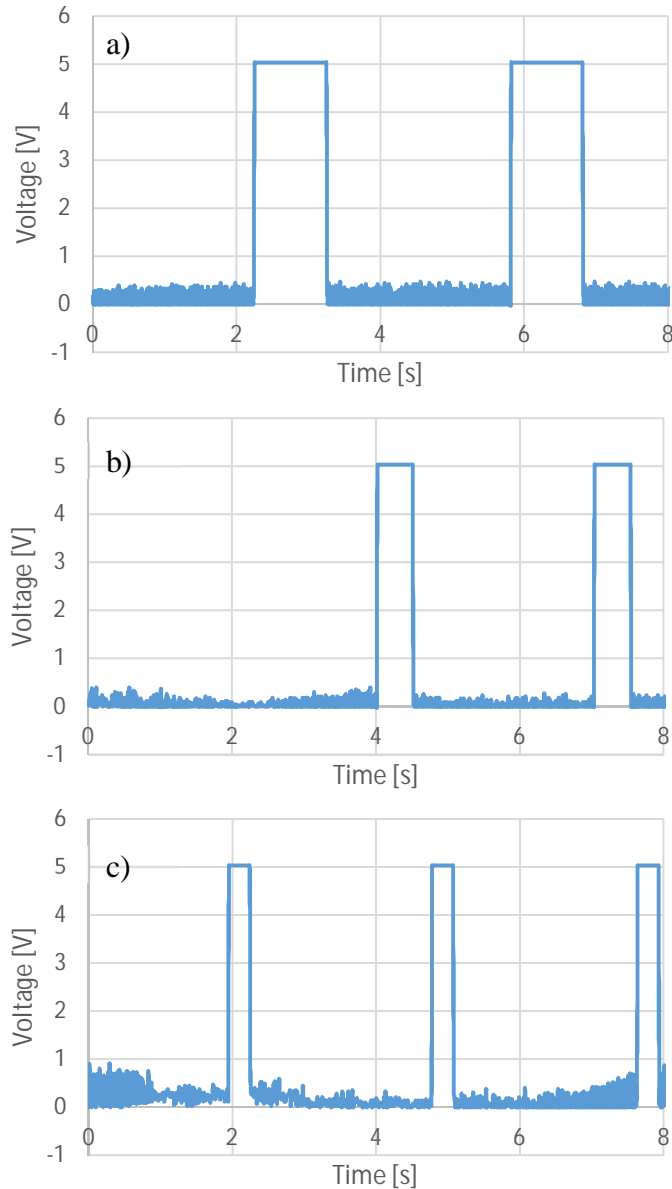


Figure 91: Square-wave signal as for a) 1 s, b) 0.5 s and c) 0.3 s of shutter opening time.

Table 23: Overview of the requested and mean shutter opening time and the standard deviation.

Requested exposure time [s]	Mean shutter opening time [s]	Standard deviation [s]
0.3	0.291	0.004
0.5	0.492	0.005
1.0	0.992	0.006

calculated from a number of 1000 measurements. The results of this calculation are summarised in Table 23. It can be seen that the mean shutter opening time is about 0.01 s shorter for all requested exposure times. The standard deviations are in a range from 0.004 to 0.006 s. Within the boundaries of the experimental setup this indicates that there is a small error introduced by the mechanical shutter.

7.2 Conclusion

In conclusion, a simple device for measuring the shutter opening time could be built. With the help of the USB data logger the exposure times could be measured with a sampling frequency of 100 Hz or 0.01 s. By using a large number of measurements, a rough guess of the accuracy of the mechanical shutter could be obtained. The actual mean shutter opening times vary statistically by about 0.01 s from the requested exposure times. For further testing, it would be advantageous to use data loggers with higher sampling rates to more accurately determine the error introduced by the mechanical shutter. For the lowest exposure time tested, the deviation of 0.01 s equals to an error of 3.33 %. However, this extremely low exposure time is not used very often but with the further development of more and more powerful X-ray sources they might be necessary to avoid overloading the detector. The most efficient way to eliminate all errors introduced by mechanical shutters is simply removing them. Recent detectors are capable of shutterless operation. However, it needs to be proven that shutterless data acquisition is suitable for measurements used in charge density investigations, as these do need extremely high data quality.

8 Data collection at SPring-8 BL02B1

In July 2016 it was possible to obtain 24 hours of beam time at the beam line BL02B at the SPring-8 synchrotron facility in Japan in cooperation with the workgroup of *Bo Brummerstedt Iversen* from Aarhus University. The SPring-8 synchrotron is a third generation and the currently most powerful synchrotron radiation source. The beam line BL02B1 offers conditions especially suited for single crystal routine and charge density

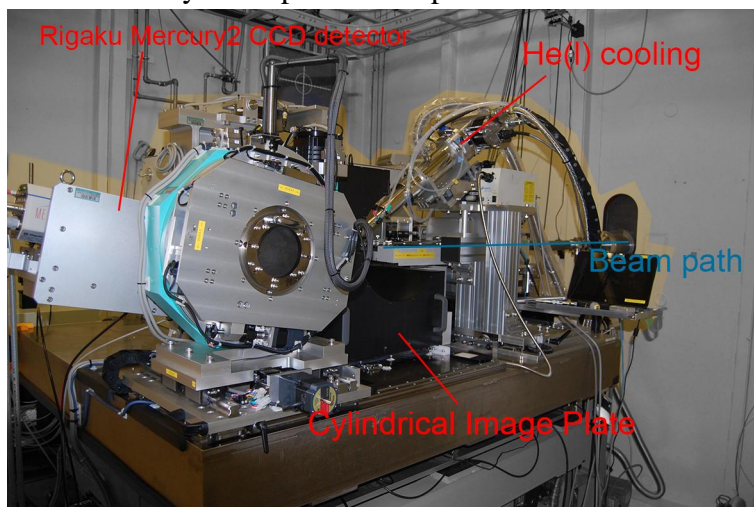


Figure 92: Setup at beam line BL02B1 at the Spring-8 synchrotron radiation facility, Japan.

studies. BL02B1 is equipped with two switchable detectors, a four circle goniometer and an open flow liquid helium cooling (Figure 92). For fast investigation of the crystal quality and routine structure determination, a RIGAKU MERCURY2 CCD detector can be used. For the measurement of high resolution charge density data sets, the also present custom RIGAKU cylindrical image plate detector is used. The image plate does cover a 2θ range from -60° to 145° , which makes it possible to obtain high resolution raw images in one shot. The superior dynamic range of the image plate is suitable to cope with the high intensity low angle reflections as well as weak reflections at high angles at the same time. However, these advantages come at a price: the readout time. Due to the readout process, the dead time between two images is approximately seven minutes. Therefore, measurements take more time than at comparable synchrotron sources or beam lines (e.g. Advanced Photon Source, Argonne National Labs,

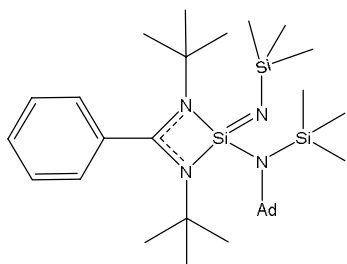


Figure 93: Schlenck line installed at BL02B1, Spring-8, Japan.

Chicago, USA). In addition, the laboratory at BL02B1 was upgraded to simplify handling of air sensitive samples (Figure 93).

8.1 Experimental measurements

A total of eight samples had been brought. However, due to limited time only two samples could be investigated. The first sample was the silylene shown in

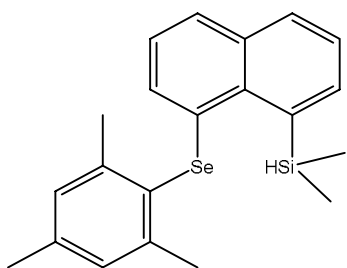


Scheme 7: Structure of the investigated silylene (**3**).

Scheme 7.^[159] The electronic structure of this compound is especially interesting because of the formally hypervalent silicon. Charge density has proven to be a tool best suited for tackling the concept of hypervalency.^[86]

A crystal of **3**, suitable for single crystal X-ray diffraction, was chosen under the microscope and glued to a glass fibre mounted at the tip of the goniometer head. The sample was mounted in the helium gas stream at 300 K and then cooled to 20 K. For cell and orientation determination, the CCD detector was used. The data collection strategy was determined with the program STRATEGY_VER3.0.EXE. The detector has been switched to the image plate for measurement. During data collection, frequent checking of the data quality was done by integrating and processing the data. While checking the data, it was noticed that the scale of the data was decreasing. This may be an indicator of crystal decay. It was therefore decided to recollect the first frame and compare this to the original frame. By integrating both frames and monitor the scale factor (original frame: 1.04, recollected frame: 0.95), it could be confirmed that there is a drop in intensity. This was indicative that the crystal was decaying.

Several other suitable crystals of compound **3** were chosen, but all samples showed a similar behaviour as described above. As this is a highly air sensitive



Scheme 8: Structure of compound **4**.

sample, it was decided to abandon it and move to the air stable compound **4** (Scheme 8).

A crystal of compound **4**, suitable for single crystal X-ray diffraction, had been selected and was glued to a glass fibre mounted to a goniometer head. The sample was mounted to the

goniometer with the helium gas stream set to 300 K. Several frames were taken with the CCD detector to check the crystal quality. As the results seemed promising, the detector was switched to the image plate and the sample was cooled to 20 K with a rate of 50 K per minute. The first image taken with the image plate detector showed that during cooling the crystals broke. This was at first attributed to the fast cooling rate. However, tests with slower cooling rates showed that all the crystals broke when cooling to temperatures below 60 K. This might be indicative to a phase transition. Therefore, further measurements were done at a temperature of 100 K. Another suitable crystal was chosen and mounted as explained above. The crystal quality was investigated using the CCD detector and after confirmation, the detector was changed to the image plate. During cooling a measurement strategy was calculated with the program STRATEGY_VER3.0.EXE. As for the other sample, frequent checking of the data quality was done. After having taken several images, it was noticed that also for this sample the scale was decreasing. To check for crystal decay, the angle settings of the first image were adjusted and the image was recollected. The sample also showed severe decay. This was confirmed by an additional attempt with another crystal of compound **4** which showed the same behaviour.

8.2 Conclusion

Despite the unique experimental setup with one of the brightest X-ray sources worldwide, no usable data set could be obtained. This is, on the one hand, due to the limited amount of time granted, and on the other hand, due to the radiation damage which was more severe than expected. It is unlikely that the radiation damage was only severe on the samples described within this thesis. The samples containing organic or metal organic compounds, which had been brought by the members of *Bo Iversens* group, showed a similar amount of decay even when attenuating the beam to an intensity of about 40 %. The samples with the best results obtained during this beam time were rather simple compounds like pyrite and CoSi_2 . One of the reasons that organometallic compounds could not be measured, is the long measurement time which is mostly due to the dead time of about seven minutes. Within these seven minutes, no frame is taken but secondary radiation damage can spread. This observation is in agreement with the better data obtained

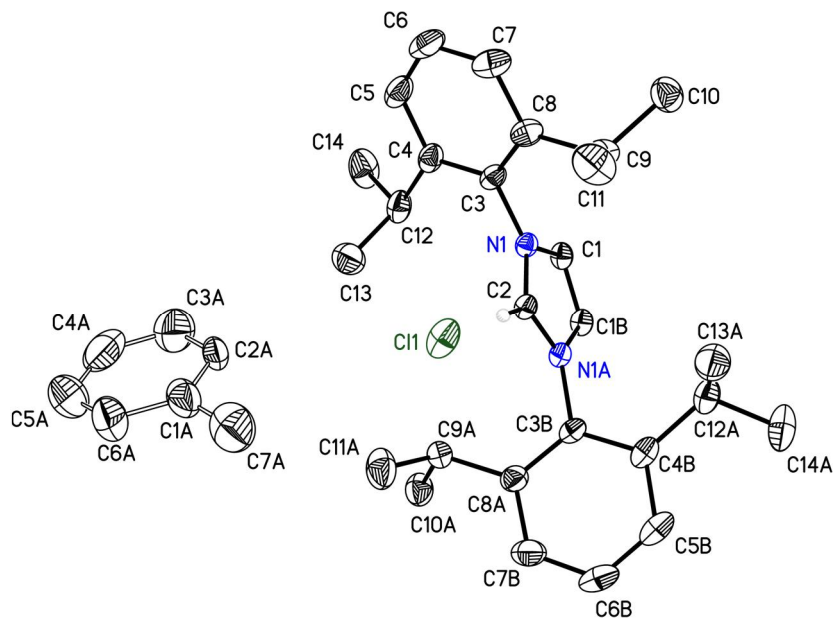
for pyrite and CoSi_2 as these are less sensitive to radiation damage. To overcome this disadvantageous seven minutes of dead time, it would be advisable to exchange the CCD detector with a detector suitable for synchrotron application. With the new generations of detectors capable of shutterless operation mode, shorter measurement times for compounds which are prone to radiation damage could be achieved.

9 Single Crystal Structures Determination

9.1 Collaboration with Dr. Rajendra Ghadwal

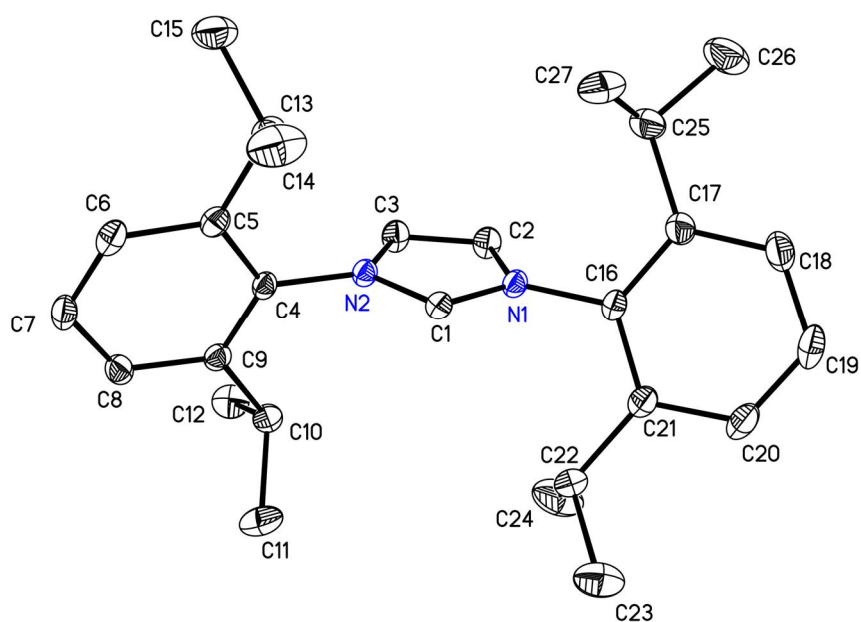
9.1.1 Unpublished Structures

9.1.1.1 FE_Raj_71



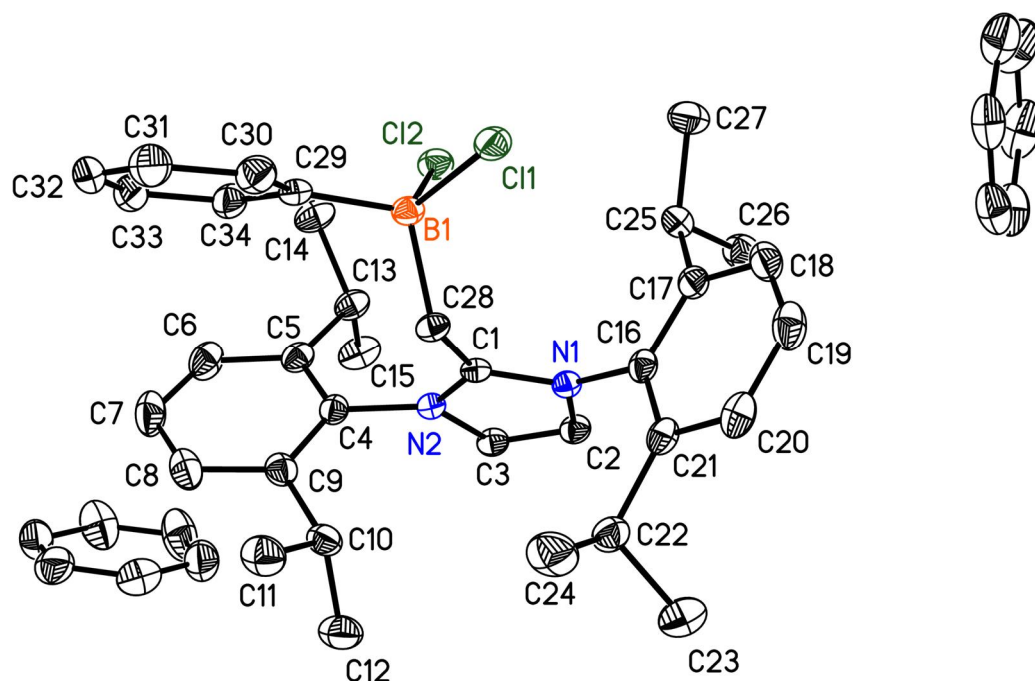
Identification code	FE_Raj_71	F(000)	1110
Empirical formula	C _{33.65} H _{44.60} ClN ₂	Crystal size	0.100 x 0.100 x 0.100 mm
Formula weight	512.56	θ range for data collection	1.999 to 27.877°.
Temperature	100(2) K	Index ranges	-30<=h<=29, -11<=k<=11, -22<=l<=22
Wavelength	0.71073 Å	Reflections collected	61512
Crystal system	Monoclinic	Independent reflections	3605 [R(int) = 0.0287]
Space group	C2/c	Completeness to θ = 25.242°	100.00%
Unit cell dimensions	a = 22.812(1) Å b = 8.761(1) Å c = 16.965(1) Å β = 116.74(2)°	Absorption correction	Semi-empirical from equivalents
Volume	3028.0(6) Å ³	Max. and min. transmission	0.7456 and 0.7159
Z	4	Refinement method	Full-matrix least-squares on F ²
Density (calculated)	1.124 Mg/m ³	Data / restraints / parameters	3605 / 382 / 222
Absorption coefficient	0.150 mm ⁻¹	Goodness-of-fit on F ²	1.073
		Final R indices [I>2σ(I)]	R1 = 0.0450, wR2 = 0.1172
		R indices (all data)	R1 = 0.0527, wR2 = 0.1232
		Largest diff. peak and hole	0.362 and -0.246 eÅ ⁻³

9.1.1.2 FE_Raj_103



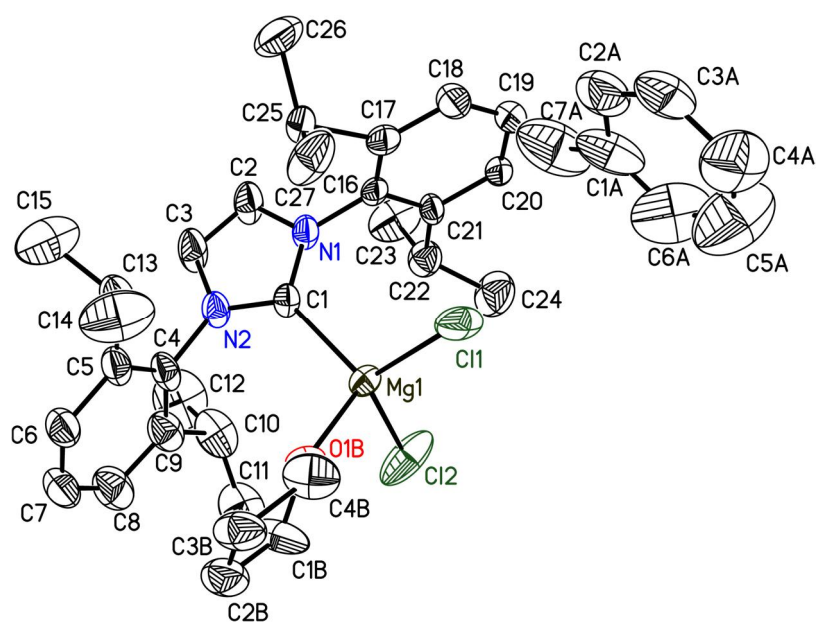
Identification code	FE_Raj_103	F(000)	848
Empirical formula	C ₂₇ H ₃₆ N ₂	Crystal size	0.200 x 0.200 x 0.100 mm
Formula weight	388.58	θ range for data collection	1.961 to 28.709°
Temperature	101(2) K	Index ranges	-26<=h<=28, -7<=k<=7, -26<=l<=25
Wavelength	0.71073 Å	Reflections collected	82531
Crystal system	Monoclinic	Independent reflections	6111 [R(int) = 0.0223]
Space group	<i>P</i> ₂ /c	Completeness to θ = 25.242°	100.00%
Unit cell dimensions	a = 20.788(1) Å b = 5.775(2) Å c = 19.723(1) Å β = 92.41(2)°	Absorption correction	Semi-empirical from equivalents
		Max. and min. transmission	0.7458 and 0.7017
		Refinement method	Full-matrix least-squares on F ²
Volume	2365.5(1) Å ³	Data / restraints / parameters	6111 / 589 / 287
Z	4	Goodness-of-fit on F ²	1.029
Density (calculated)	1.091 Mg/m ³	Final R indices [I > 2σ(I)]	R1 = 0.0450, wR2 = 0.1162
Absorption coefficient	0.063 mm ⁻¹	R indices (all data)	R1 = 0.0523, wR2 = 0.1220
		Largest diff. peak and hole	0.409 and -0.304 eÅ ⁻³

9.1.1.3 FE_Raj_250



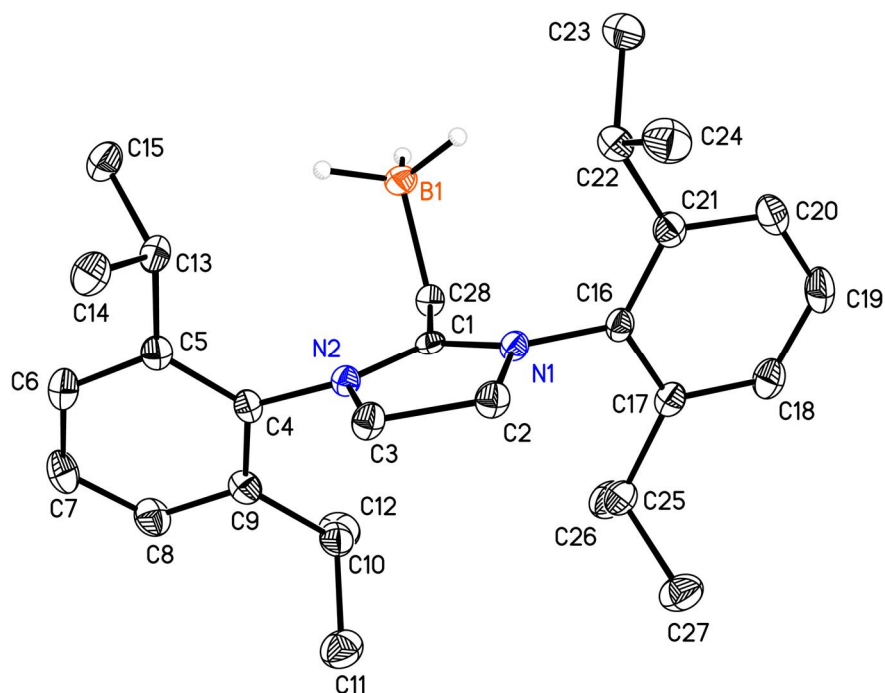
Identification code	FE_Raj_250	F(000)	1536
Empirical formula	C ₄₆ H ₅₅ BCl ₂ N ₂	Crystal size	0.200 x 0.200 x 0.100 mm
Formula weight	717.63	θ range for data collection	3.723 to 70.239°
Temperature	100(2) K	Index ranges	-17<=h<=18, -20<=k<=19, -20<=l<=20
Wavelength	1.54178 Å	Reflections collected	66927
Crystal system	Monoclinic	Independent reflections	7903 [R(int) = 0.0227]
Space group	<i>P</i> ₂ ₁ / <i>n</i>	Completeness to θ = 25.242°	99.90%
Unit cell dimensions	a = 14.772(2) Å b = 16.583(2) Å c = 17.080(2) Å β = 95.40(1)°	Absorption correction	Semi-empirical from equivalents
Volume	4165.4(9) Å ³	Max. and min. transmission	0.7533 and 0.7085
Z	4	Refinement method	Full-matrix least-squares on F ²
Density (calculated)	1.144 Mg/m ³	Data / restraints / parameters	7903 / 0 / 468
Absorption coefficient	1.636 mm ⁻¹	Goodness-of-fit on F ²	1.043
		Final R indices [I > 2σ(I)]	R1 = 0.0319, wR2 = 0.0867
		R indices (all data)	R1 = 0.0335, wR2 = 0.0882
		Largest diff. peak and hole	0.334 and -0.231 eÅ ⁻³

9.1.1.4 FE_Raj_132



Identification code	FE_Raj_132	Crystal size	0.200 x 0.200 x 0.100 mm ³
Empirical formula	C ₃₈ H ₅₂ Al ₁₀ Cl ₂ Mg N ₂ O	θ range for data collection	1.689 to 25.368°
Formula weight	648.02	Index ranges	-15 ≤ h ≤ 15, -19 ≤ k ≤ 19, -21 ≤ l ≤ 21
Temperature	100(2) K	Reflections collected	25844
Wavelength	0.71073 Å	Independent reflections	6883 [R(int) = 0.0447]
Crystal system	Orthorhombic	Completeness to θ = 25.242°	99.90%
Space group	<i>P</i> 2 ₁ 2 ₁ 2 ₁	Absorption correction	Semi-empirical from equivalents
Unit cell dimensions	a = 12.810(2) Å b = 16.104(2) Å c = 18.186(2) Å	Max. and min. transmission	0.7452 and 0.6887
Volume	3751.6(9) Å ³	Refinement method	Full-matrix least-squares on F ²
Z	4	Data / restraints / parameters	6883 / 1424 / 557
Density (calculated)	1.147 Mg/m ³	Goodness-of-fit on F ²	1.057
Absorption coefficient	0.220 mm ⁻¹	Final R indices [I > 2σ(I)]	R ₁ = 0.0531, wR ₂ = 0.1331
F(000)	1392	R indices (all data)	R ₁ = 0.0576, wR ₂ = 0.1364
		Absolute structure parameter	0.09(3)
		Largest diff. peak and hole	0.478 and -0.496 eÅ ⁻³

9.1.1.5 FE_Raj_243



Identification code	FE_Raj_243	Absorption coefficient	0.062 mm ⁻¹
Empirical formula	C ₂₈ H ₄₃ B N ₂	F(000)	920
Formula weight	418.45	Crystal size	0.200 x 0.200 x 0.100 mm ³
Temperature	100(2) K	θ range for data collection	1.775 to 26.035°
Wavelength	0.71073 Å	Index ranges	-14<=h<=13, -19<=k<=19, -17<=l<=17
Crystal system	Monoclinic	Reflections collected	23115
Space group	<i>P</i> ₂ ₁ / <i>c</i>	Independent reflections	5061 [R(int) = 0.0356]
Unit cell dimensions	a = 11.625(3) Å	Completeness to θ = 25.242°	99.90%
	b = 15.935(4) Å	Absorption correction	Semi-empirical from equivalents
	c = 14.033(3) Å	Max. and min. transmission	0.7453 and 0.7058
	α = 90°	Refinement method	Full-matrix least-squares on F ²
	β = 99.19(2)°	Data / restraints / parameters	5061 / 522 / 297
	γ = 90°	Goodness-of-fit on F ²	1.125
Volume	2566.2(11) Å ³	Final R indices [I > 2σ(I)]	R1 = 0.0422, wR2 = 0.1070
Z	4	R indices (all data)	R1 = 0.0554, wR2 = 0.1132
Density (calculated)	1.083 Mg/m ³	Largest diff. peak and hole	0.225 and -0.202 e.Å ⁻³

References

- [1] W. Friedrich, P. Knipping, M. v. Laue, *Sitzungsberichte der kaiserlich Akademischen Wissenschaften München* **1912**, 303–322.
- [2] A. W. Hull., *Phys. Rev.* **1917**, *10*, 661–696.
- [3] P. Debye, P. Scherrer, *Nachr. K. Ges. Wiss. Göttingen Math. Physik. Kl.*, 1–26.
- [4] W. H. Bragg, *Proc. R. Soc. A* **1913**, *89*, 246–248.
- [5] W. H. Bragg, W. L. Bragg, *Proc. R. Soc. A* **1913**, *88*, 428–438.
- [6] W. L. Bragg, *Proc. R. Soc. A* **1913**, *89*, 248–277.
- [7] N. K. Hansen, P. Coppens, *Acta Cryst. A* **1978**, *34*, 909–921.
- [8] D. Jayatilaka, B. Dittrich, *Acta Cryst. A* **2008**, *64*, 383–393.
- [9] P. Coppens, *X-ray charge densities and chemical bonding*, International Union of Crystallography, Chester, England, Oxford, New York, **1997**.
- [10] R. F. Stewart, *Chem. Phys. Lett.* **1979**, *65*, 335–342.
- [11] R. F. Stewart, *J. Chem. Phys.* **1973**, *58*, 1668.
- [12] R. F. Stewart, *J. Chem. Phys.* **1969**, *51*, 4569.
- [13] R. F. Stewart, *J. Chem. Phys.* **1968**, *48*, 4882.
- [14] T. Schulz, K. Meindl, D. Leusser, D. Stern, J. Graf, C. Michaelsen, M. Ruf, G. M. Sheldrick, D. Stalke, *J. Appl. Crystallogr.* **2009**, *42*, 885–891.
- [15] P. Macchi, H.-B. Bürgi, A. S. Chimpri, J. Hauser, Z. Gál, *J. Appl. Crystallogr.* **2011**, *44*, 763–771.
- [16] L. Krause, R. Herbst-Irmer, G. M. Sheldrick, D. Stalke, *J. Appl. Crystallogr.* **2015**, *48*, 3–10.
- [17] J. Graf, H. Ott, A. Kleine, C. Michaelsen, *High-Brightness Microfocus Sources for Chemical Crystallography. Bright.Brighter.Unique.*, **2016**.
- [18] L. Krause, R. Herbst-Irmer, D. Stalke, *J. Appl. Crystallogr.* **2015**, *48*, 1907–1913.
- [19] K. Kirschbaum, A. Martin, A. A. Pinkerton, *J. Appl. Crystallogr.* **1997**, *30*, 514–516.
- [20] C. Giacovazzo (Ed.) *IUCr texts on crystallography, Vol. 15*, Oxford Univ. Press, Oxford, **2011**.

- [21] M. S. Weiss, *J. Appl. Crystallogr.* **2001**, *34*, 130–135.
- [22] K. Diederichs, *Acta Cryst. D* **2010**, *66*, 733–740.
- [23] P. A. Karplus, K. Diederichs, *Science* **2012**, *336*, 1030–1033.
- [24] A. T. Brünger in *Methods in Enzymology*, Vol. 277 (Ed.: C. W. Carter), Acad. Press, San Diego, Calif., **1997**.
- [25] B. Zarychta, J. Zaleski, J. Kyzioł, Z. Daszkiewicz, C. Jelsch, *Acta Cryst. B* **2011**, *67*, 250–262.
- [26] A. T. Brünger **1992**, *355*, 472–475.
- [27] A. Paul, M. Kubicki, C. Jelsch, P. Durand, C. Lecomte, *Acta Cryst. B* **2011**, *67*, 365–378.
- [28] C. Jelsch, B. Guillot, A. Lagoutte, C. Lecomte, *J. Appl. Crystallogr.* **2005**, *38*, 38–54.
- [29] A. Volkov, P. Macchi, L. J. Farrugia, C. Gatti, P. Mallinson, T. Richter, T. Koritsanszky, *XD2006 - A computer program for multipole refinement topological analysis of charge densities and evaluation of intermolecular interaction energies from experimental or theoretical structure factors.*, **2006**.
- [30] L. Krause, R. Herbst-Irmer, D. Stalke, *submitted*.
- [31] K. Meindl, J. Henn, *Acta Cryst. A* **2008**, *64*, 404–418.
- [32] B. Niepötter, R. Herbst-Irmer, D. Stalke, *J. Appl. Crystallogr.* **2015**, *48*, 1485–1497.
- [33] V. V. Zhurov, E. A. Zhurova, A. A. Pinkerton, *J. Appl. Crystallogr.* **2008**, *41*, 340–349.
- [34] H. Wolf, M. R. V. Jorgensen, Y.-S. Chen, R. Herbst-Irmer, D. Stalke, *Acta Cryst. B* **2015**, *71*, 10–19.
- [35] J. Hey, *Dissertationsschrift*, Georg-August-Universität, Göttingen, **2013**.
- [36] A. Stash, *DRKplot for XD and SHELX*, **2007**.
- [37] S. C. Abrahams, E. T. Keve, *Acta Cryst. A* **1971**, *27*, 157–165.
- [38] R. F. W. Bader, *Atoms in molecules. A quantum theory*, Clarendon Press, Oxford, **2003**.
- [39] R. F. W. Bader, T. H. Tang, Y. Tal, F. W. Biegler-Koenig, *J. Am. Chem. Soc.* **1982**, *104*, 946–952.
- [40] R. F. W. Bader, *Acc. Chem. Res.* **1975**, *8*, 34–40.

-
- [41] R. F. W. Bader, T. H. Tang, Y. Tal, F. W. Biegler-Koenig, *J. Am. Chem. Soc.* **1982**, *104*, 940–945.
- [42] R. F. W. Bader, H. Essén, *J. Chem. Phys.* **1984**, *80*, 1943.
- [43] L. J. Kershaw Cook, R. Mohammed, G. Sherborne, T. D. Roberts, S. Alvarez, M. A. Halcrow, *Coord. Chem. Rev.* **2015**, *289-290*, 2–12.
- [44] J. Contreras-Garcia, W. Yang, E. R. Johnson, *J. Phys. Chem. A* **2011**, *115*, 12983–12990.
- [45] E. R. Johnson, S. Keinan, P. Mori-Sanchez, J. Contreras-Garcia, A. J. Cohen, W. Yang, *J. Am. Chem. Soc.* **2010**, *132*, 6498–6506.
- [46] P. J. Cox, N. S. Simpkins, *Tetrahedron: Asymmetry* **1991**, *2*, 1–26.
- [47] N. S. Simpkins, *Pure Appl. Chem.* **1996**, *68*.
- [48] D. R. Armstrong, D. Barr, W. Clegg, S. M. Hodgson, R. E. Mulvey, D. Reed, R. Snaith, D. S. Wright, *J. Am. Chem. Soc.* **1989**, *111*, 4719–4727.
- [49] R. E. Mulvey, *Chem. Soc. Rev.* **1998**, *27*, 339.
- [50] E. Weiss, *Angew. Chem.* **1993**, *105*, 1565–1587.
- [51] R. v. Bülow, H. Gornitzka, T. Kottke, D. Stalke, *Chem. Commun.* **1996**, 1639.
- [52] K. Gregory, P. von Ragué Schleyer, R. Snaith in *Advances in Inorganic Chemistry* (Ed.: A. G. Sykes), Elsevier textbooks, s.l., **1991**.
- [53] C. R. Groom, I. J. Bruno, M. P. Lightfoot, S. C. Ward, *Acta Cryst. B* **2016**, *72*, 171–179.
- [54] N. P. Funnell, A. Dawson, W. G. Marshall, S. Parsons, *CrystEngComm* **2013**, *15*, 1047–1060.
- [55] J. B. Collins, A. Streitwieser, *J. Comput. Chem.* **1980**, *1*, 81–87.
- [56] A. L. Hinde, A. Pross, L. Radom, *J. Comput. Chem.* **1980**, *1*, 118–128.
- [57] J. D. Dill, P. v. R. Schleyer, J. S. Binkley, J. A. Pople, *J. Am. Chem. Soc.* **1977**, *99*, 6159–6173.
- [58] A. Hinchliffe, J. Charles Dobson, *Theoret. Chim. Acta* **1975**, *39*, 17–24.
- [59] A. Hinchliffe, *Chem. Phys. Lett.* **1977**, *45*, 88–91.
- [60] E. U. Wuerthwein, K. D. Sen, J. A. Pople, P. v. R. Schleyer, *Inorg. Chem.* **1983**, *22*, 496–503.
- [61] A. E. Reed, R. B. Weinstock, F. Weinhold, *J. Chem. Phys.* **1985**, *83*, 735.

- [62] C. Fressigné, J. Maddaluno, C. Giessner-Prettre, B. Silvi, *J. Org. Chem.* **2001**, *66*, 6476–6479.
- [63] A. D. Becke, K. E. Edgecombe, *J. Chem. Phys.* **1990**, *92*, 5397.
- [64] P.-C. Kuo, J.-C. Chang, W.-Y. Lee, H. M. Lee, J.-H. Huang, *J. Organomet. Chem.* **2005**, *690*, 4168–4174.
- [65] T. Kottke, D. Stalke, *J. Appl. Crystallogr.* **1993**, *26*, 615–619.
- [66] D. Stalke, *Chem. Soc. Rev.* **1998**, *27*, 171.
- [67] *COSMO*, Bruker-AXS, Madison(WI), USA, **2011**.
- [68] *APEX2 Suite* 2013.4-1, Bruker-AXS, Madison (WI), USA, **2013**.
- [69] *SAINT* v8.30C, Bruker-AXS, Madison(WI), USA, **2013**.
- [70] G. M. Sheldrick, *XPREP* 2015/1, Madison (WI), USA, **2015**.
- [71] G. M. Sheldrick, *Acta Cryst. A* **2015**, *71*, 3–8.
- [72] G. M. Sheldrick, *Acta Cryst. C* **2015**, *71*, 3–8.
- [73] R. M. Badger, *J. Chem. Phys.* **1935**, *3*, 710.
- [74] R. M. Badger, *J. Chem. Phys.* **1934**, *2*, 128.
- [75] M. Kaupp, B. Metz, H. Stoll, *Angew. Chem.* **2000**, *112*, 4780–4782.
- [76] M. Kaupp, S. Riedel, *Inorg. Chim. Acta* **2004**, *357*, 1865–1872.
- [77] E. Kraka, D. Setiawan, D. Cremer, *J. Comput. Chem.* **2016**, *37*, 130–142.
- [78] M. Hermann, G. Frenking, *Chem. - Eur. J.* **2016**, *22*, 4100–4108.
- [79] F. H. Allen, I. J. Bruno, *Acta Cryst. B* **2010**, *66*, 380–386.
- [80] A. Volkov, Y. A. Abramov, P. Coppens, *Acta Cryst. A* **2001**, *57*, 272–282.
- [81] H. Ott, U. Pieper, D. Leusser, U. Flierler, J. Henn, D. Stalke, *Angewandte Chemie (International ed. in English)* **2009**, *48*, 2978–2982.
- [82] H. Ott, U. Pieper, D. Leusser, U. Flierler, J. Henn, D. Stalke, *Angew. Chem.* **2009**, *121*, 3022–3026.
- [83] H. Ott, C. Daschlein, D. Leusser, D. Schildbach, T. Seibel, D. Stalke, C. Strohmann, *J. Am. Chem. Soc.* **2008**, *130*, 11901–11911.
- [84] F. Engelhardt, *Diplomarbeit*, Georg-August-Universität, Göttingen, **2012**.
- [85] I. Objartel, D. Leusser, F. Engelhardt, R. Herbst-Irmer, D. Stalke, *Z. anorg. allg. Chem.* **2013**, *639*, 2005–2012.
- [86] M. S. Schmokel, S. Cenedese, J. Overgaard, M. R. V. Jorgensen, Y.-S. Chen, C. Gatti, D. Stalke, B. B. Iversen, *Inorg. Chem.* **2012**, *51*, 8607–8616.

-
- [87] P. Macchi, P. Coppens, *Acta Cryst. A* **2001**, *57*, 656–662.
- [88] J. Luebben, T. Gruene, *Proc. Natl. Acad. Sci. U. S. A.* **2015**, *112*, 8999–9003.
- [89] H. Hopf, *Math. Ann.* **1927**, *96*, 209–224.
- [90] R. F. W. Bader, *J. Phys. Chem. A* **2009**, *113*, 10391–10396.
- [91] J. Cioslowski, S. T. Mixon, *Can. J. Chem.* **1992**, *70*, 443–449.
- [92] C. F. Matta, J. Hernández-Trujillo, T.-H. Tang, R. F. W. Bader, *Chem. - Eur. J.* **2003**, *9*, 1940–1951.
- [93] J. J. Novoa, M.-H. Whangbo, J. M. Williams, *J. Chem. Phys.* **1991**, *94*, 4835.
- [94] D. J. Wolstenholme, T. S. Cameron, *J. Phys. Chem. A* **2006**, *110*, 8970–8978.
- [95] E. A. Zhurova, C. F. Matta, N. Wu, V. V. Zhurov, A. A. Pinkerton, *J. Am. Chem. Soc.* **2006**, *128*, 8849–8861.
- [96] U. Koch, P. L. A. Popelier, *J. Phys. Chem.* **1995**, *99*, 9747–9754.
- [97] A. Nimmermark, L. Öhrström, J. Reedijk, *Z. Kristallogr. Cryst. Mater.* **2013**, *228*, 311–317.
- [98] N. Miyaura, K. Yamada, A. Suzuki, *Tetrahedron Lett.* **1979**, *20*, 3437–3440.
- [99] N. Miyaura, A. Suzuki, *J. Chem. Soc., Chem. Commun.* **1979**, 866.
- [100] M. Xia, Z.-C. Chen, *Synth. Commun.* **1999**, *29*, 2457–2465.
- [101] S. Darses, G. Michaud, J.-P. Genêt, *Eur. J. Org. Chem.* **1999**, *1999*, 1875–1883.
- [102] S. Darses, J.-P. Genêt, J.-L. Brayer, J.-P. Demoute, *Tetrahedron Lett.* **1997**, *38*, 4393–4396.
- [103] S. Darses, J.-P. Genet, *Eur. J. Org. Chem.* **2003**, *2003*, 4313–4327.
- [104] J. Barluenga, M. Tomas-Gamasa, F. Aznar, C. Valdes, *Nat. Chem.* **2009**, *1*, 494–499.
- [105] H. Takemura, N. Kon, M. Yasutake, H. Kariyazono, T. Shinmyozu, T. Inazu, *Angewandte Chemie (International ed. in English)* **1999**, *38*, 959–961.
- [106] H. Plenio, *Chem. Rev.* **1997**, *97*, 3363–3384.

- [107] D. Stalke, U. Klingebiel, G. M. Sheldrick, *Chem. Ber.* **1988**, *121*, 1457–1459.
- [108] D. Stalke, K. H. Whitmire, *J. Chem. Soc., Chem. Commun.* **1990**, 833–834.
- [109] D. Stalke, U. Klingebiel, G. M. Sheldrick, *J. Organomet. Chem.* **1988**, *344*, 37–48.
- [110] U. Pieper, S. Walter, U. Klingebiel, D. Stalke, *Angewandte Chemie (International ed. in English)* **1990**, *29*, 209–211.
- [111] G. R. Desiraju, *Crystal engineering. The design of organic solids*, Elsevier, Amsterdam u.a., **1989**.
- [112] G. M. J. Schmidt, *Pure Appl. Chem.* **1971**, *27*.
- [113] J. Bojarska, A. Fruziński, W. Maniukiewicz, *J. Mol. Struct.* **2016**, *1116*, 22–29.
- [114] R. D. Poulsen, J. Overgaard, A. Schulman, C. Ostergaard, C. A. Murillo, M. A. Spackman, B. B. Iversen, *J. Am. Chem. Soc.* **2009**, *131*, 7580–7591.
- [115] W. Perger, R. Pandey, M. A. Blanco, J. Zhao, *Chem. Phys. Lett.* **2004**, *388*, 175–180.
- [116] C. R. Martinez, B. L. Iverson, *Chem. Sci.* **2012**, *3*, 2191.
- [117] R. Michel, R. Herbst-Irmer, D. Stalke, *Organometallics* **2011**, *30*, 4379–4386.
- [118] J. Hey, D. M. Andrada, R. Michel, R. A. Mata, D. Stalke, *Angewandte Chemie (International ed. in English)* **2013**, *52*, 10365–10369.
- [119] V. R. Hathwar, M. Sist, M. R. V. Jorgensen, A. H. Mamakhel, X. Wang, C. M. Hoffmann, K. Sugimoto, J. Overgaard, B. B. Iversen, *IUCrJ* **2015**, *2*, 563–574.
- [120] D. Chopra, T. N. G. Row, *CrystEngComm* **2011**, *13*, 2175.
- [121] D. O'Hagan, *Chemical Society reviews* **2008**, *37*, 308–319.
- [122] A. Falcicchio, S. O. Nilsson Lill, F. M. Perna, A. Salomone, D. I. Coppi, C. Cuocci, D. Stalke, V. Capriati, *Dalton Trans.* **2015**, *44*, 19447–19450.
- [123] G. Saleh, L. Lo Presti, C. Gatti, D. Ceresoli, *J. Appl. Crystallogr.* **2013**, *46*, 1513–1517.

-
- [124] R. Herbst-Irmer, J. Henn, J. J. Holstein, C. B. Hubschle, B. Dittrich, D. Stern, D. Kratzert, D. Stalke, *J. Phys. Chem. A* **2013**, *117*, 633–641.
- [125] R. F. W. Bader, *J. Phys. Chem. A* **1998**, *102*, 7314–7323.
- [126] S. Grimme, C. Mück-Lichtenfeld, G. Erker, G. Kehr, H. Wang, H. Beckers, H. Willner, *Angewandte Chemie (International ed. in English)* **2009**, *48*, 2592–2595.
- [127] J. Cioslowski, S. T. Mixon, *J. Am. Chem. Soc.* **1992**, *114*, 4382–4387.
- [128] Y. A. Abramov, *J. Phys. Chem. A* **1997**, *101*, 5725–5728.
- [129] V. G. Tsirelson, A. S. Avilov, Y. A. Abramov, E. L. Belokoneva, R. Kitaneh, D. Feil, *Acta Cryst. B* **1998**, *54*, 8–17.
- [130] V. Tsirelson, Y. Abramov, V. Zavodnik, A. Stash, E. Belokoneva, J. Stahn, U. Pietsch, D. Feil, *Struct. Chem.* **1998**, *9*, 249–254.
- [131] A. Haaland, D. J. Shorokhov, N. V. Tverdova, *Chem. - Eur. J.* **2004**, *10*, 4416–4421.
- [132] L. J. Farrugia, C. Evans, D. Lentz, M. Roemer, *J. Am. Chem. Soc.* **2009**, *131*, 1251–1268.
- [133] R. Destro, L. Loconte, L. Lo Presti, P. Roversi, R. Soave, *Acta Cryst. A* **2004**, *60*, 365–370.
- [134] J. Henn, K. Meindl, *Acta Cryst. A* **2010**, *66*, 676–684.
- [135] M. R. V. Jorgensen, H. Svendsen, M. S. Schmokel, J. Overgaard, B. B. Iversen, *Acta Cryst. A* **2012**, *68*, 301-3; discussion 304.
- [136] J. Henn, K. Meindl, *Acta Cryst. A* **2012**, *68*, 304.
- [137] P. Evans, *Acta Cryst. D* **2006**, *62*, 72–82.
- [138] W. C. Hamilton, *Acta Cryst. A* **1969**, *25*, 194–206.
- [139] L. E. McCandlish, G. H. Stout, L. C. Andrews, *Acta Cryst. A* **1975**, *31*, 245–249.
- [140] D. Waterman, G. Evans, *J. Appl. Crystallogr.* **2010**, *43*, 1356–1371.
- [141] S. C. Abrahams, *Acta Cryst. A* **1969**, *25*, 165–173.
- [142] W. Kabsch, *Acta Cryst. D* **2010**, *66*, 125–132.
- [143] P. R. Evans, G. N. Murshudov, *Acta Cryst. D* **2013**, *69*, 1204–1214.
- [144] D. Borek, W. Minor, Z. Otwinowski, *Acta Cryst. D* **2003**, *59*, 2031–2038.

- [145] R. Kaminski, S. Domagala, K. N. Jarzemska, A. A. Hoser, W. F. Sanjuan-Szklarz, M. J. Gutmann, A. Makal, M. Malinska, J. M. Bak, K. Wozniak, *Acta Cryst. A* **2014**, *70*, 72–91.
- [146] H. Wolf, *Dissertationsschrift*, Georg-August-Universität, Göttingen, **2013**.
- [147] T. Skarzynski, *Acta Cryst. D* **2013**, *69*, 1283–1288.
- [148] L. A. Aslanov, G. V. Fetisov, J. A. K. Howard, *Crystallographic instrumentation*, Oxford Univ. Press [u.a.], Oxford, **1998**.
- [149] K. Iniewski, *Semiconductor radiation detection systems*, CRC Press/Taylor & Francis, Boca Raton, FL, **2010**.
- [150] B. B. He, *Two-dimensional x-ray diffraction*, Wiley, Hoboken, NJ, **2009**.
- [151] B. G. Batchelor (Ed.) *Springer reference*, Springer, London, **2012**.
- [152] C.-Y. Wu, W.-M. Chen, L.-T. Kuo, *IEEE transactions on biomedical circuits and systems* **2013**, *7*, 107–114.
- [153] J. H. Nielsen, E. Bruun, *Analog Integr Circ Sig Process* **2004**, *42*, 65–76.
- [154] H. Dietrich, *J. Appl. Crystallogr.* **1976**, *9*, 205–208.
- [155] G. V. Fetisov, V. T. Markov, *J. Appl. Crystallogr.* **1987**, *20*, 289–294.
- [156] Z. Fei, N. Kocher, C. J. Mohrschladt, H. Ihmels, D. Stalke, *Angewandte Chemie (International ed. in English)* **2003**, *42*, 783–787.
- [157] *Albula*, Dectris, Baden, Schweiz.
- [158] E. B. Knudsen, H. O. Sørensen, J. P. Wright, G. Goret, J. Kieffer, *J. Appl. Crystallogr.* **2013**, *46*, 537–539.
- [159] R. Azhakar, H. W. Roesky, J. J. Holstein, K. Pröpper, B. Dittrich, *Organometallics* **2013**, *32*, 358–361.

Danksagung

Die vorliegende Arbeit wurde in der Zeit von April 2013 bis April 2017 im Arbeitskreis Stalke am Institut für Anorganische Chemie der Universität Göttingen angefertigt. An dieser Stelle möchte ich allen danken, die zum Gelingen dieser Arbeit beigetragen haben.

An erster Stelle gilt mein Dank meinem Doktorvater Prof. Dr. Dietmar Stalke für sein grenzenloses Vertrauen in meine Arbeit, die Bereitstellung von einmaligen technischen Möglichkeiten für die Erforschung kristallographischer Probleme und die Möglichkeit viele interessante Fachkonferenzen und Großforschungseinrichtungen weltweit zu besuchen.

Herrn Prof. Dr. Franc Meyer möchte ich herzlich für die Übernahme des Korreferats danken.

Des Weiteren möchte ich den Mitgliedern der Prüfungskommission Dr. H. Sowa, Dr. F. Fabbiani, Prof. Dr. Ricardo Mata und Jun.-Prof. Dr. Selvan Demir für ihre Arbeit danken.

Mein Dank gilt auch dem *Center for Materials Crystallography* nicht nur für die finanzielle Unterstützung, sondern auch für die interessanten Workshops und die damit verbundenen Reisen.

Regine Herbst-Irmer, der „Grand Dame“ der Charge Density Subgroup, danke ich für ihre unendliche Geduld und die Fähigkeit auch die kleinste Unstimmigkeit in der Verfeinerung zu finden. Außerdem gebührt ihr Dank für die Hilfe bei so manchem routinekristallographischen Problem.

Allen ehemaligen und gegenwärtigen Mitgliedern des Arbeitskreis Stalke danke ich für die stets gute Stimmung und den nicht selbstverständlichen Zusammenhalt der Gruppe. Lennard danke ich für die „Zusammenarbeit“ an den Diffraktometern und die Fach- sowie Privatgespräche; Svole dem unerreichten Grillwart, weil er fast immer gut gelaunt war und es verstand einen aufzumuntern, wenn es mal nicht lief; Jakob, Hilke und Daniel für die Einführung in die Geheimnisse der Elektronendichteanalyse; Reent für seine herrlich lebenswürdige Art und Gespräche über „2001: Odyssee im Weltraum“ und andere nicht arbeitsrelevante Dinge.

Den Teilnehmern des *Herzog von Franken Elektronendichte Seminars* Hilke, Jakob, Markus, Reent, Dirk, Fridi, Daniel, Fink, Lennard und Ann-Christin danke ich für nette Grillabende und die Zusicherung, dass nichts so heiß gegessen, wie es gekocht wird.

Den *Skedoches* Alex, Anne, Johannes, Benny und Mathis für Mittags- und Feierabendausfahrten auf dem Longboard und Fachsimpelei über *Decks, Trucks and Rock 'n Roll*.

Peter und Alex danke ich für diverse Hilfeleistung und das Ertragen altkluger Sprüche im Projektlabor.

Meinen Korrekturlesern Hilke, Daniel, Julia und Regine danke ich für ihr Lob und die konstruktive Kritik.

Der guten Seele des Arbeitskreises, Heike Tappe, danke ich dafür, dass sie den Laden zusammenhält auch wenn es ihr manchmal vorkommen muss als würde sie einen Sack Flöhe hüten.

Unseren Hausmeistern Uwe, Acker und Niklas danke ich für nette Gespräche, kalte Getränke und natürlich dafür, dass sie immer schnell zur Stelle waren, wenn man sie brauchte und Dinge auch auf dem kurzen Dienstweg erledigt haben.

Allen Angestellten der Feinmechanik- und Elektrowerkstatt des Institutes für Anorganische Chemie danke ich für die tolle Zusammenarbeit. Vor allem die Arbeit von HaJo, Benjamin, Mariusz, Bernd, Rainer und Stephan sowie deren Azubis war mir eine große Hilfe.

Meiner Familie und besonders meinen Eltern Gabi und Alfred danke ich für das Vertrauen, dass sie in mich gesetzt haben und die ständige, nicht nur finanzielle, Unterstützung. Vielen, vielen Dank!

Zum Schluss möchte ich Julia dafür danken, dass sie die letzten drei Jahre mit mir durchgestanden hat. Danke dafür, dass Du trotz Fernbeziehung da warst, wenn ich dich brauchte. Für die eine oder andere Ermahnung, „das jetzt einfach mal zu machen“ und ein liebes Wort an der richtigen Stelle.

Curriculum Vitae

Name: Felix Engelhardt

Date of birth: 07.11.1985 in Northeim

Nationality: German

Marital status: unmarried

Address: Hagenweg 51, 37081 Göttingen

E-mail: felix.engelhardt@googlemail.com

Scientific Career

- 04.2013 – 04.2017 PhD studies in the Georg August University School of Science program. Work on the doctoral thesis “Evaluation of Detector and Intensity reliability in Charge Density Studies” in the *Stalke* workgroup.
- 02.2013 Diploma in chemistry
- 05.2012 – 11.2012 Work on the graduation thesis “Elektronendichteuntersuchungen an alkalimetallorganischen Verbindungen” in the *Stalke* workgroup.
- 10.2005 – 05.2012 Chemistry studies at the Georg August University Göttingen
- 06.2005 Abitur at the Georg-Christoph-Lichtenberg Gesamtschule

Presentations

- 2015 18. Sagamore Conference, Italy, Poster Presentation
- 2015 23. Tagung der Deutschen Gesellschaft für Kristallografie, Germany, Poster Presentation
- 2014 8. Workshop of the Center for Materials Crystallography, Germany, Talk
- 2012 6. Workshop of the Center for Materials Crystallography, Germany, Talk

Scientific Publications in Print

- 2014 **Unprecedented Borylene Insertion into a C-N Bond**, Rajendra S. Ghadwal, Christian J. Schuermann, Felix Engelhardt, Christian Steinmetzger, *Eur. J. Inorg. Chem.*, 4921-4926.
- 2013 **Facile Access to Silyl-Functionalized N-Heterocyclic Olefins with HSiCl₃**, *Rajendra S. Ghadwal, Sven O. Reichmann, Felix Engelhardt, Diego M. Andrada, Gernot Frenking, Chem. Commun.*, 49, 9440-9442
- 2013 **Coordination Abilities of Di-2-picolylphenylphosphane Judged on the Basis of Charge Density Investigations**, *Ina Objartel, Dirk Leusser, Felix Engelhardt, Regine Herbst-Irmer, Dietmar Stalke, Z. Anorg. Allg. Chem.*, 639, 2005-2012.

Skills and Interests

Languages:

German: first language

English: fluent

Computer literacy:

C, C++, Adobe Photoshop, Adobe Illustrator, Python, Latex, Microsoft Office, Microsoft Windows (XP, 7, Server 2008), Linux (Debian, Ubuntu, Fedora), Computer Hardware and Support

Sports:

Free climbing, Longboarding, Inline Skating, Skiing